THE UNIVERSITY *of* EDINBURGH

The Effect of Attractive Forces on Active-Passive Interactions

Samuel Griffiths

Doctor of Philosophy
The University of Edinburgh
December 2020

Abstract

Active matter is a burgeoning topic of current soft matter research due to its innate non-equilibrium behaviour. However, because of the difficult and complex procedures that are common with experimental active systems, it is appealing to investigate what active properties can be retained in mixtures of active and passive particles. In particular, we are interested in systems with polymer-induced depletion attractions, where we review if attractions can increase the interaction timescales between active and passive particles, with the aim of increasing the effect of activity on the passive particles. For this work, we use motile *E. coli* for active particles, micron-sized spherical colloids for the passive particles and a polymer depletant of polymer-colloid size ratio, $\xi = 0.06$.

We start by investigating how depletion attractions affect the enhanced diffusion of passive particles in baths of motile bacteria. For diffusion on a two-dimensional surface, bacteria are observed to push the particles via steric interactions. As attraction strength is increased, the bacteria can stick to the particles and drag passive particles along. This depletion-enhanced, activity-enhanced diffusion can result in a thirty-fold increase in diffusivity over the passive particle's Brownian diffusivity. However, for three-dimensional diffusion, depletion attractions are not as effective. Even though the active diffusivity remains low, for large attraction strengths, when a tracer does stick to a bacterium, the tracer can be dragged for distances up to 50 μm.

We proceed by studying the effect of doping motile bacteria into a phase-separating, two-dimensional colloid-polymer mixture. In the absence of bacteria, the passive particles phase separate into a dilute gas phase and dense crystals which macroscopically look gel-like. We find that bacteria can accumulate at the edges of crystals due to their persistent motion. The bacteria are observed to then break the cluster apart and swim through the gap, pushing the two halves out of the range of depletion forces. The competition between aggregation

and fragmentation results in a steady-state cluster phase, this incomplete phase-separation is known as micro-phase separation. The mean steady-state cluster size is found to increase with increasing attraction strength and decreasing bacterial concentration. We show that the production of a steady-state and its scaling with bacterial concentration, as well as the form of the cluster size distribution agrees with predictions of Smoluchowski equation modelling aggregation-fragmentation.

Finally, we start to explore the possibility of using samples containing only light-activated bacteria to create designer structures at micron scales. These light-activated bacteria continuously swim when exposed to green light and thus accumulate in dark regions of the sample. It has been previously shown that with a spatially modulated light field, templated structures can be created from light-activated bacteria. Such structures rapidly decay on the deactivation of the light source due to diffusion. We show that the addition of polymer depletants stabilise the structures, increasing their lifetime by at least two orders of magnitude. Such work relies on the detail that the attraction strength required to induce phase separation increases with activity and thus, with a carefully tuned attraction strength, phase separation can be locally induced within dark regions of the sample. This work represents a few initial steps to building structures from passive colloids using bacteria.

Lay Summary

The development of active matter, where here, active matter refers to the ability of particles to self-propel, has yielded many novel and results; phase separation, turbulence, powering micro-machines and pattern formation to name a few. These active particles are often difficult to produce and use at high concentrations, so it can be desirable to try to impose their unique properties onto passive (non-self-propelled) particles. We extend studies on active-passive mixtures by introducing short-ranged attractive interactions between the populations. Throughout we will use one of the most well studied active particles, a non-pathogenic strain of highly motile Escherichia coli.

First, we study enhanced diffusion, the process by which the diffusivity of an individual passive particle is increased by the presence of active particles. Without attractions between the active and passive particles, enhanced diffusion has been previously found to occur due to hydrodynamic flows from the active particles. We find that with attractions, the passive particles can stick to the active particles and be dragged short distances which can increase resulting diffusion enhancement thirty-fold when near a surface. This increase in diffusion enhancement is not nearly as prevalent far from a surface, which we attribute to the increased range of active particles flow field that is able to push the active particle away limiting the frequency of sticky interactions.

Next, we review the phase behaviour of a collection of passive particles when doped with active particles. Without active particles, attractions between the passive particles induce aggregation yielding crystalline clusters. We observe that active particles can swim through the clusters along the grain, breaking them apart. The competition between the passive particles aggregating and the active particles breaking the clusters apart creates a highly dynamic steady state of small clusters. We go on to find that our results are well described by an existing model for systems undergoing aggregation and fragmentation.

Finally, by carefully tuning the attraction strength, we develop a system where we can spatially control the phase behaviour with the application of green light. This work requires a new strain of *E. coli* (developed elsewhere) which converts the energy from light into a propulsive force, so when illuminated, it can locally escape attractive interactions.

Declaration

I declare that this thesis was composed by myself, that the work contained herein is my own except where explicitly stated otherwise in the text, and that this work has not been submitted for any other degree or professional qualification except as specified.

(*Samuel Griffiths, December 2020*)

Acknowledgements

There are a number of people who I owe a great deal of thanks to for all of their help in the production and completion of this thesis. Firstly, I want to thank my supervisor Professor Wilson Poon for his endless support. This work would not have been possible without his input.

I especially want to thank Dr Nick Koumakis for all his patience and help with coding, refining experiments and in particular for his comments on this thesis. I also want to thank Dr Aidan Brown and Dr Teun Vissers for all of the fruitful discussions about my work.

Thanks to Dr Angela Dawson for her company in the lab and all of help with Biological materials. I want to thank Dr Vincent Martinez, Dr Jochen Arlt and Dr Jana Schwarz-Linek for all that they have taught me about active matter, microscopy and DDM. I would also like to acknowledge Dr Andy Schofield, Dr Job Thijssen and Dr Teuta Pilizota for their help.

I want to thank Ed Muir and Xuemao Zhou for their companionship and for listening to me complain about failed experiments. Special thanks to all of my friends far and wide for keeping sane over the last few years. And finally, I want to thank my family, for whom I would not have made it this far without.

Contents

List of Figures

List of Tables

Chapter 1

Introduction

1.1 Brownian Motion

The random motion of micron-sized particles was first observed by Brown in 1827. Einstein later showed that this motion was the result of thermally driven solvent molecules pushing the larger particle around. The stochastic nature of forces pushing dispersed particles results in a random walk, characterised by a mean square displacement (MSD)

$$\langle \Delta r^2(\tau) \rangle = 2\mathcal{N}D\tau \tag{1.1}$$

For $\mathcal{N}$ dimensions, over time τ, with a diffusion constant D. In the absence of an external field, colloids diffuse in random directions which ensures $\langle \Delta r \rangle$=0. Their diffusion constant is defined as

$$D = \frac{k_B T}{6\pi\eta R} \tag{1.2}$$

Where the Boltzmann constant k_B, temperature T, viscosity η and particle radius R.

The dynamics of such a system is fundamentally equilibrium in nature and has been well understood for decades. We will refer to these types of particles as passive particles because they passive move due to thermal fluctuations.

1.2 Active Particles

The alternative to a passive particle is an active particle, one which consumes energy to perform some non-equilibrium activity. Examples of active systems include cells that grow and replicate, however, within this thesis, we will focus exclusively on active particles which undergo self-propulsion. A common class of self-propulsive particles are natural micro-organisms, for example, bacteria, algae and spermatozoa. Recently a second class has been created, synthetic active particles like the two-faced Janus particle, which self-propel by decomposing hydrogen peroxide on their platinum-coated face. The details of the mechanism for Janus particle propulsion is still under review [21, 22].

The motion of active particles is dominated by their low Reynolds number, the ratio of inertial to viscous forces

$$Re = \frac{av\rho}{\eta} \tag{1.3}$$

For a characteristic dimension a, speed v, density ρ and viscosity η. Typical active particle have a characteristic dimension of $\sim 1\ \mu m$, $v\ \ 10\ \mu m s^{-1}$, $\rho = 10^3\ kgm^{-3}$, and $\eta = 10^{-3} Pa.s$ which gives a Reynolds number of $\ 10^{-5}$, so it is fair to say, inertia plays no role here.

The lack of inertia has a dramatic impact on fluid motion, as described by the Navier-Stokes equation (expressed in units of force per unit volume)

$$-\nabla p + \eta \nabla^2 v = \rho \frac{\partial v}{\partial t} + \rho v \cdot \nabla v \tag{1.4}$$

Where the right-hand side is the inertial term, ∇p is the pressure gradient and $\eta\ \nabla^2\ v$ is the viscous term. In this low Reynolds number environment, we can neglect the inertial term, which yields

$$-\nabla p + \eta \nabla^2 v = 0 \tag{1.5}$$

This description no longer contains any time derivatives, and thus states any response to motion is instantaneous. Consider the effect this has on swimming by reciprocal motion, which is the act of performing an action to move, then the same

in reverse. For example, the scallop, which slowly opens its shell and slams it shut to propel its self forward. In a high Reynolds number environment, where scallops exist, after quickly closing its shell the scallop moves quickly and continues to move as its velocity is dissipated. In a low Reynolds number environment, the speed of the action no longer matters, and the scallop would remain in its original position. The reversibility of reciprocal motion was famously shown by Taylor et al [139], who injected ink into a very viscous fluid between two cylinders and then began to shear the fluid. After several cycles, they reverse the shear for the same duration which returns the ink to its exact starting point.

To swim at low Reynolds number, active particles requires some form of non-reciprocating motion. There are two famous examples within nature, firstly the "flexible oar". If the oar is stiff, pushing it back and forth is reciprocal motion and yields no net displacement. However if the oar is allowed to bend on each stroke, it will bend in one direction on the first half of the stroke and the opposite as it returns. This flex is sufficient to allow propulsion, and for example, it is how spermatozoa beat their single flagellum to swim.

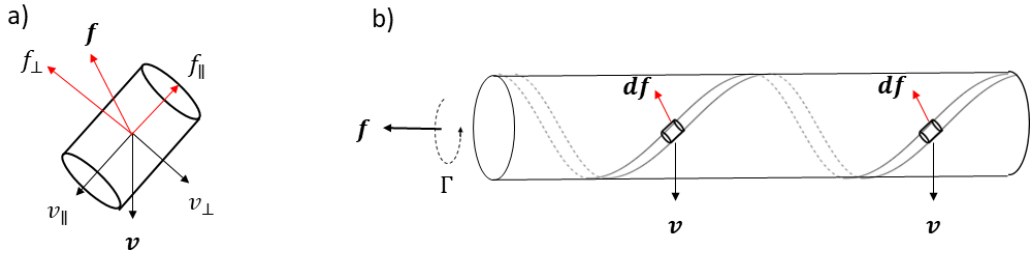

Figure 1.1 The drag force on helix comprising of a sequence of cylinders. a) A cylinder being dragged through a fluid with velocity v with an off-inverse drag force f. b) A sequence of cylinders making up a helix. As the helix is rotated with angular velocity Γ experiences net force f.

The second famous example of non-reciprocal motion is the rotation of helix or "corkscrew". Consider the helix as a series of cylinders, for example, see figure 1.1. As the helix is rotated with some angular velocity, each cylinder moves through the fluid at velocity, v. The drag, f, on the cylinder is larger perpendicular to its central axis than along it, causing the total drag to not be anti-parallel to the velocity. Averaging over all cylinders across the length of the helix yields a total drag along the axis of the helix, and thus a propulsive force in the opposite direction. These do not slip through the medium like a corkscrew does a cork, but exert a force upon the surrounding medium and can require 100 rotations to

propel themselves a single wavelength [77, 102]. This is the mechanism used by *E. coli* to self-propel.

The bacterium *E. coli*, which is the active particle we will focus on in this work, is approximately 0.75 μm in diameter with a length of 2-5 μm depending on its growth stage. Each cell has ∼7 flagella randomly distributed around the body of 75 nm diameter and length of 7-10 μm which are connected to complex rotatory motor proteins embedded within the cell wall. When all of the flagella are turned counter clockwise they form a single helical bundle behind the cell, the process by which this occurs is still under investigation. Note that within a single culture of E. coli, a fraction of the cells do not have flagella and are thus non-motile.

Each flagellum is connected to a flexible hook which then connects to a complex motor protein assembly in the cell membrane. The motors are driven by a proton motive force (PMF), a flux of H^+ entering the cell from the surrounding medium. The PMF is maintained at 150 mV by the consumption of a carbon source, i.e. a fuel [123, 130]. Without a carbon source present, for example, glucose, *E. coli* can continue to swim if oxygenated [123].

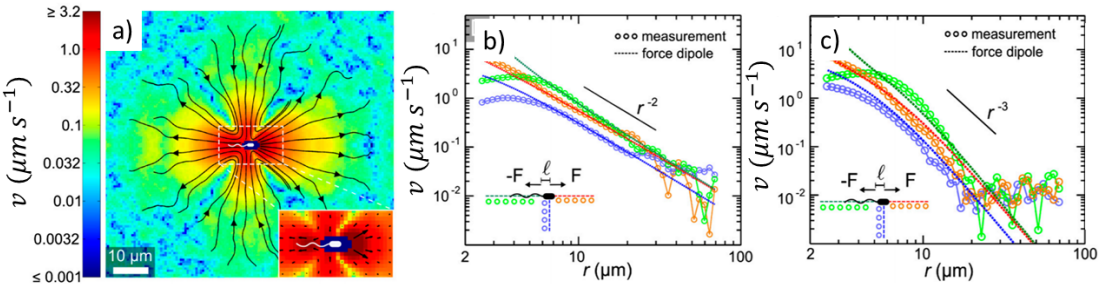

Figure 1.2 Taken from [37]. a) Experimentally measured flow field created by a single free-swimming *E. coli*, far from a surface, where the direction of the flow is indicated by arrows. b) The decay of the fluid velocity, when the cell is far from a surface. c) The decay of the fluid velocity, when the cell is 2 μm above the surface.

The swimmer's body exerts a force on fluid, f, which is balanced by an opposing force by the flagella, $-f$. These opposing forces can be described as a force dipole, where the fluid velocity $v \propto f/\eta r^2$. Experimentally, the force dipole model has been found to be accurate in the far-field by Drescher *et al.* as shown in figure 1.2a and b, while it overestimates the flow in the near-field [37]. Drescher *et al.* found that the best to fit their data was achieved using two force monopoles instead of a point dipole, giving the force dipole $f = 0.42$ pN [37]. The cell drag monopole was determined to be behind the cell body, indicating the importance

of the flagella bundle.

The flow fields exerted by motile cells must decrease in proximity to a surface due to the no-slip boundary condition on the fluid velocity, where molecules at the surface have zero velocity [17]. So when in proximity to a wall (figure 1.2c) a cell's flow field decays faster than in the bulk (figure 1.2b) [37].

1.3 Active Motion

In this work we are interested in imparting active properties on passive particles, here we will introduce one of the most fundamental active properties, their motion. The observed motion of an active particle is dependant on the observation window. Active particles are still subject to Brownian forces, which dictate their motion over short time scales. Active particles then exhibit ballistic motion over intermediate time scales, where the square displacement is $\langle \Delta r^2 \rangle \approx v^2\tau^2$ for a given swimming speed v and time τ. For long times, Brownian forces randomise the particle's orientation giving rise to long-time diffusive behaviour. The time-scale over which an active particle turns from ballistic to effective diffusion is controlled by their rotational diffusion time, τ_r [102]

$$\tau_r = \frac{8\pi\eta R^3}{k_B T} \tag{1.6}$$

The mean square displacement of an active Brownian particle in two dimensions is [98]

$$\langle \Delta r^2(\tau) \rangle = 4D\tau + \frac{v^2\tau_r^2}{3}\left[\frac{2\tau}{\tau_r} + exp\left(\frac{-2\tau}{\tau_r}\right) - 1\right] \tag{1.7}$$

Whereat short times, $\tau \ll \tau_r$, this can be approximated as $\langle \Delta r^2(\tau) \rangle = v^2\tau^2$. While at long times, $\tau \gg \tau_r$, gives an effective diffusion constant of $D_{eff} = D + v^2\tau_r/6$

Note that equation 1.7 can also be used to describe the motion of a Brownian particle and its fast decorrelation due to inertia (obviously for such a description the first term is set to zero, i.e. $4Dt = 0$) [10, 145]. This is reduced to equation 1.1 because the time scales involved in Brownian motion are several orders of magnitude smaller than what is generally measured in experiments [73].

In this work, we focus on the active particle, motile *E. coli*. So far we have described particles that undergo continuous propulsion which undergoes rotation due to Brownian forces, which we call "smooth swimmers", however, such motion is atypical for the species. The wild type (WT), i.e. the typically observed type, swims with "run-and-tumble" motion, named after the bacterium's runs where they swim for $\sim$ 1s and then tumble for $\sim$0.1s [12]. A tumbling event is triggered when one or more of the motors reverses its direction briefly, this breaks the flagella bundle apart and causes the cell to spin with no net displacement. When the motors all turn counter-clockwise again, the flagella reforms a bundle and the cell will undergo another run in a new direction [144]. Run-and-tumble motion allows each cell to control its reorientation timescale, τ_r, an ability that is useful for processes like chemotaxis, where the cell will preferentially swim up or down a concentration gradient [1]. To remove run-and-tumble motion, and thus induce smooth swimming in *E. coli* requires the deletion of appropriate chemotactic genes [123].

Within this thesis, we will use active baths, a fluid containing a wealth of active particles. These baths are far from equilibrium, and thus can generate novel non-equilibrium states. A particularly striking property of dense active baths is the manifestation of swirling patterns and short-lived vortices, caused by the collective motion of its parts. Such turbulent behaviour is generally the result of inertial forces, which are not present in these systems. While the details are still under debate, the basic phenomenology can be understood by the Vicsek model, which is a minimal model where each constituent (or here particle) within the system attempts to align itself with its neighbours [150]. For baths of *E. coli*, long-range hydrodynamics act as aligning interactions. These interactions have a characteristic range, which limits the lowest density at which each constituent senses its neighbours, below this limit, where we will focus, uncorrelated motion occurs.

1.4 Particle Interactions

1.4.1 Hard-Spheres

We introduce particle interactions with one of the simplest interactions, the hard-sphere potential. The interaction potential, $U(r)$, is infinite between two particles

in contact (repulsive) and drops to zero when the centre-to-centre separation, r, increases.

$$U_{\mathrm{HS}}(r) = \begin{cases} \infty & r \leq \sigma \\ 0 & r > \sigma \end{cases} \tag{1.8}$$

where σ is the particle diameter.

These hard-spheres do not deform and cannot penetrate or overlap with other particles. However experimentally, solid particles are not perfect hard spheres because of van der Waals attractions. Electrostatic repulsions or steric polymer brushes can be used to minimise the effect of these attractions, but at best these result in steep potentials that are only an approximation to hard-spheres [114].

1.4.2 Electrostatic Interactions

Van der Waals forces, which here refer to London dispersion forces, are the result of fluctuations of the electron clouds in a particle, resulting in momentary dipole, which can then induce a momentary dipole in a neighbouring particle resulting in an attractive force. These forces are always attractive. For two spheres of radius R at a centre-to-centre separation of r, the Van der Waals potential is [71]

$$U_{\mathrm{VdW}}(r) = \frac{-A}{6}\left[\frac{2R^2}{r^2+4Rr} + \frac{2R^2}{r^2+4Rr+R^2} + ln\left(\frac{r^2+4Rr}{h^2+4Rr+R^2}\right)\right] \tag{1.9}$$

where A is the Hamaker constant, R is particle radius and r is centre-to-centre separation. This potential is very short-ranged and very strong, which can result in the aggregation of particles, sketched in figure 1.3a.

In this work, we use electrostatic repulsions to stabilize particles and prevent aggregation and phase separation. For charged particles in a fluid, repulsive forces occur due to the formation of a double layer. Particles with ionisable groups on the surface undergo dissociation when dispersed in a fluid, leaving the particle with a surface charge. The charged surface adsorbs counter-ions, depleting co-ions from the surface. The co-ions then form a more diffuse second layer, the combination of these layers is the so-called double-layer [71]. As the

ionicity in the fluid increases, the surface charge is screened more, i.e. the double layer becomes more compact.

As a charged particle approaches another, their double layers begin to overlap resulting in a repulsive force, given by [71]

$$U_{\mathrm{DLR}}(r) = k_B T \frac{8p_c^2}{1+p_c^2} \frac{R}{\lambda_B} exp(-r/\lambda_D) \tag{1.10}$$

where $p_c = 2\pi\lambda_D\lambda_B s_c/e$ for the elementary charge e and surface charge density s_c. λ_D is the Debye screening length

$$\lambda_D = \sqrt{\frac{1}{8\pi\lambda_B n_s}} \tag{1.11}$$

for salt number density, n_s. λ_B is the Bjerrum length

$$\lambda_B = \frac{e^2}{4\pi\epsilon_0\epsilon_r k_B T} \tag{1.12}$$

where e is the elementary charge, ϵ_r is the relative dielectric constant and ϵ_0 is the dielectric constant of a vacuum.

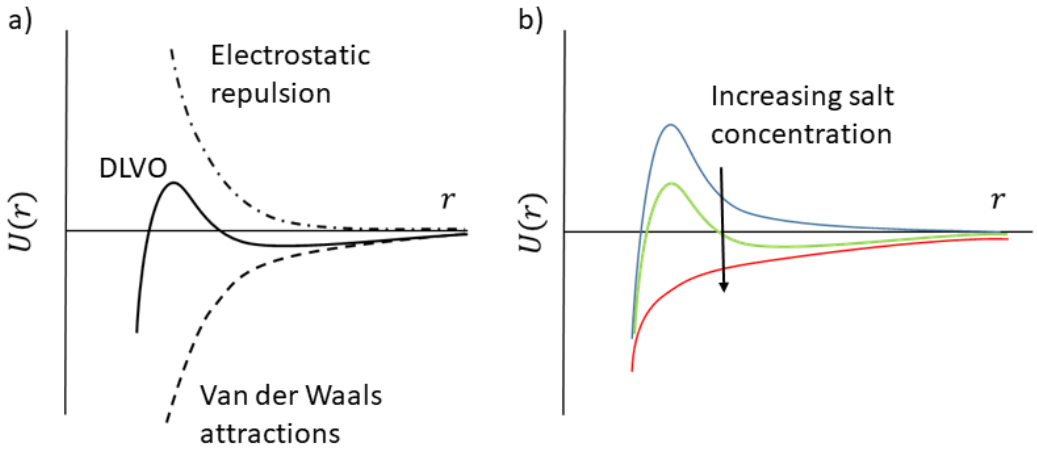

Figure 1.3 Schematic representation of the DLVO potential. a) The DLVO potential as the sum of Van der Waals attraction and electrostatic repulsion. b) The effect of increasing salt concentration on the DLVO potential

The DLVO potential is given by the sum of Van der Waals attraction and double

layer repulsion

$$U_{\mathrm{DLVO}}(r) = U_{\mathrm{VdW}}(r) + U_{\mathrm{DLR}}(r) \tag{1.13}$$

The DLVO potential is illustrated in figure 1.3a, if the maximum is larger than a few k_BT, aggregation is prevented [71]. However, as the double layer repulsion is screened by increasing salt concentrations the potential can become purely attractive, as illustrated in figure 1.3b. This introduces a salt concentration limit for particle stability.

1.4.3 Polymer Depletion

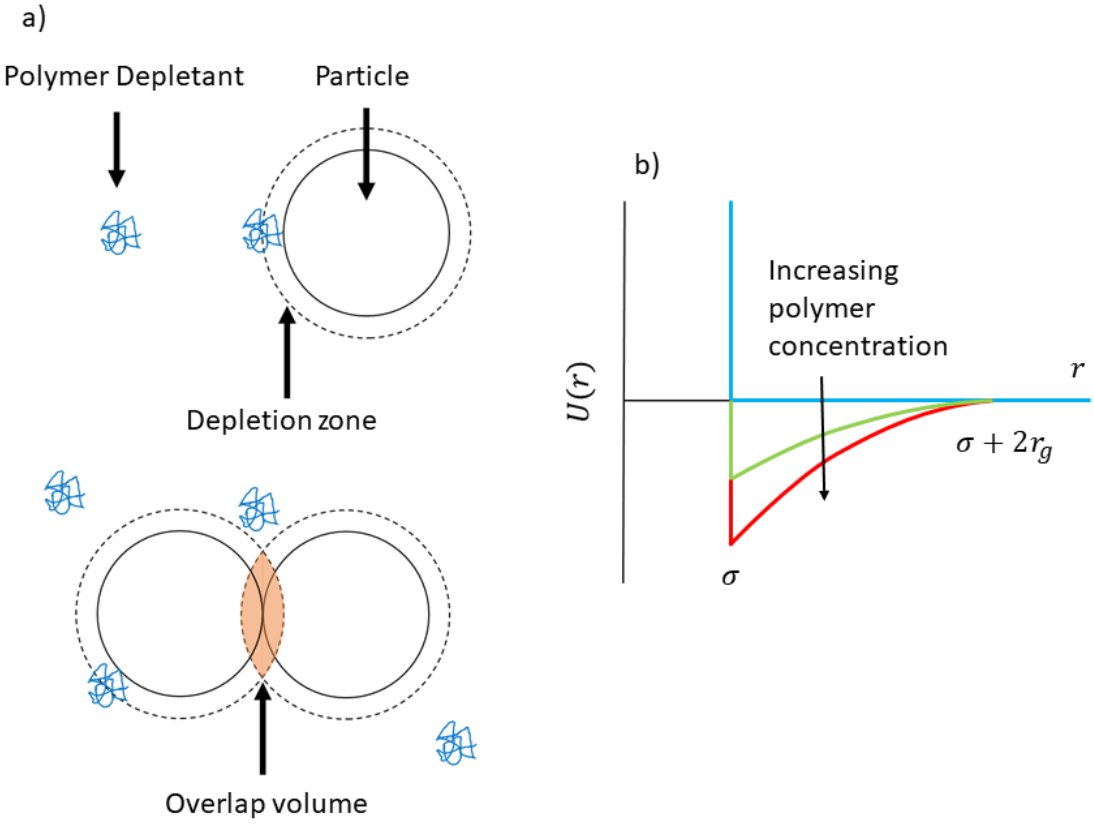

Figure 1.4 Schematic representation of the polymer-induced depletion interaction. a) Depiction of polymer-particle interactions resulting in a depletion zone around the particle. b) Sketch of the interaction potential arising from polymer depletion.

Particle attractions can also be induced by the addition of a non-adsorbing polymer. Since the polymers do not adsorb, within the fluid there is a zone around

the particles which the polymer centres cannot penetrate without significant deformation, called the depletion zone. As two particles approach the depletion zones overlap which increases the volume available to the polymer. As the free volume increases the polymers free energy decreases. So, even though polymer-particle and particle-particle interactions are repulsive, the favoured state is one where the particles are in close proximity, yielding an effective attraction between the particles. A schematic showing the overlap of depletion zones is shown in figure 1.4a.

This depletion force is the result of an unbalanced osmotic pressure from the surrounding fluid which is given by [6, 7, 158]

$$U_{\mathrm{HS}}(r) = \begin{cases} \infty & r \leq \sigma \\ -\Pi_p V_{overlap} & \sigma < r < \sigma + 2r_g \\ 0 & r > \sigma + 2r_g \end{cases} \tag{1.14}$$

where $V_{overlap}$ is the overlapping volume of the depletion zones and Π_p is the osmotic pressure. The range of the attraction is given by the polymer's radius of gyration, r_g.

The osmotic pressure is proportional to the number density of polymer depletants, n_p [71]

$$\Pi_p = n_p k_B T \tag{1.15}$$

For two symmetric spheres, the overlap volume is given by

$$V_{overlap}(r) = \frac{\pi}{6}\sigma^3(1+\xi^3)\left[1 - \frac{3r}{2\sigma(1+\xi)} + \frac{r^3}{2\sigma^3(1+\xi)^3}\right] \tag{1.16}$$

where the size ratio is $\xi = 2r_g/\sigma$.

This means the potential is controlled by the radius of the polymer depletant and the depth by its number density. A sketch of the potential, equation 1.14 is shown in figure 1.4

1.4.4 Interaction Potentials in Baths of E. Coli

In the experiments presented here, we use high salt concentrations to promote 'ideal' conditions for active particles, motile *E. coli*. Here, ideal means what has widely been studied. We report in appendix A how changing salt concentrations can alter the behaviour of *E. coli*. Note, this salt also screens electrostatic repulsions between particles (equation 1.11). The salt concentration must therefore be carefully selected to be close to ideal but not high enough to induce aggregation.

Chapter 2

Materials and Methods

In this thesis, we use microscopy to study the dynamics and structure of passive particles with depletion-induced attraction in a bath of motile *E. coli*. In this chapter, we review the materials and general methods used.

2.1 Polymer

To induce particle-particle and particle-bacteria attractions, we add a non-adsorbing polymer depletant, where the attraction strength $U(r) \propto \phi_p^{free}$, for a polymer volume fraction in the free volume ϕ_p^{free}. In this work, we will use sodium polystyrene sulfonate, NaPSS ($M_w \sim 10^6$ Da, linear chain purchased from Sigma Aldrich), which has previously been shown to act as a non-adsorbing depletant in samples of *E. coli* [121, 122, 124]. Ideally, the polymer used would be a random coil, however, NaPSS is a polyelectrolyte for which the charges on the backbone repel inducing a self-avoiding behaviour. Random coils can be induced in NaPSS at sufficient salt concentrations, which screens the negative charge. Here, PSS is dispersed in a phosphate buffer (to accommodate bacteria and particles), which is lower ionicity than ideal conditions [160]. In an ideal solvent, polymer chains have random walks, however here, the chain is slightly self avoiding. This swelling of the polymer coil at lower than ideal salt concentrations increases the depth and width of the depletion potential [6, 142].

Since the volume fractions of particles and cells used within this work are very low, the volume fraction in the free volume, $\phi_p^{free} \approx \phi_p$, where $\phi_p = c_p/c_p^*$ for a

polymer mass concentration, c_p and the overlap concentration [51]

$$c_p^* = \frac{3M_w}{4\pi r_g^3 N_A} \tag{2.1}$$

For a radius of gyration r_g and Avogadro's number N_A.

One of the best methods of calculating the overlap concentration is from the measurement of the intrinsic viscosity $[\eta]$, where $c_p^* \approx [\eta]^{-1}$ [118]. The intrinsic viscosity can be written as the virial expansion of the viscosity, η and the polymer concentration, c_p, where the polymers occupy the available free volume

$$\eta = \eta_s(1 + [\eta]c_p + k_H[\eta]^2 c_p^2 + ...) \tag{2.2}$$

where k_H is the Huggins coefficient. At low polymer concentrations, equation 2.2 fits results well and therefore higher-order terms can be ignored [118]. Solving for $[\eta]$ gives the Huggins fit for the intrinsic viscosity

$$\frac{\eta - \eta_s}{\eta_s c} = [\eta] + k_H[\eta]^2 c_p \tag{2.3}$$

An alternative involves solving equation 2.2 for η/η_s and then taking the natural logarithm

$$ln(\eta/\eta_s) = ln(1 + [\eta]c_p + k_H[\eta]^2 c_p^2 + ...) \tag{2.4}$$

For small c_p, expansion of this logarithm produces

$$ln(\eta/\eta_s) = [\eta]c_p + (k_H - \frac{1}{2})[\eta]^2 c_p^2 + ... \tag{2.5}$$

Yielding a different form known as the Kraemer equation

$$\frac{ln(\eta/\eta_s)}{c_p} = [\eta] + \left(k_H - \frac{1}{2}\right)[\eta]^2 c_p \tag{2.6}$$

Both equations 2.3 and 2.6 should return the same value for the y-intercept, $[\eta]$.

We measure the viscosity at various concentrations of PSS in motility buffer (6.2 mM K_2HPO_4, 3.8 mM KH_2PO_4, 0.1 mM EDTA at pH $\sim$ 7.5) using a shear rate-controlled rheometer with cone-and-plate geometry, the viscosity and Huggins and Kraemer fits are plotted in figure 2.1. Fits to the Huggins equation yield $[\eta] \approx 3.7$ dL/g and the Kraemer equation $[\eta] \approx 3.0$ dL/g, for our purposes we will take the average value, $[\eta]$= 3.35 dL/g (and $c_p^* = 0.435$ wt%). For more accurate measurements of $[\eta]$, where both fits yield the results, maybe possible with the use of lower polymer concentrations and careful use of capillary viscometers [118]. With the intrinsic viscosity and thus c_p^*, using equation 2.1, we can now extract the polymer's radius of gyration, $r_g = 45$ nm.

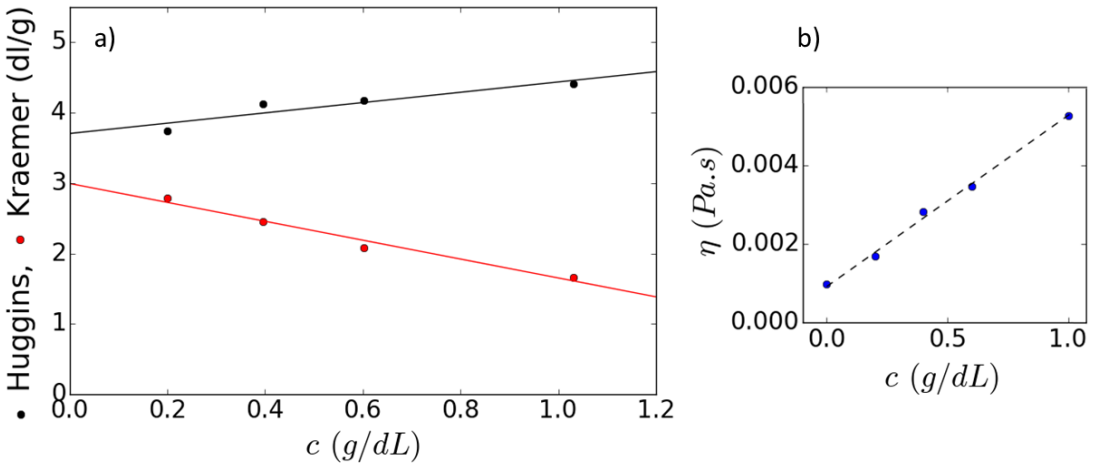

Figure 2.1 Measurement of the intrinsic viscosity of sodium polystyrene sulfonate in motility buffer (6.2 mM K_2HPO_4, 3.8 mM KH_2PO_4, 0.1 mM EDTA at pH $\sim$ 7.5). a) Fits to the Huggins and Kraemer equations, equations 2.3 and 2.6. b) The viscosity measurements used for the plotting of Huggins and Kraemer fits, fitted to a straight line.

2.2 Particles

In this thesis, we use two separate particle stocks for our two types of experiments. For our quasi-two-dimensional system, we use 1.5 μm diameter silica particles from Bangs particles, of density, ρ= 2 g/cm^3, twice that of water. These dense particles quickly sediment to the bottom of the capillary with velocity, $v_{sed} = \Delta mg/3\pi\eta\sigma$, where Δm is the buoyant mass, giving $v_{sed} = 1.2$ μms^{-1}. In our 400 μm high capillaries, the silica particles take $\sim$ 5 minutes to reach the bottom

surface. In section 4.2, we will show that on average these particles remain within 200 nm of the surface.

For measurements far from the surface, we use 1.8 μm diameter fluorescent polystyrene (yellow-green) from Invitrogen. Polystyrene is used due to its close density matched with water (where the density mismatch, $\Delta\rho$= 0.04 g/cm^3) and are therefore much more stable to sedimentation. The fluorescence labelling allows for the particles to be easily discriminated from *E. coli*.

The particles are dispersed in a phosphate buffer composed of 6.2 mM K_2HPO_4, 3.8 mM KH_2PO_4, 0.1 mM EDTA at pH $\sim$ 7.5, this buffer is used for the later addition of motile *E. coli*. These salts will partially screen the charge stabilisation of both particles, but here, not by enough to induce aggregation. We also add 0.3 wt% TWEEN 20 surfactant to minimize surface adhesion [156].

2.3 Biological Materials and Methods

2.3.1 Bacteria

Throughout this thesis, we use a non-pathogenic strain of *E. coli*, AB1157, which is highly motile, relatively easy to mutate and has already been extensively studied and optimised for the use as an active colloid [123]. Unless otherwise specified, we use AB1157 ΔCheY, where the Δ refers to the deletion of the chemotactic CheY gene, yielding smooth swimming bacteria. In brief sections, we will also use the wild-type (WT) which undergo run-and-tumble motion and also use AB1157 ΔCheZ which undergo constant tumbling.

In chapter 8, we will discuss the use of AD10, a strain of AB1157 which is able to self-propel by illumination with green light activating genetically added proteorhodopsin (PR) proteins [5]. PR exists as extrachromosomal DNA within the cell, further to that the unc gene was deleted to decrease stopping time after green-light is switched off and again the CheY gene is deleted to yield smooth swimmers. Resistance to the antibiotic ampicillin was also encoded, as this allows for growing cultures of this strain in media containing ampicillin, hindering the loss of the evolutionarily unfavourable genetic modifications.

The ΔCheY and ΔCheZ strains were transformed by J. Schwarz-Linek and AD10

was transformed by A. Dawson.

2.3.2 Media

Luria broth (LB) is a rich growth medium containing 10 g/L tryptone, 5 g/L yeast extract and 5 g/L NaCl, dispersed in deionised water, which is then sterilised by autoclaving at 120Celsius for 20 minutes. LB agar contains an additional 15 g/L agar.

Tryptone broth (TB) is a moderately rich growth medium used for growing reproducibly highly motile cultures of *E. coli* [2]. TB contains 10 g/L tryptone and 5 g/L NaCl, dispersed in deionised water, which is then sterilised by autoclaving at 120Celsius for 20 minutes.

Motility buffer (MB) composed of 6.2 mM K_2HPO_4, 3.8 mM KH_2PO_4, 0.1 mM EDTA at pH $\sim$ 7.5, in which the bacteria do not grow. This buffer is based on Berg's motility buffer (BMB), which is commonly used for suspensions of motile *E. coli*, however here, MB is BMB without 67 mM NaCl. We removed salt from the MB to reduce screening between tracer particles that were added to the same mixture. The removal of NaCl does not appear to dramatically change the behaviour of *E. coli* or alter our findings. We report observed behavioural changes of *E. coli* in appendix A.

2.3.3 Growth Protocols

The bacteria are stored on LB agar plates at 4 Celsius in a fridge and disposed of after 1 month. These plates were prepared by J. Schwarz-Linek and A. Dawson.

To prepare a batch of cells (AB1157 WT, ΔCheY or ΔCheZ), first overnight cultures are grown, inoculated from a single colony and grown aerobically in 10 mL LB in an orbital shaker at 30 Celsius and 200 RPM for $\sim$16 hours. A fresh culture is prepared by 1:100 dilution of the overnight culture into tryptone broth, which is grown in the same conditions for 4 hours. At this point, the culture is mid-exponential phase, at which point the growth is stopped by filtration and a single wash into MB, yielding a final optical density (OD) $\sim$ 7, corresponding to $c_B = 0.8 \times 10^{10}\mathrm{mL}^{-1}$. This protocol has been previously studied and optimised for motility [123] [60].

The growth protocol for AD10 required modification. First, 100 μg/mL ampicillin is added to all growth stages to minimise genetic mutations. Secondly, after growing in TB for 4 hours, the transcription of PR is then induced by the addition of 1 mM arabinose and the necessary co-factor all-trans-retinal to 10 μM and is allowed to grow for a further 75 minutes to allow expression to take place. The growth is again stopped by filtration and washing into motility buffer.

2.3.4 Note on Experimental Procedure

When in MB, i.e. a media without nutrients, the swimming speed of *E. coli* is observed to steadily decrease over time until oxygen is depleted, upon which swimming stops [123]. This decrease in motility in starvation conditions is not fully understood, however, to minimise its impact we run experiments in parallel (where possible). By running experiments at the same time, the variation in motility is minimised between samples.

2.4 Methods for Studying Dynamics

Within this thesis, the main experiments revolve around direct observations with a microscope. We use three types of microscopy, bright-field, phase-contrast and epifluorescence. We process the micrographs using two separate methods, particle tracking and differential dynamic microscopy (DDM). In the following sections, we will review the above-mentioned methods.

2.4.1 Transmission Light Microscopy

Bright-field microscopy is one of the simplest microscope techniques, where the sample is illuminated from behind and the image is directly transposed on to a camera. As the light passes through the sample, contrast is generated by absorption and refraction.

Both bright-field and phase contrast are set up with Köhler illumination. For bright-field, Köhler illumination aims to remove any imaging artefacts from the light source and increase contrast [161]. Light from the source passes through a collector lens which is then focused on to the condenser. After passing through

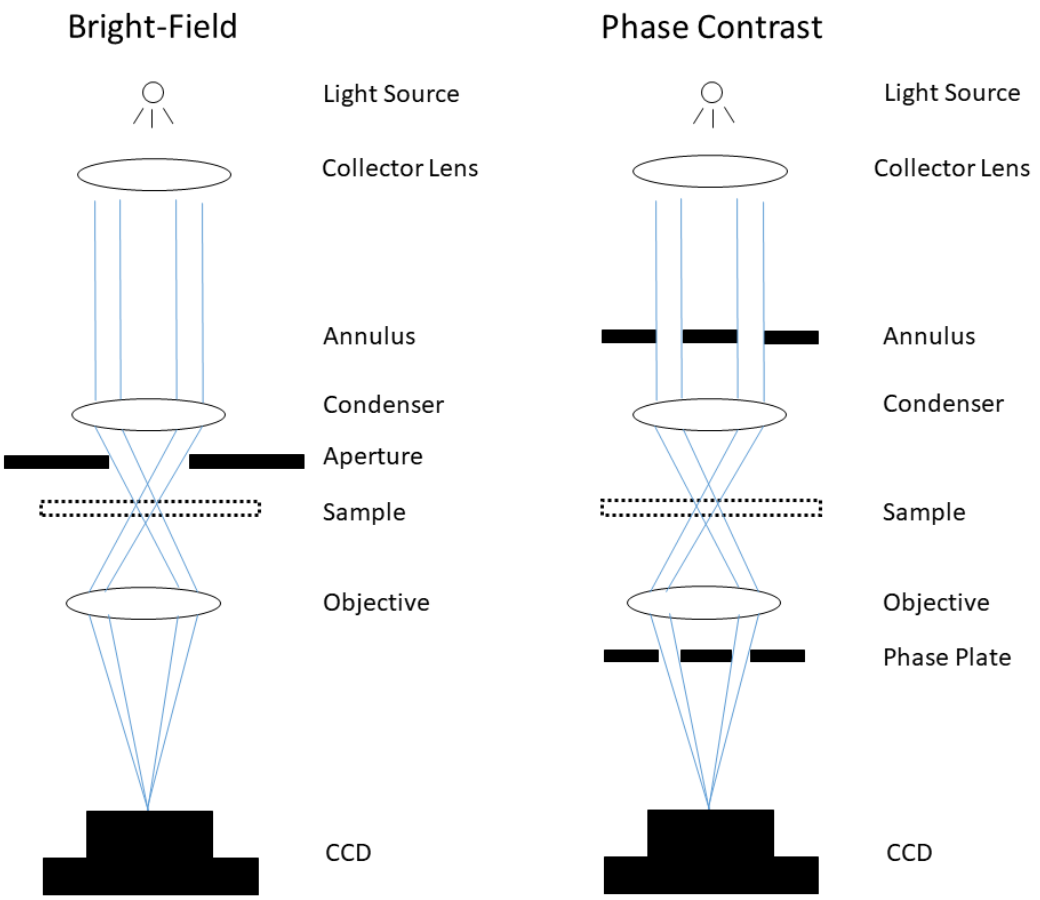

Figure 2.2 Simplified optical paths for left, bright-field and right, phase-contrast microscopes.

the condenser, light from each point on the source evenly illuminates each point on the sample. The image of the sample is then inverted as it passes through the objective, which is then captured by the camera. A simplified optical path for bright-field is depicted in figure 2.2.

Bright-field imaging of semi-transparent biological samples are generally low contrast, for such samples phase-contrast microscopy can be utilised for higher contrast imaging. Phase-contrast, as the name suggests, generates contrast in the final image from changes in the phase of the light.

In phase-contrast microscopy, a phase ring is added to the condenser, leaving only the most oblique illuminating light, figure 2.2. The condenser again focuses the light through the sample and into the objective forming a bright background. Semi-transparent cells, diffract the light which proceeds to destructively interfere with the background light. The use of oblique illumination emphasises the phase

shifts in the diffracted light increasing the contrast [161].

2.4.2 Epifluorescence Microscopy

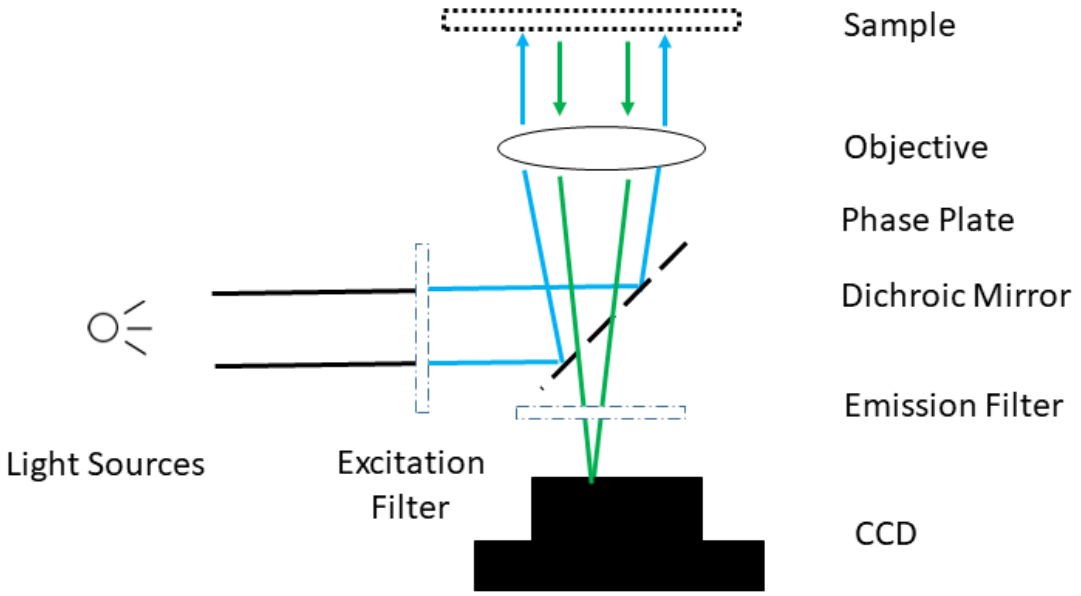

Figure 2.3 Simplified optical path used for epifluorescence microscopy.

Fluorescence is the emission of a photon from a molecule or atom as an electron decays from a raised energy level. The raised energy level is caused by the absorption of a photon from within a small band of wavelengths. Due to collisional relaxation occurring in the brief 1 μs window between absorption and emission, the emitted light is of higher wavelength (lower energy) than that initially absorbed. With careful choice of filters, the change in wavelengths means that the excitation source can be excluded from the imaging plane, allowing for the clear observation of the fluorescing object.

Fluorescence microscopy refers to microscopes that utilise fluorescence to observe the sample, epifluorescence microscopy refers specifically to the emission of excitation light from the objective (the same objective used for imaging). For parts of our work, we used an inverted epifluorescent microscope, for which a simplified layout is depicted in figure 2.3. We start with the excitation light source, here a mercury-vapour lamp with a neutral density filter (ND8) to reduce its intensity. The light is filtered to 450-490 nm by a Chroma EGFP filter cube

which is then reflected by a dichroic mirror into the objective and onto the sample. The dichroic mirror is key to epifluorescence as it reflects most of the excitation light while allowing the emission light to pass through. An emission filter is placed behind the dichroic mirror to minimise any of the excitation light proceeding to reach the camera. These experiments are also done in a dark room to further minimise any background light reaching the camera. The fluorescing sample can then be visualised as bright on a dark background.

We use epifluorescence to study polystyrene tracer particles from Invitrogen, which are labelled with an unspecified fluorescent dye which absorbs around $\sim$ 490 nm and emits $\sim$ 520 nm. We will use epifluorescence microscopy in chapter 5 to study the dynamics of fluorescent colloidal tracers in a bath of non-fluorescing *E. coli*.

2.4.3 Multiple Particle Tracking

Particle tracking is the process of identifying and locating particle centres over a time-lapsed series of images and then 'connecting the dots' to compile a trajectory. To track a large number of particles over long periods of time, algorithms are implemented to automate the process. The exact method used varies between project and research group as no universal best method exists [28]. Within this work, we opt to use simple methods, made possible by the use of high-quality experimental data (high frame rates and small pixels sizes) [28].

Here, we use a four-part process. First, the image pre-processed to improve clarity, then it is thresholded to identify particle locations, followed by a centre of mass (or centroid) calculation to find the sub-pixel location, then finally the linking of particle positions over time to create the trajectory.

To identify candidate particles, we note that the particles are significantly brighter than the background. To improve the signal, we convolve the image with the Gaussian kernel, resulting in blurring. For a two-dimensional image, the Gaussian filter is

$$G(x,y) = \frac{1}{\sqrt{2\pi\sigma}} exp^{-\frac{x^2+y^2}{2\sigma^2}} \tag{2.7}$$

where x and y are the distances from a central pixel and σ is the standard

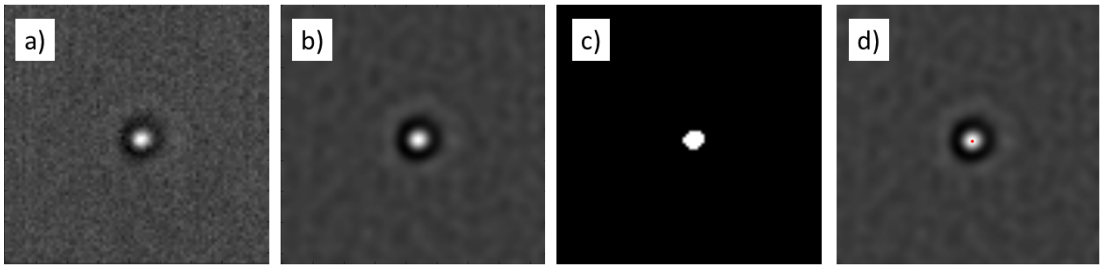

Figure 2.4 Example showing the visual process of identifying a particle and calculating its centre. a) raw image, b) pre-processed image, c) thresholded pre-processed image and d) the centre labelled in red on the pre-processed image.

deviation. This filter is applied to all pixels in an image. A raw image of a silica particle in bright-field is shown in figure 2.4a and the same image processed with a Gaussian filter, $\sigma = 2$, figure 2.4b.

Next, we threshold the image to identify the particles. To remove variations in illumination between experiments, we first subtract the average brightness of the image from the processed image and then threshold the image. The thresholded image is shown in figure 2.4c. The threshold is then used to then label each individual bright object in the image. While we did not need to, for each object, the number of pixels of a particle can be used to discriminate between real particles and dirt or dust.

For the pixels associated with each particle, the centre of mass is calculated, where the centre is [26]

$$C_x = \frac{\sum_{i=1}^{n} \sum_{i=j}^{m} x_i \cdot I_{ij}}{\sum_{i=1}^{n} \sum_{i=j}^{m} I_{ij}} \tag{2.8}$$

where I is the intensity matrix, for pixels above the threshold and C_x centre of mass in the x-axis. Figure 2.4d shows the identified centre (in red) on the processed image. This method identifies the particle centre to a sub-pixel level [28].

The centre of mass is a computationally inexpensive calculation, which is sufficient for our needs as long as no sub-pixel biasing is present [26]. Sub-pixel bias occurs when the particle spans over too few pixels and the identified centre shows bias towards the centre of a pixel (instead of finding a uniform distribution of sub-pixel locations). The presence of sub-pixel biasing is a problem for the study of

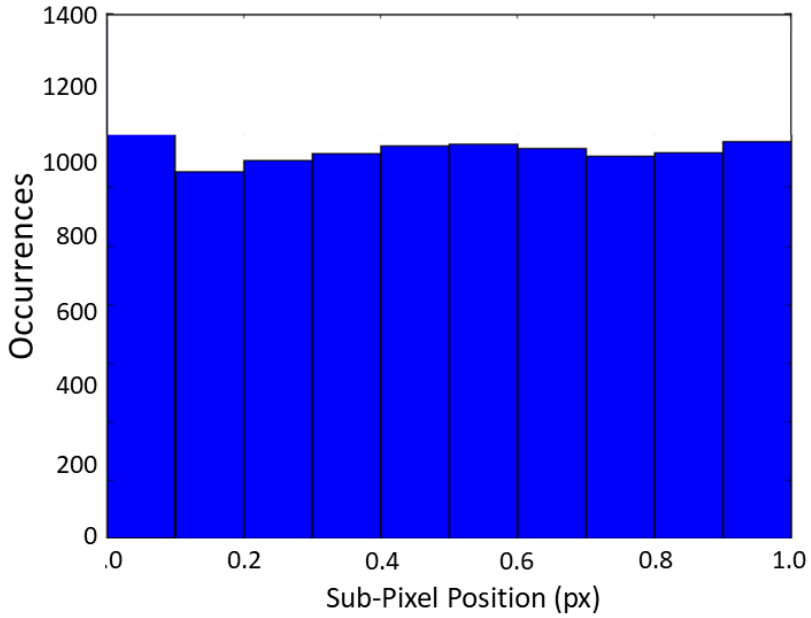

Figure 2.5 Histogram showing representative sub-pixel locations of particles.

particle displacements, where at short times, the biasing to a central pixel can cause the particle to appear stationary and then jump a large distance. In figure 2.5, we report a representative histogram of sub-pixel locations for the tracking used here, which shows a uniform distribution and no sub-pixel bias.

If sub-pixel biasing was present, other, more accurate and slower methods can be utilised to identify centres. A common, next best method is fitting the pixel intensities to a Gaussian in x and y, where the centre of the function is the particle centre [26] (which is not used in this thesis).

Finally, the particle locations are connected across frames to build each particle's trajectory. We identify the particles next location by finding the nearest neighbour method, i.e. the closest particle on the next frame. To ensure the trajectories do not 'jump' between particles, we impose a maximum range of the next frame of $\sigma/3$, for particle diameter σ, made possible by the use of high frame rate movies ($\sim$100 fps).

We use the results from particle tracking for calculations of the particles mean square displacement in chapter 4 and for structural analysis of clusters in chapter 7.

2.4.4 Intermediate Scattering Function

We also measure the intermediate scattering function, $f(q,\tau)$, to study both tracer and bacteria dynamics, using a method called differential dynamic microscopy. The ISF is a measure of structure correlation after a timescale τ over a length scale, $2\pi/q$, as given by the Fourier transform of the probability distribution function of particle displacements.

$$f(q,\tau) = \left\langle \sum_{j=1}^{N} e^{iq.(r(t+\tau)-r(t))} \right\rangle \tag{2.9}$$

where r is the displacement of the particle and $f(q,0) = 1$.

The ISF is commonly measured by dynamic light scattering and differential dynamic microscopy and requires fitting to a model to extract dynamic properties like diffusivity or swimming. For isotropic particles undergoing Brownian diffusion, where the displacement distribution is Gaussian, equation 2.9 reduces to [13]

subject to the condition that $f(q,0) = 1$

$$f(q,\tau) = e^{-Dq^2\tau} \tag{2.10}$$

For motile *E. coli*, the ISF is modelled assuming they swim on an infinitely straight trajectory with velocity v, $\delta r(\tau) = v\tau$. For an isotropic culture in three-dimensions, the ISF is [13]

$$f(q,\tau) = e^{-Dq^2\tau} \int_0^\infty P(v)\mathrm{sinc}(qv\tau)dv \tag{2.11}$$

where $P(v)$ is the distribution of bacteria velocities and the multiplicative factor $e^{-Dq^2/\tau}$ accounts for the Brownian motion experienced by the bacteria and the function $\mathrm{sinc}(x) = \sin(x)/x$. The velocity distribution, $P(v)$ is well modelled as a Schulz distribution [79]

$$P(v) = \frac{v^Z}{Z!}\left(\frac{Z+1}{\bar{v}}\right)^{Z+1} \exp\left[-\frac{v}{\bar{v}}(Z+1)\right] \tag{2.12}$$

where Z is related to the standard deviation, σ, by $Z = (\bar{v}/\sigma)^2 - 1$.

However, a third of an *E. coli* culture will typically be non-motile [79], described by a non-motile fraction, β, which undergo purely diffusive motion (the fraction of motile cells $\alpha = 1 - \beta$). After accounting for the non-motile cells, the ISF becomes

$$f(q,\tau) = e^{-Dq^2\tau}\left[(1-\alpha) + \alpha\int_0^\infty P(v)sinc(qv\tau)dv\right] \tag{2.13}$$

We will later make fits to equation 2.13, where, to reduce computing time, we make use of the simplification [79, 107]

$$\int_0^\infty P(v)sinc(qv\tau)dv = \left(\frac{Z+1}{Zq\bar{v}\tau}\right)\frac{\sin(Z\tan^{-1}\Lambda)}{(1+\Lambda^2)^{Z/2}} \tag{2.14}$$

where $\Lambda = (q\bar{v}\tau)/(Z+1)$.

For motile populations, this model of the ISF is only valid for $0.5 < q < 6\,\mu\mathrm{m}^{-1}$ [79, 162]. For large length scales, $q < 0.5\,\mu\mathrm{m}^{-1}$, the trajectories are no longer straight due to tumbling events or rotational diffusion. Whereas short length scales, $q > 6\,\mu\mathrm{m}^{-1}$, probe the precessive motion of the cells. While it is possible to access these q values with ultra-low-angle dynamic light scattering [95], the results are more readily accessible with differential dynamic microscopy.

2.4.5 Differential Dynamic Microscopy

The advent of Differential Dynamic Microscopy (DDM) has provided access to information on the dynamics of colloids while averaging over significantly larger populations than those accessible by tracking. DDM is an extension of light scattering, but instead of requiring a laser light source like traditional methods, DDM uses the more accessible optical light microscope with a camera and computer for analysis.

The raw input for DDM here is a high frame rate movie from a microscope of colloids undergoing diffusion or self-propulsion. The light intensity (pixel values) of each frame is described as $I(\vec{r},t)$ where $\vec{r}$ describes the imaging plane in terms of pixel position for a time, t. As particles move, the $I(\vec{r},t)$ changes accordingly. We then calculate the difference between frames $D(\vec{r},\tau) = I(\vec{r},t+\tau) - I(\vec{r},t)$ for

a time t and time difference of τ.

The Fourier transform of $D(\vec{r},\tau)$ is

$$F_D(\vec{q},\tau) = \int D(\vec{r},\tau) exp[i\vec{q}\cdot\vec{r}]d\vec{r} \tag{2.15}$$

Since the fluctuations in light intensity are due to the movement of colloids we assume

$$\Delta I(\vec{r},t) = \kappa \Delta\rho(\vec{r},t) \tag{2.16}$$

Where the constant κ is dependent on the imaging setup. Here we define $\Delta I(\vec{r},t) = I(\vec{r},t) - \langle I\rangle$ and $\Delta\rho(\vec{r},t) = \rho(\vec{r},t) - \langle\rho\rangle$

Combining equations 2.15 and 2.16 give

$$F_D(\vec{q},\tau) = \kappa[\Delta\rho(\vec{q},\tau) - \Delta\rho(\vec{q},0)] \tag{2.17}$$

Since we are studying continuous and homogeneous process, we average radially and the initial time t, from which we calculate the differential intensity correlation function, DICF

$$\left\langle |F_D(q,\tau)|^2 \right\rangle = A(q)[1 - f(q,\tau)] + B(q) \tag{2.18}$$

where the prefactor A(q) is

$$A(q) = 2\kappa^2 \langle [\Delta\rho(\vec{r},t)]^2 \rangle \tag{2.19}$$

and $f(q,\tau)$ is the intermediate scattering function

$$f(q,\tau) = \frac{\langle \Delta\rho(\vec{q},\tau)\Delta\rho(\vec{q},0)\rangle}{\langle [\Delta\rho(\vec{q},\tau)]^2\rangle} \tag{2.20}$$

The final term, B(q), is added to account for camera noise. The differential intensity correlation function can be fit using an appropriate form of the intermediate scatting function.

DDM has two separate uses within this thesis, firstly for measuring the diffusivity

of colloids in the bulk (as we report in chapter 5) and secondly to characterise bacterial motility and note batch-to-batch variations.

Here, we report representative results from DDM for samples of *E. coli* in motility buffer with glucose, the bacteria concentration, $c_B = 5.1 \times 10^8$ μm^{-3}. The movie was recorded in phase-contrast illumination (10×/0.3 NA Ph1 objective) at 512×512 pixels (where pixel size = 1.4 μm/px for $\sim$ 4000 images at 100fps. These are bulk measurements, where the objective is focused 100 μm up from the bottom of a 400 μm high capillary. These setup parameters (bacteria density, objective, frame rate, etc.) were previously optimised for the signal to noise ratio [79].

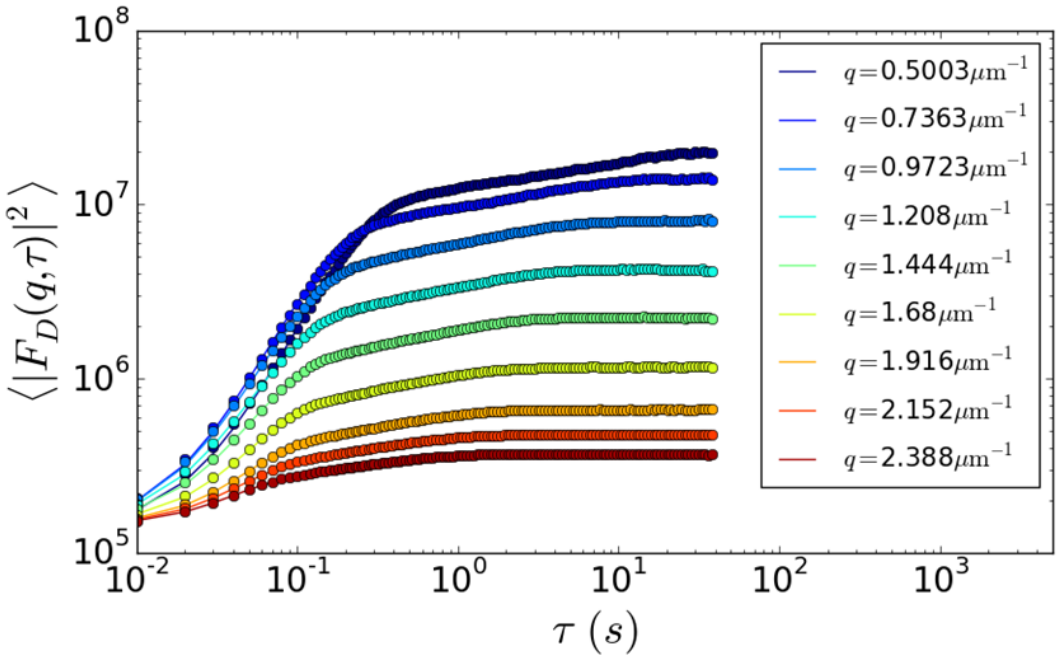

Figure 2.6 The differential intensity correlation function as measured by DDM (points) and the fits to equation 2.13 for a range of q. The sample is WT *E. coli* (bacteria concentration, $c_B = 5.1 \times 10^8$ μm^{-3}) in motility buffer with glucose, 5 minutes after sealing the capillary.

The differential intensity correlation function is calculated and then plotted in figure 2.6 (points) and the fits using equations 2.18 and 2.13 are also plotted (lines). The value of the DICF is for $\tau \to 0$, $\left\langle |F_D(q,\tau)|^2 \right\rangle = B(q)$ and for $\tau \to \infty$, $\left\langle |F_D(q,\tau)|^2 \right\rangle = A(q) + B(q)$, where the intermediate form is determined by the intermediate scattering function.

The fitting of the DICF yields 6 variables as a function of q, shown in figure 2.7.

For this example, averaging in the range $0.5 < q < 2.4\,\mu\text{m}^{-1}$, we extracted $D = 0.51 \pm 0.03\ \mu m^2 s^{-1}$, $v = 17.7 \pm 0.3\ \mu m s^{-1}$, $\beta = 0.37 \pm 0.02$, $Z = 1.74 \pm 0.20$, where the errors correspond to the variance in q. Here, Z appears slightly q-dependent, this only corresponds to a small increase in the standard deviation of the velocity distribution at high q.

$A(q)$ is the only fitting parameter with significant q-dependence, which occurs due to the strong q-dependence of the form factor of the bacterium and imaging setup [79]. Further, ratios of $A(q)$ between samples can be used as a measure of the relative sample density [5].

The velocity has slight q-dependence based on the swimming mode [79]. For swimmers with infinitely straight trajectories, which are recorded with an infinite depth of field, the velocity will have no q dependence. However, if the bacteria undergo run-and-tumble motion, for length scales longer than the persistence length, bacteria are swimming further than the length probed by DDM, making them appear slower for smaller q. Alternatively, smooth swimmers can swim out of the imaging plane, which makes them appear to swim faster for smaller q.

DDM can also be used with recordings from epi-fluorescent setups (or fluorescence DDM, fDDM). If for example you have mixed populations of fluorescent colloids and non-fluorescent bacteria, the fluorescence movies detail the dynamics of the colloids alone [59]. Subsequent DDM analysis yields information of the fluorescent colloids alone. We will use fDDM for this purpose in chapter 5.

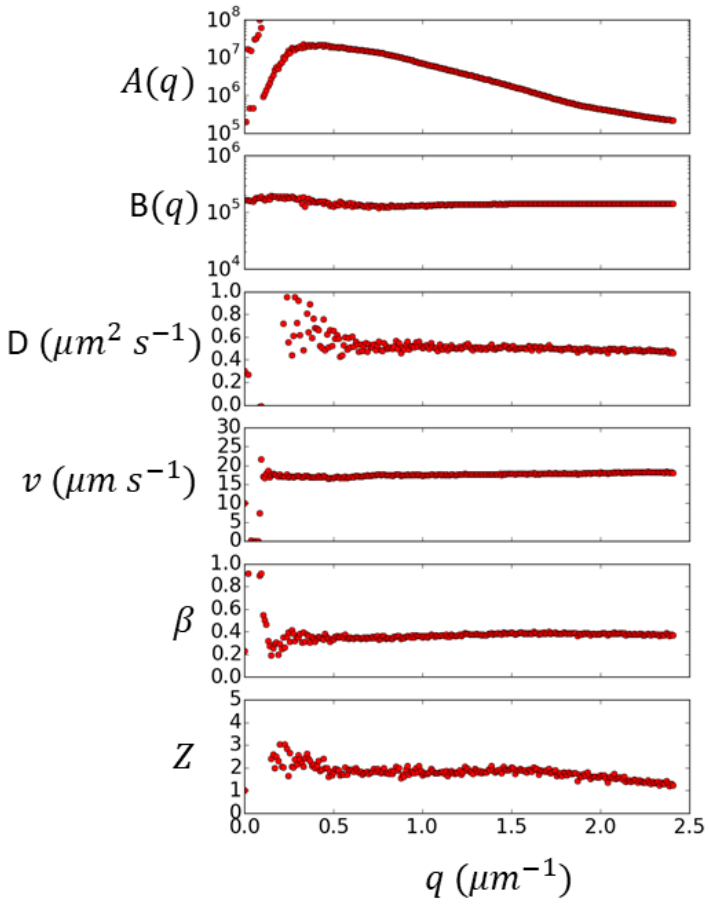

Figure 2.7 Fitting parameters for DDM corresponding to the fits shown in figure 2.6, for a sample of WT *E. coli* (bacteria concentration, $c_B = 5.1 \times 10^8$ μm^{-3}) in motility buffer with glucose, 5 minutes after sealing the capillary.

Chapter 3

Introduction to Enhanced Diffusion

In the context of this work, the enhanced diffusion of a micron-sized tracer particle is the process by which the diffusivity is increased due to the presence of active swimmers. In this chapter, we will review the key mechanisms which lead to enhanced diffusion.

3.1 Enhanced Diffusion by Collective Motion

Enhanced diffusion was first observed by Wu and Libchaber [164] in a mixture of tracer particles and motile *E. coli*. They started with a free-standing soap film which was ~ 10 μm thick in which passive particles exhibited diffusive motion [29]. To the film, they added large quantities of motile *E. coli*, up to bacterial concentrations of 5.35×10^{10} mL^{-1}, sufficient to induce collective motion, the formation of short-lived vortices much larger than individual bacteria. Upon addition of motile bacteria to the sample, they observed two changes to the mean square displacement of tracer particles, their results are reproduced in figure 3.1. At short times, $t < t_c$, the tracers are observed to be superdiffusive, i.e. the mean square displacement increases with t^x for $1 < x < 2$. For long times, $t > t_c$, the tracer behaves diffusively, where $x = 1$, with an effective diffusion constant that is higher than the passive diffusivity. This behaviour was observed for tracers of diameter 4.5 and 10 μm.

By integrating the velocity autocorrelation function, Wu and Libchaber obtained an expression for the mean square displacement [164]

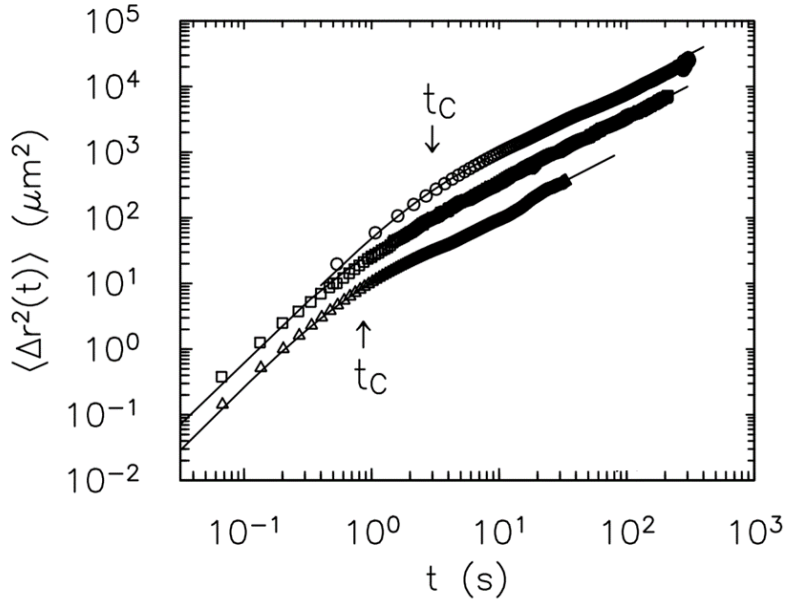

Figure 3.1 Mean square displacements of 10 μm diameter beads in an active bath, taken from [164]. Each dataset corresponds to a different bacterial concentration where triangles, squares and circles correspond to 0.67, 1.34 and 5.35 $\times 10^{10}\,\mathrm{mL}^{-1}$. The timescale t_c detailing the crossover from superdiffusive to diffusive behaviour is obtained from fitting to equation 3.1 and is marked for the highest and lowest bacterial concentrations.

$$\langle \Delta r^2 \rangle = 4Dt\left[1 - e^{-t/t_c}\right] \tag{3.1}$$

where D describes the total long-time diffusivity. By fitting their mean square displacements to equation 3.1, they observe that both D and t_c increase with increasing bacterial concentration. The increase in t_c is observed to correlate with an increase in the lifetime of the vortices.

Grégoire *et al.* reported a model for the Wu and Libchaber experiments based on a Vicsek model [52], where the bacteria orient to align with neighbours within a cut-off radius with an additional noise term. The bacteria in these systems are able to align due to their long-range hydrodynamic flow fields. These simulations confirmed the emergence of enhanced diffusivity due to the presence of collective motion and validate that the timescale t_c describes the vortex lifetime. They also found that enhanced diffusion could originate from steric, hydrodynamic interactions or a mixture of the two.

Valeriani *et al.* replicated both experimental and simulation results for 4 μm diameter polystyrene tracers trapped between two glass coverslips separated by 5-7 μm in a bath of *B. subtilis*, which are approximately 4 μm in length and 1 μm in width [146]. This setup is also quasi-two-dimensional, but the confinement minimises particle drift. They semi-quantitatively reproduced their experimental results with simulations which omitted hydrodynamic interactions, highlighting that steric effects play an important role in enhanced diffusion.

3.2 Enhanced Diffusion due to Single Scattering Events

While initial work focused on collective behaviour, this is not required to enhance the diffusion of tracer particles. There has been extensive work investigating how tracers interacting with a single active particle can result in enhanced diffusion, this work is reviewed within this section.

Leptos *et al.* used a predictive algorithm to track tracer particles in three-dimensions, 100 μm from a surface [72]. They studied the diffusion of 2 μm diameter polystyrene tracers in a bath of *C. reinhardtii*, a spherical algae with a radius of 5 μm, which swim by beating their two flagella in a 'breaststroke' pattern pulling the bacteria forward. These are fast swimmers, here the mode of the speed distribution was identified as $\sim$ 100 μms^{-1}. Unlike the bacteria used in previously reported studies, the algae used here are 'pullers' which are not observed to undergo collective motion [152]. Enhanced diffusion of the tracers occurs when a cell swims within $\sim$ 25 μm of the tracer, $\sim$ 8 μm out of the reach of the flagella, where the tracers are observed to form loop-like trajectories. Example trajectories are shown in figure 3.2. The formation of loops is found to correlate with the beating motion of the flagella. Note, these experiments are also found to exhibit the linear increase in tracer diffusivity with increasing bacterial concentration.

Numerical and theoretical studies have since validated the observation that single active-passive scattering events result in quasi-closed loops of the passive tracer, where the tracers are displaced due to far-field advection [38, 108, 166]. The structure of the loop and direction of the tracer's motion is dependent on the flow field and thus the specific swimmer. In the limit of a swimmer, swimming

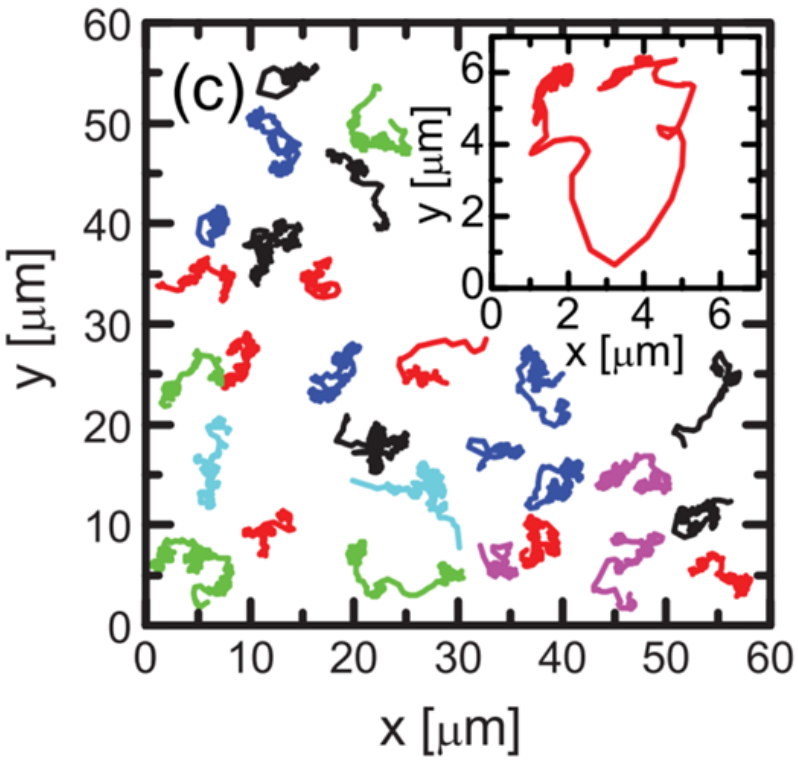

Figure 3.2 Taken from [72]. Experimental tracks of 2 μm diameter polystyrene tracers with loop-like trajectories induced by scattering events with *C. reinhardtii*. The inset focuses on an individual tracer.

on an infinitely straight trajectory which moves significantly faster than the induced motion of the tracer, it is found that the symmetry of the swimmer's hydrodynamic flow field results in the tracer moving in a perfect loop. In order for enhanced diffusion to occur, the tracers must not move in perfect loops and therefore one of the following criteria must be fulfilled. Firstly, the swimmer can undergo reorientation during the scattering event, this is often interpreted as a tumbling event [108, 166]. Secondly, if the tracer is displaced at similar velocities to the swimmer, the tracer will move with the swimmer initially, and when the swimmer passes, the tracer moves quickly in the opposite direction (i.e. the tracer is pushed in one direction more than the other). This asymmetric experience of the flow field results in net displacement. An extreme limit of this is entrainment, the process by which the tracer is caught in the fluid being dragged along with the swimmer.

Further experimental studies verified that at these low swimmer concentrations, scattering events still enhance tracer diffusivity for quasi-two-dimensional [87] and three-dimensional systems [59]. For these low concentrations, the number

Paper	Swimmer	Tracer Diameter (μm)	z (μm)	β μm^4
[87]	Janus Rods	1 and 2	At surface	13
[87]	*E. coli* (WT)	1 and 2	At surface	5
[88]	*E. coli* (WT)	2	5-110	10-50
[59]	*E. coli* (WT)	*E. coli* (NM)	100	7.1
[72]	*C. reinhardtii*	2	100	500
[58]	*C. reinhardtii*	1	13	900

Table 3.1 Values of β reported for various experimental systems. The tracers used in [59] are non-motile *E. coli* cells, all others used spherical particles.

tracer-swimmer scattering events increase linearly with the active flux, $J_A = vc_B$, where v is the mean swimmer speed and c_B is the swimmer (or motile bacteria) concentration. The total effective diffusivity is described by

$$D_{eff} = D_0 + \beta J_A \tag{3.2}$$

where D_0 is the tracer's diffusivity in the absence of swimmers. The constant β, which is not fully understood, is a length scale to the fourth power, the value is known to depend on the swimmer's propulsion mechanism, large changes in tracer diameter and the distance to a surface (z) [58, 59, 87, 88, 99]. Values of β have been reported for several experimental systems, summarised in table 3.1. The reported values for β range from 5 μm^4 for 2 μm diameter beads at a surface in a bath of WT *E. coli* [87] up to values of $\sim$ 900 μm^4 for 2 μm diameter beads in the bulk in a bath of *C. reinhardtii* [58].

Several simulation and theoretical works have focused on modelling *E. coli* and determining the underlying mechanism and developing an understanding of the origin and meaning of the constant β [90, 108–110, 166]. These works rely on the same set of assumptions. Based on measurements of the flow field of *E. coli* by Drescher *et al.* [37], swimmers are modelled as point dipoles, which accurately describes far-field interactions. The point-dipole model overestimates the near-field flow and completely omits steric interactions, instead, a short-ranged cut-off is introduced, defining a minimum distance in which tracers interact with the swimmers flow field. The tracer particles are also described as point particles because for tracers of interest (tracers of size $\sim$1 μm), the fluid velocity does not change significantly over their size. Tracer particles can then be assumed to move at the same velocity as their surrounding fluid. Finally, the

swimmer's finite persistence length is described by an infinitely straight trajectory interspersed with instantaneous tumbling events, randomising the swimmer's direction. Pushkin *et al.* show that these tumbling events can be viewed as equivalent to reorientation due to rotational diffusion [108].

All of these models capture the short-time superdiffusive behaviour and long-time enhanced diffusivity and reproduce to reasonable accuracy the constant β [90, 108–110]. As such, they advocate for the mechanism of enhanced diffusion due to reorientations of swimmers during a scattering event. These models agree that β is a strong function of the system's parameters such as system size, dipole strength and persistence length. They also find a small contribution to the diffusion enhancement due to entrainment effects, the process of the tracer being dragged along with fluid near the swimmer's surface, leading to large displacements [90, 110].

Theory and numerical calculations by Kasyap *et al.* found that enhanced diffusion is highly dependent on the Brownian diffusivity, i.e. tracer diameter, including the presence of a peak in the enhanced diffusion [63], which has since been verified by experiments [99]. These works identified a maximum in the diffusion enhancement for a given Brownian diffusivity, where the enhancement decays towards zero for high Brownian diffusivity and decays to a constant value for low Brownian diffusivity. The peak can be attributed to the tracer's ability to asymmetrical probe the swimmer's flow field resulting in larger net displacements. Whereas, for high Brownian diffusivities, the tracer freely diffuses through the swimmer's flow field and therefore, on average, probes the flow field symmetrically.

For baths of pullers, for example, *C. reinhardtii*, as opposed to the pushers described above, entrainment has been observed to be the dominant mechanism leading to enhanced diffusion [58, 82]. These extreme cases are directly observable due to the tracer trajectories exhibiting diffusive motion interspersed with large linear displacements where entrainment events occurred. These large displacements due to entrainment result in values of β which are $\times 100$ larger for *C. reinhardtii* than *E. coli*.

So far, the primary interest has been in the long-time diffusivity of the tracer particle. Koumakis *et al.* measured the mean square displacement of 2 μm diameter silica particles in a bath of *E. coli* (WT) at 100 frames-per-second [66]. To fit the short-time mean square displacements, they modelled the velocity autocorrelation function as the sum of active and Brownian effects, giving

$$\langle \Delta r(t)^2 \rangle = 4D_0 t + 4D_{act}\left[t - t_c\left(-e^{-t/t_c}\right)\right] \tag{3.3}$$

where D_{act}=βJ_A, so at long-times ($t \gg t_c$) the diffusivity is the sum of the Brownian and activity enhanced diffusivity, D=$D_0 + D_{act}$ or for short times($t \ll t_c$), the diffusivity, D=D_0. Their experimental results and fits to equation 3.3 are shown in figure 3.3. This form used by Koumakis *et al.* is equivalent to that used by Wu *et al.* (equation 3.1) for $t \gg t_c$ [164].

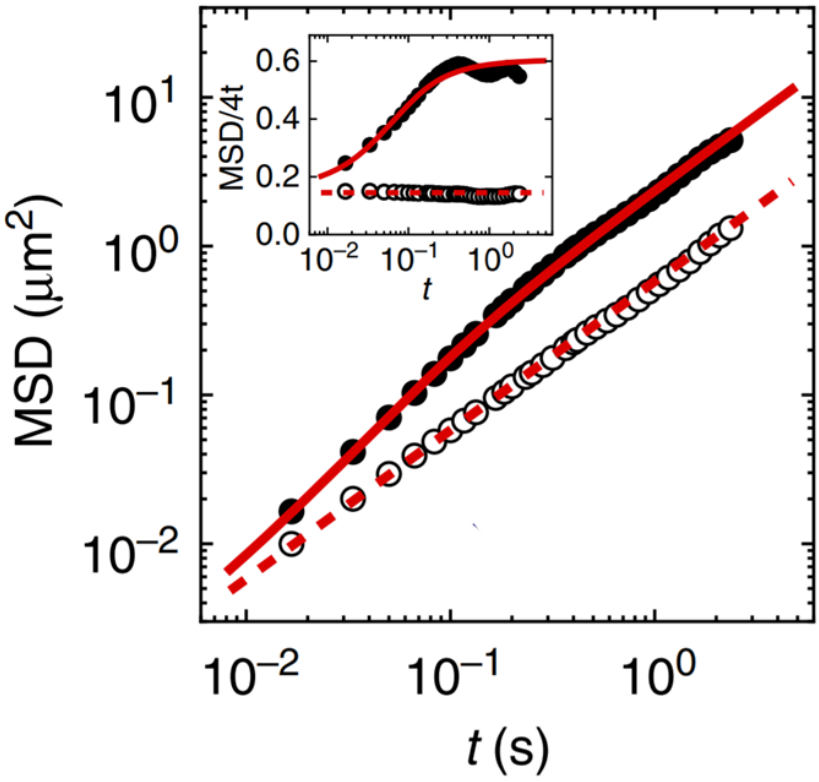

Figure 3.3 Taken from [66]. Experimental measurements of the mean square displacements and fitting to equation 3.3

Within this thesis, we focus on smooth-swimming bacteria, for which it is suggested that enhanced diffusion is reduced (relative to run-and-tumble swimmers) [59]. The majority of our work is in quasi-two-dimensional systems, where long-ranged hydrodynamic flows are suppressed [37], thus minimising these long-ranged interactions [90]. We will however return and question the importance of bacterial persistence length in the models mentioned above.

Chapter 4

Activity Enhanced Diffusion in Two Dimensions

The diffusivity of a colloidal tracer particle is known to be enhanced in an active bath due to a range of hydrodynamic and steric mechanisms. In this chapter we investigate how changing the interaction potential between passive and active particles can affect the enhancement of diffusivity for a quasi-two-dimensional system.

The model for the average z of tracers was given by W. Poon.

4.1 Methods

In this chapter, we use 1.5 μm diameter silica particles in a phosphate buffer in a 400 μm high rectangular capillary made of borosilicate glass. The particles sediment to the surface over 5 minutes upon preparation, where they are observed to diffuse. To these samples, we will add motile bacteria, smooth swimming E. coli (AB1157 ΔCheY). We also add a polymer depletant, polystyrene sulphonate of radius of gyration, $r_g = 45$ nm.

To study the tracer's dynamics we track each particle's displacement over time. We use movies recorded in bright-field for tracking of tracer particles, as this retained information about the bacteria as well. In bright-field, the tracer particles appear significantly brighter than the bacteria as they scatter light more

efficiently, meaning tracers can be detected by brightness alone.

4.1.1 Tracking Corrections and Filtering

This chapter focuses on results from particle tracking, for which there are two main sources of error. Firstly static error, the error associated with accurately locating a static particle. For our purposes, static errors are sufficiently minimised by insuring no pixel-biasing is present, as discussed in section 2.4.3 [120]. Secondarily, there are dynamic errors which arise from the finite exposure time of each image. These dynamic errors can be thought of as a blurring effect, arising from the particle moving during the exposure time. Effects of dynamic errors can be ignored when the exposure time is less than a quarter of the time between frames [120], therefore, we set the exposure time to 2 ms for imaging at both 100 and 10 frames per second.

Next, there are experimental sources of error. Sample preparation is optimised to minimise hydrodynamic flows within the capillary by sealing the capillary with a minimal volume of air remaining, but some flows do remain causing all particles in the field of view to drift and unintentionally enhance particle motion. These flows enhance particle diffusion by removing isotropic behaviour. We correct for these small errors by enforcing the isotropic criteria with corrections to all particle tracks. From each movie, we extract ∼30 trajectories and ensure that total average displacements in x and y displacements are zero for each frame in the video

$$\begin{aligned} \langle \Delta x(t) \rangle &= \sum_i \Delta x_i(t) \\ \langle \Delta y(t) \rangle &= \sum_i \Delta y_i(t) \end{aligned} \tag{4.1}$$

Which for particle i on frame t, makes the corrected displacement

$$\begin{aligned} x_i^{\mathrm{c}}(t) &= x_i(t) - \langle \Delta x(t) \rangle \\ y_i^{\mathrm{c}}(t) &= y_i(t) - \langle \Delta y(t) \rangle \end{aligned} \tag{4.2}$$

So, $\langle x_i^c(t)\rangle = \langle y_i^c(t)\rangle = 0$. These corrected trajectories are then used for analysis. For our experiments, drift typically accounts for $< 2\%$ of a particles displacement.

Throughout this chapter, we will examine samples with sufficient polymer depletants to cause aggregation of tracer particles. This process dramatically reduces particle diffusivity and is an effect we do not want to study here. To minimise the number of interacting particles in the sample the particle area fraction is kept low, $\phi_c = 10^{-3}$, and the measurements are completed as fast as possible after sample preparation, generally taking 15-20 minutes to complete. Some aggregation is unavoidable however, we identify these trajectories by frame-to-frame proximity, where if two particle centres are detected within two particle diameters, the tracks are omitted from the final results.

Further filtering is required because some particles adhere to the surface and become non-diffusive. These particles can be filtered by fitting individual mean square displacements, $\langle \Delta r^2(\tau)\rangle \propto \tau^k$ [156]. For each tracer, if the exponent $k < 0.7$, the track is omitted.

To probe short and long time delays we image each sample at 100 and 10 frames per second, and average over 7 and 5 positions respectively for 1000 frames each. We reported a combination of these two datasets.

4.1.2 Polymer Concentration

We are interested in how depletion forces between a spherical tracer and spherocylinderical bacterium effect enhanced diffusion. Here, we control the force by the addition of polymer depletants. However, as the bacterium is not radially symmetrical, the overlapping excluded volume is dependant on orientation. The two extremes of the orientation are depicted in figure 4.1, which can be approximated as a) two spheres in contact ('head-on') and b) a sphere in contact with a cylinder ('side-on').

To simplify the system, we approximate the radius of both the cylinder and sphere to be equal $\sigma_c/2 = \sigma_s/2$, where the potential, U, for the 'head-on' orientation becomes that of two identical spheres [71].

$$U_{s-s} = -\frac{3}{2}\phi_p^{free} k_B T \left(\frac{1+\xi}{\xi^3}\right)\left(\frac{r}{\sigma} - 1 - \xi\right) \tag{4.3}$$

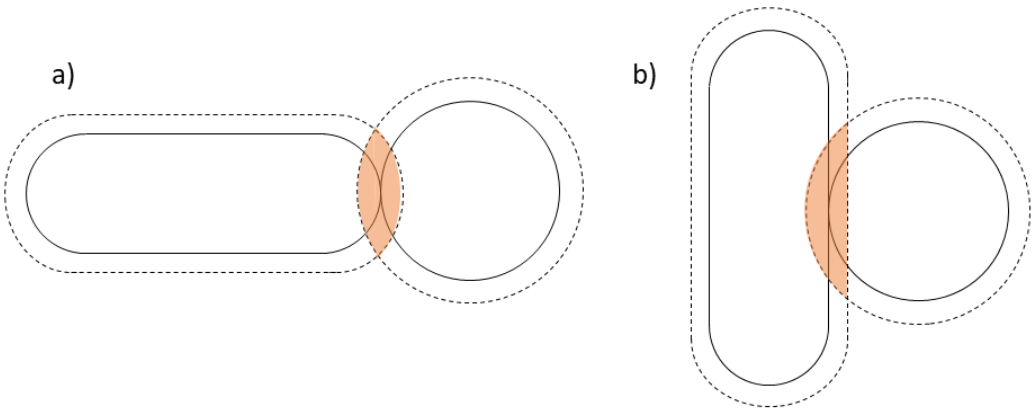

Figure 4.1 Depiction of the overlapping excluded volumes for a spherical tracer particle and a spherocylinderical bacterium in contact for two extremes of the orientation. The polymer excluded volume is depicted as a dotted line and the overlap is labelled in orange for a) 'head-on' b) 'side-on'.

where ϕ_p^{free} is the polymer volume fraction in the available free volume, ξ is the polymer-colloid size ratio, r is the distance between two particles and σ is the colloid diameter.

The potential for the 'side-on' orientation is that of a sphere and a cylinder [69]

$$U_{c-s} = -\frac{3}{\sqrt{2}}\phi_p^{free} k_B T \left(\frac{1+\xi}{\xi^3}\right)\left(\frac{r}{\sigma} - 1 - \xi\right) \tag{4.4}$$

The difference between these two limits is a factor of $\sqrt{2}$ for all values of r.

The bacteria and tracer concentrations remain low throughout this work, therefore we say $\phi_p^{free} \approx \phi_p$, where $\phi_p = c_p/c_p^*$. We will refer to ϕ_p throughout this chapter as a measure of the interaction potential. The largest polymer concentration used here, $\phi_p = 0.893$, corresponds to a contact potential, $U_{\text{contact}} =$ 18-25 $k_B T$ depending on orientation. For these calculations, we used the average radius between the bacterium and tracer, $r = (0.43 + 0.75)/2\,\mu\text{m} = 0.59\,\mu\text{m}$ and polymer radius of gyration, $r_g = 44.8$ nm.

Finally, as we shall explore in the next section, we also need to be aware of depletion between the tracers and the wall [71].

$$U_{w-s} = -3\phi_p^{free} k_B T \left(\frac{1+\xi}{\xi^3}\right)\left(\frac{r}{\sigma} - 1 - \xi\right) \tag{4.5}$$

which again scales linearly with the polymer concentration.

4.2 Brownian Diffusion on a Surface

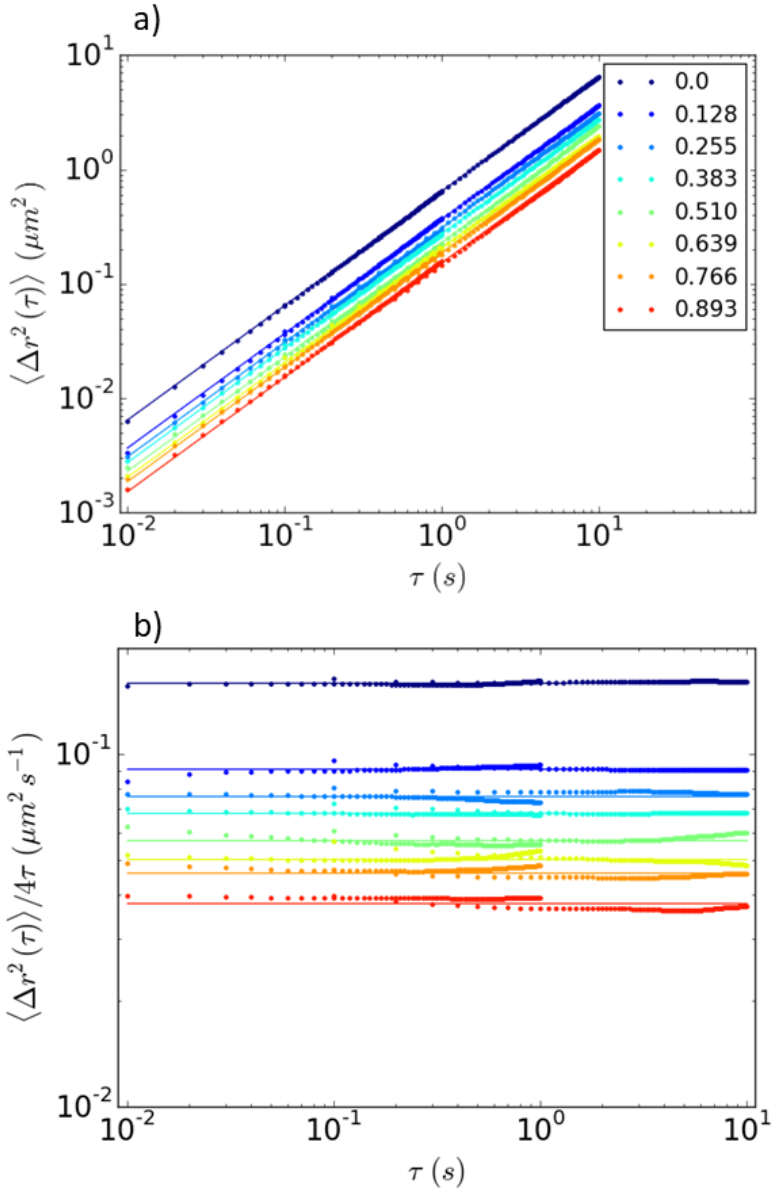

Figure 4.2 Mean square displacements of monomeric tracer particles for a range of polymer concentrations, ϕ_p. a) Mean square displacement. b) Mean square displacements are divided by 4τ to give the effective diffusion constant as a function of the timescale, τ. Both are fitted with Brownian diffusion models, equation 4.6

To understand how activity alters the diffusive properties of a tracer particle, we

must first measure the tracer particle's passive diffusive behaviour. The mean square displacement, $\langle \Delta r^2(\tau) \rangle$ of a passive tracer particle on a surface is [104]

$$\langle \Delta r^2(\tau) \rangle = \langle (r(t+\tau) - r(t))^2 \rangle = 4D_0\tau \tag{4.6}$$

where $\langle \Delta r^2(\tau) \rangle$ is the average over all starting times t, D_0 is the diffusion constant and τ is the delay time

The mean square displacement, $\langle \Delta r^2(\tau) \rangle$, of passive tracers over a range of polymer concentrations are plotted in figure 4.2a. Each dataset is comprised of short-time data recorded at 100 frames per second and long-time data recorded at 10 frames per second. The straight lines are fits to equation 4.6. These datasets are replotted as $\langle \Delta r^2(\tau) \rangle / 4\tau$ in figure 4.2b, with corresponding fits to equation 4.6. This plot shows the effective diffusion constant as a function of delay time. The effective diffusion constants are expected and found to be invariant with delay time. As polymer concentration is increased, viscosity increases, reducing the Brownian diffusion constant [104]

$$D_{\text{Brownian}} = \frac{k_B T}{6\pi\eta R} \tag{4.7}$$

where k_B is the Boltzmann constant, T is the temperature, η is the viscosity and R is the tracer radius. For the tracers used here, $D_{\text{Brownian}} = 0.30\ \mu\text{m}^2\text{s}^{-1}$

The diffusion constants extracted from the fitting in figure 4.2a are plotted as a function of solution viscosity, η, in figure 4.3 with the polymer concentration, ϕ_p, on the upper x-axis. The measured diffusion constant, D_0 is lower than the theoretical values, D_{Brownian}, because of increased hydrodynamic drag due to proximity to the capillary surface. This effect can be understood by considering that fluid at the surface of the particle is dragged along with the particle, called a no-slip boundary. The surface also a no-slip boundary, so the displacement of a particle near the surface generates large velocity gradients in the fluid, obstructing the flow and limiting particle motion [48]. The relationship between the theoretical and measured values is described by [42]

$$\frac{D_0}{D_{\text{Brownian}}} = \alpha(z) \tag{4.8}$$

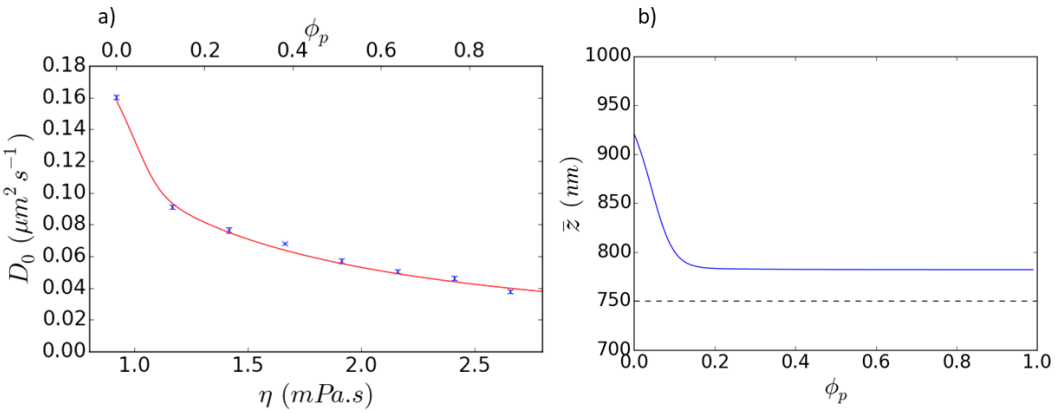

Figure 4.3 a) The passive diffusion constants of tracer particles on the capillary surface as a function of solution viscosity, η and polymer volume fraction ϕ_p, on the second x-axis. Our theoretical prediction for D_0 which accounts for the proximity of a surface, given by equation 4.14, is plotted as a red line. b) Our prediction of $\bar{z}$ corresponding to the theory plotted in a), the dotted line represents the tracer's radius, R, closest a particle can get to the surface.

and

$$\alpha(z) = 1 - \frac{9}{16}\left(\frac{R}{z}\right) + \frac{1}{8}\left(\frac{R}{z}\right)^3 - \frac{45}{256}\left(\frac{R}{z}\right)^4 - \frac{1}{16}\left(\frac{R}{z}\right)^5 \tag{4.9}$$

where z is the distance from the surface to the particle centre.

The measured diffusivity can then be expressed as

$$D_0 = \alpha(z)\frac{k_B T}{6\pi\eta R} \tag{4.10}$$

In our experiments, the distribution of particle height, z, is determined by a gravitational potential and when in proximity, depletion to the wall. The depletion forces attract particles close to the wall, keeping tracers closer to the wall as ϕ_p increases and therefore reduce the average tracer height. The potential experienced by a tracer particle is then

$$U^{\mathrm{w}}_{\mathrm{tot}}(z) = \begin{cases} \infty & z \leq R \\ U^{\mathrm{w}}_{\mathrm{d}}(z) + U_{\mathrm{g}}(z) & R < z < R + 2r_g \\ U_{\mathrm{g}}(z) & R > z + 2r_g \end{cases} \tag{4.11}$$

where depletion potential to the wall, $U_{\mathrm{d}}^{\mathrm{w}}(z)$, is given by equation 4.5.

The distribution of particles in z is [104]

$$\frac{n(z)}{n(0)} = exp\frac{-z+R}{z_0} \tag{4.12}$$

Which gives the gravitational potential

$$\frac{U_{\mathrm{g}}(z)}{k_B T} = \frac{z-R}{z_0} \tag{4.13}$$

where the gravitational length, $z_0 = k_B T/\Delta m g = 0.23$ μm,for a buoyant mass, Δm, and the acceleration due to gravity, g [104]. Note z_0 describes the height of point masses and not particles of radius, R, meaning that the tracers will be close to the surface due to gravitational forces alone.

We predict a near-wall average diffusivity of

$$\bar{D_0} = \frac{D\int_0^\infty \alpha(z) e^{-U_{\mathrm{tot}}^{\mathrm{w}}/k_{\mathrm{B}}T}\,\mathrm{d}z}{\int_0^\infty e^{-U_{\mathrm{tot}}^{\mathrm{w}}/k_{\mathrm{B}}T}\,\mathrm{d}z} \times \frac{\eta_0}{\eta_{\mathrm{p}}} \tag{4.14}$$

Results from equation 4.14 are plotted against the experimentally measured values in figure 4.2a and the corresponding prediction for $\bar{z}$ is plotted in figure 4.2b. Our prediction of D_0 matches experimental measurements. For $\phi_p > 0.2$, the average height is constant, $\bar{z} - R \approx 30$nm, within depletion range of the wall, $2r_g = 89.6$ nm. In this constant $\bar{z}$ regime, the measured diffusivity decreases as the polymer concentration increases due to increasing viscosity.

For $\phi_p < 0.2$, the reduction in depletion forces results in an increased sediment height, for $\phi_p = 0.0$, $\bar{z} - R = 170$ nm, slightly smaller than $z_0 = 230$ nm. Note, $\bar{z} - R$ is only a direct measure of z_0 in the limit $R \to 0$.

The variation in $\bar{z}$ for small ϕ_p may introduce a systematic error for our samples where $\phi_p = 0.0$. For small increases in the height from the surface, enhanced diffusion due to hydrodynamics is expected to increase [110], which may cause enhanced diffusivities to initially decrease with polymer concentration (for $\phi_p < 0.2$).

4.3 Activity Enhanced Diffusion

The mean square displacements are measured for tracer particles in an active bath of surface concentration, $c_B = 5.7 \times 10^{-3}\,\mu\text{m}^{-2}$ for the same range of attraction strengths as previously for passive samples. In this section, we reproduce the derivation for the mean square displacement of activity enhanced tracers [13, 66] and fit the model to our findings.

To start, we describe the displacement of a tracer particle as the integral of its velocity in one-dimension

$$r(t) = \int_0^t dt' v(t') \tag{4.15}$$

Therefore the mean square displacement is as follows

$$\langle r(t)^2 \rangle = \int_0^t dt' \int_0^t dt'' \langle v(t') v(t'') \rangle \tag{4.16}$$

Since this is a stochastic process and independent of starting time, the velocity correlation function can be rewritten as

$$\langle v(t') \cdot v(t'') \rangle = \langle v(\tau) \cdot v(0) \rangle \tag{4.17}$$

where $\tau = t'' - t'$ and $d\tau = -dt''$

To further utilise the time independence, we note that the integral in equation 4.16 is a square defined by t' and t''. For half of the integral $t' < t''$ and for the other half $t'' < t'$. It follows then that by integrating from 0 to t'', equation 4.16 becomes

$$\langle r(t)^2 \rangle = 2 \int_0^t dt'' \int_0^{t''} d\tau \langle v(0) v(\tau) \rangle \tag{4.18}$$

which can be integrated without prior knowledge of the velocity autocorrelation function to yield the general result

$$\langle r(t)^2 \rangle = 2 \int_0^t d\tau (t - \tau) \langle v(0) v(\tau) \rangle \tag{4.19}$$

To extract a full expression for the mean square displacement we approximate the form of the velocity autocorrelation function. Particle diffusion is a Gaussian process for which the correlation of motion can be described by an exponential decay [145]

$$\langle v(0) \cdot v(\tau) \rangle = \langle v(0)^2 \rangle exp\left[\frac{-\tau}{t_{\mathrm{D}}}\right] \tag{4.20}$$

where t_{D} is the correlation timescale of Brownian diffusion.

This description has also been found to describe long-time activity enhanced diffusion [164], where the timescale becomes an active timescale t_{c}. We suppose the velocity autocorrelation function is a linear superposition of both the active and passive effects

$$\langle v(0) \cdot v(\tau) \rangle = \langle v(0)^2 \rangle exp\left[\frac{-\tau}{t_{\mathrm{c}}}\right] + A(\tau) \tag{4.21}$$

where $A(\tau)$ describes the Brownian contribution.

The timescale of the passive contribution is in general, and here, assumed to tend to zero, as it is several orders of magnitude faster than the imaging speed used ($> 10^3$) [73]. This means

$$\int_0^t d\tau A(\tau) = D_0 \tag{4.22}$$

Substitution of the velocity autocorrelation function, equation 4.21, into equation 4.19, produces

$$\begin{aligned} \langle \Delta r(t)^2 \rangle = 2t \int_0^t v^2 e^{-\tau/t_{\mathrm{c}}} \, d\tau \; + \; 2t \int_0^t A(\tau) \, d\tau \\ - \; 2 \int_0^t \tau v^2 e^{-\tau/t_{\mathrm{c}}} \, d\tau \; - \; 2 \int_0^t \tau A(\tau) \, d\tau \end{aligned} \tag{4.23}$$

which we integrate and reduce, then convert to a two-dimensional expression by multiplying by 2 to yield

$$\langle \Delta r^2(\tau) \rangle = 4D_0\tau + 4D_{\text{act}}[\tau - \tau_c(1 - exp^{-\tau/t_c})] \tag{4.24}$$

where D_0 remains as the passive diffusivity, D_{act} is the long-time or active diffusivity and τ_c is the correlation time, describing the timescale in which the diffusivity changes from D_0 to D_{act}. Note, this is the same form used by Koumakis *et al.* and Huang *et al.* [57, 66] for their fitting of activity-enhanced mean square displacements.

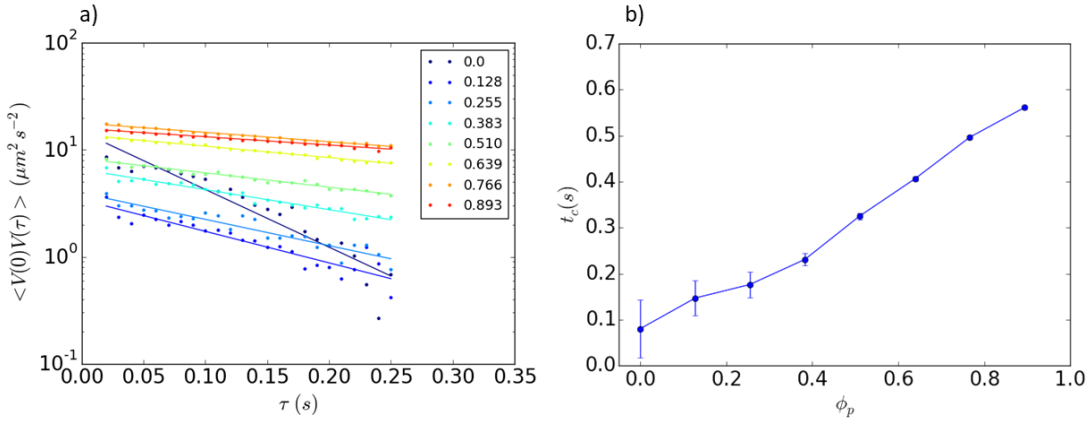

Figure 4.4 a) Velocity autocorrelation function for a series of attraction strengths, ϕ_p. These are fitted with equation 4.20 to extract the timescale, t_c, which is then plotted in b) as a function of ϕ_p

Direct fitting of equation 4.24 often yields noisy results due to poor fits of t_c. We opt to first measure t_c from the velocity autocorrelation function, equation 4.21, and later use those values for fitting the mean square displacement, equation 4.24.

The velocity autocorrelation functions are calculated from equation 4.18 for the range of polymer concentrations and plotted in figure 4.4a. The results fit the exponential decay assumed by equation 4.20, and the related correlation times are extracted and plotted in figure 4.4b. The correlation times are found to continuously increase with polymer concentration, indicating that stronger depletion attractions increase the persistence of the tracer's motion. As we will show later, this increased correlation occurs due to extend tracer-bacteria interactions.

The average mean square displacements are measured for tracer particles in an

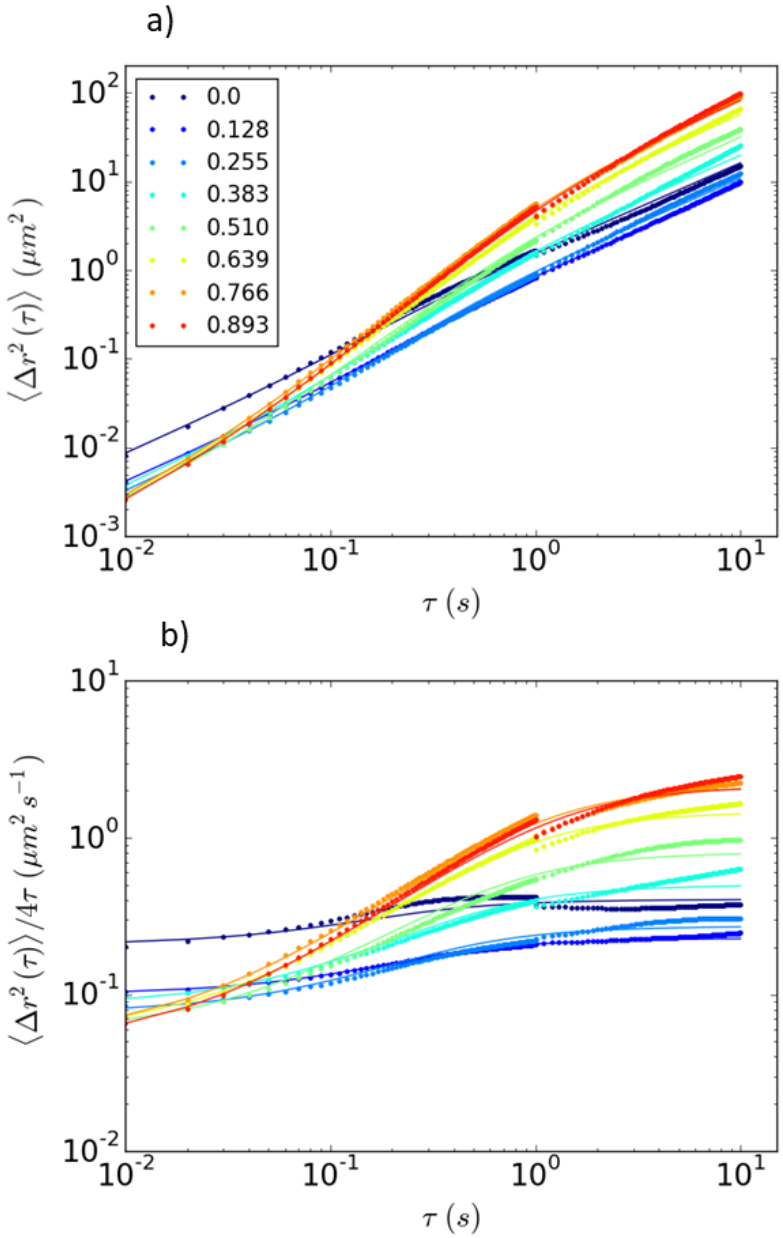

Figure 4.5 Mean square displacements of monomeric tracer particles in a bath of motile *E. coli* at fixed surface concentration $c_B = 5.7 \times 10^{-3}$ μm^{-2} for a range of polymer concentrations, ϕ_p. a) Mean square displacement. b) Mean square displacements are divided by 4τ to give the effective diffusion constant as a function of the timescale, τ. Both plots are fitted to equation 4.24, where the timescale, t_c, is not fitted but extracted from the velocity autocorrelation function below.

active bath of surface concentration, $c_B = 5.7 \times 10^{-3}$ μm^{-2} for the same range of attraction strengths as previously, plotted in figure 4.5a. The mean square

displacements are fitted with equation 4.24, where t_c was previously determined from the velocity autocorrelation functions. For short delay times, the tracers are diffusive, with effective diffusivities close to their previous measured passive diffusivities, D_0. While at intermediate delay times, $\langle \Delta r^2(\tau) \rangle$ shows super-diffusive behaviour, where it increases with τ^x, for $1 < x < 2$, the largest power observed here, $x \sim 1.8$ for the largest polymer concentration, $\phi_p = 0.893$. At long times, the tracers behave diffusively again, with an enhanced effective diffusion constant. This is the generic behaviour for activity enhanced diffusion and does not change with polymer concentration.

Again, we replot the datasets in the form $\langle \Delta r^2(\tau) \rangle / 4\tau$, shown in figure 4.5b, to give the effective diffusivity as a function of delay time. The effective diffusivity highlights that the addition of polymer decreases the short-time diffusivity and increases the long-time diffusivity. In the most extreme case, this is polymer-enhanced and activity-enhanced diffusivity results in a $\times 30$ increase in the long-time diffusivity. We will review how and why this occurs later in this section and in further detail within the next section.

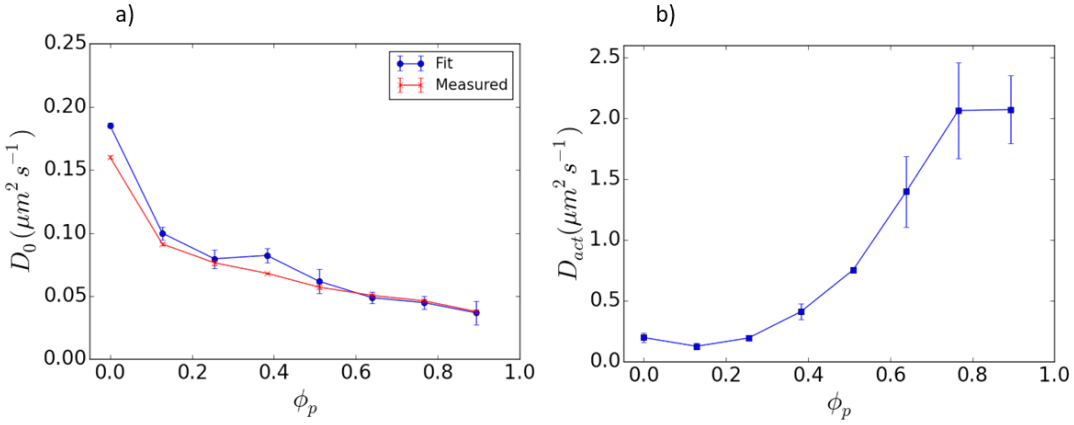

Figure 4.6 Experimentally measured diffusion constants from the fitting of the mean square displacements with equation 4.24. a) The passive diffusion constant, in red, is plotted against the short-time diffusion constant for samples in an active bath, in blue, as a function of polymer concentration, ϕ_p. Red data points were extracted from passive $\langle \Delta r(\tau)^2 \rangle$ fits, figure 4.2 and blue data points from active $\langle \Delta r(\tau)^2 \rangle$ fits, figure 4.5. b) The long-time diffusion constant for samples in an active bath.

The fitted values of D_0 and D_{act} from the mean square displacements of the activity enhanced samples are reported in figure 4.6. Figure 4.6a shows the results fitted values of D_0 from samples with bacteria in blue and from samples without

bacteria in red, from the previous section, which show excellent agreement. The long-time, activity enhanced diffusion constant, D_{act} is plotted in figure 4.6b and is found to increase with increasing attraction strength. Again, $\phi_p = 0$ is observed to have a higher diffusivity than expected based on the trends in D_0 and D_{act}. This deviation occurs because, without polymer depletants, the tracers are located slightly further away from the surface and thus experience less drag.

4.4 Enhanced Diffusion Mechanism

So far we have shown that active baths increase tracer particle's diffusivity and the addition of polymer depletants to the active bath yields a further increase to tracer particle's enhanced diffusion. Within this section, we will explore the mechanism by which this occurs.

There are two mechanisms by which enhanced diffusion could occur for this system, either sticky interactions between bacteria and tracer or long-ranged hydrodynamic interactions with a bacterium's flow field. We can determine if one of these mechanisms dominates by examination of the tracer trajectories due to overt differences in the actively enhanced displacements. Sticky interactions are expected to result in a continuous movement of the tracer in the direction of the bacterium, whereas long-hydrodynamic interactions result in incomplete loop-like trajectories. Note, the bacterial density is not high enough to induce collective motion within the bath [80], ruling out that mechanism and we also do not expect entrainment to be significant for this system as the tracers are too large [82].

Example tracer trajectories are depicted in figure 4.7 corresponding to samples with or without bacteria and samples with no polymer depletant or the highest polymer concentration tested. Samples without bacteria behave diffusively (a and b). Upon addition of the active bath samples with no polymer show enhanced displacements (c). In these samples, by eye, we do not observe any noticeable loop-like trajectories indicative of long-range hydrodynamic interactions with passing bacteria. For samples containing high concentrations of polymer depletant and an active bath, we observe highly persistent motion, indicating prolonged particle-bacteria sticky interactions, where the bacteria pushes or drags the particles.

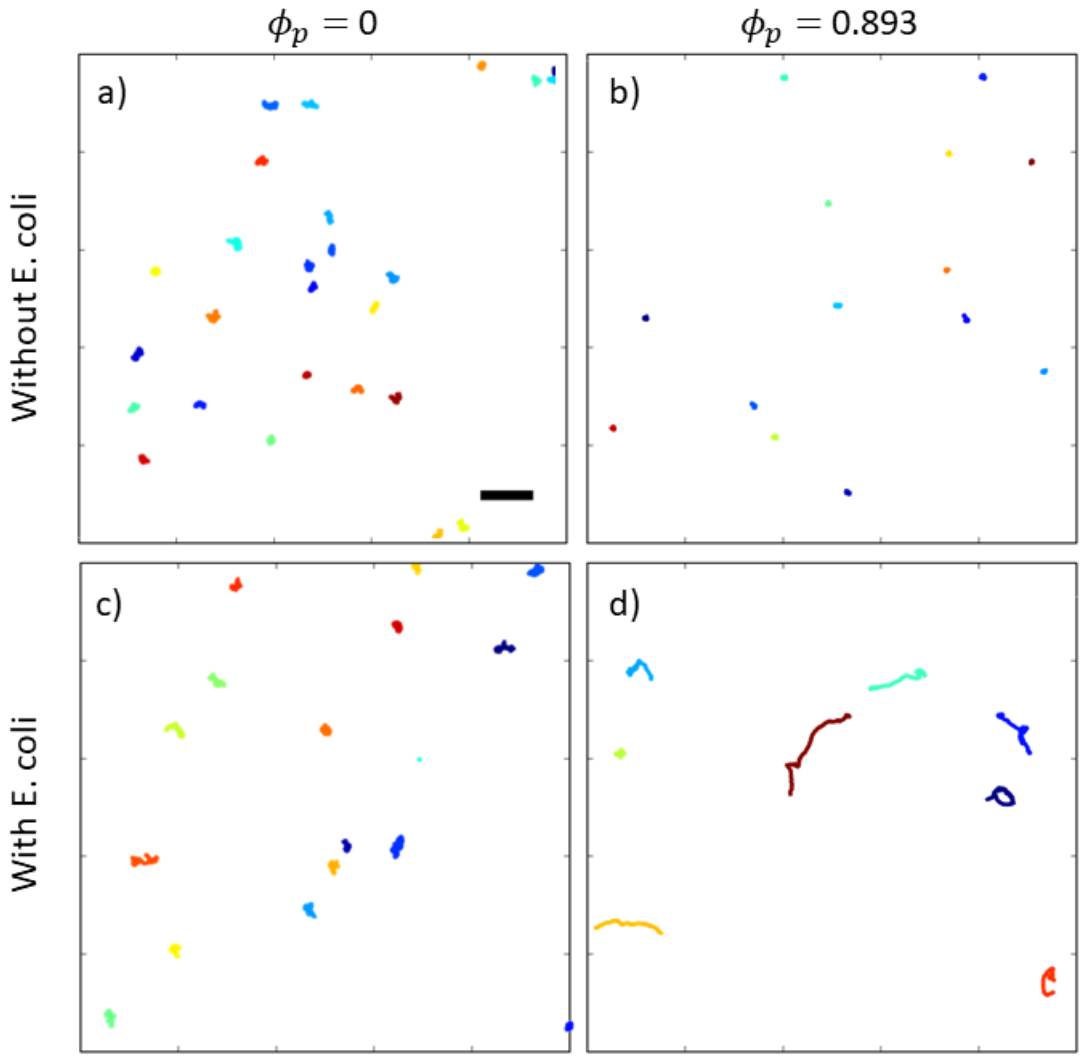

Figure 4.7 Representative trajectories of passive colloids over a 10 s period, covering the range of the variables investigated here. a) shows trajectories for the passive colloids in the buffer alone. b) trajectories for the passive colloid monomers in polymer depletant, where the polymer volume fraction, $\phi_p = 0.893$ and the viscosity, $\eta \approx 2.6$ mPa s. c) and d) show trajectories for samples with motile smooth swimming E. coli (surface concentration $= 5.7 \times 10^{-3}$ μm^{-2}, and mean speed v $= 12$ μm s^{-1}), without and with polymer depletant respectively. The scale bar represents 15 μm.

To further support the sticky interaction mechanism, we show a detailed sticky interaction between a bacterium and tracer. Figure 4.8, depicts a sequence of cropped bright-field micrographs, labelled with the tracer's trajectory from particle tracking. For the first 1.0 s of the sequence, the tracer does not interact with any bacteria and undergoes Brownian diffusion. A bacteria approaching from the left of the image makes contact with the tracer at 1.0 s. While interacting

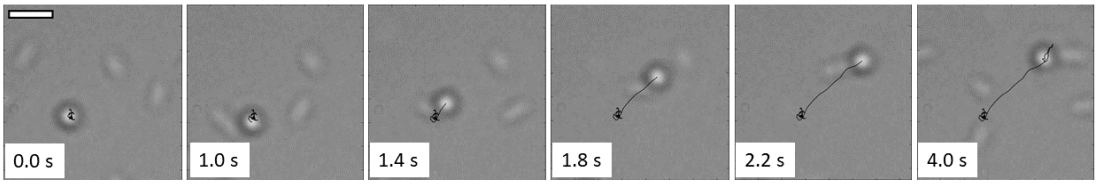

Figure 4.8 Sequence of bright-field micrographs depicting the interaction between a particle tracer and bacterium for $\phi_p = 0.639$. The images are overlaid with the tracked particle trajectory. A scale bar depicting 3 μm is located on the first image and the timestamps are indicated in the bottom left of each image. The bacteria approaches from the left and makes contact with the tracer at 1.0 s and then pushes the tracer until $\approx$ 2.2 s.

with the bacterium, the tracer moves with enhanced speed and in a persistent manner, in the same direction as the bacterium. After a short period of $\sim$ 1.2 s, the bacterium slides past the tracer, and then the tracer returns to diffusing in a Brownian manner. Note the flagella bundle often does not align with the cell bodies central axis, which here gives the appearance that the cell is sliding sideways.

4.5 Active Flux Normalisation

The degree of activity enhanced diffusion is well known to be dependant on the active particle's speed and density, where the activity enhanced component of the diffusion constant [88]

$$D_{\text{act}} = \beta J_A \tag{4.25}$$

where the active flux, $J_A = vc_B$ and v is the speed of the bacteria and c_B is bacterial surface concentration. The constant β is dependant on the bacteria-tracer interactions and changes based on system parameters, for example, chamber height [88] or tracer diameter [99].

The addition of polymers to solutions of bacteria can alter the active flux and therefore also D_{act} [81, 99]. To account for a changing active flux, we measure and normalise our values by the flux and therefore isolate the role of changing bacteria-tracer interactions on D_{act}.

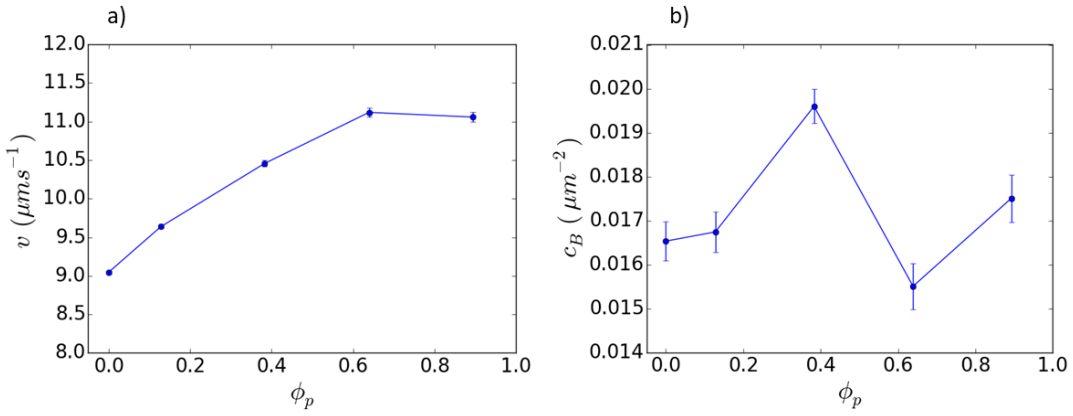

Figure 4.9 Measurements of how the active bath is influenced by the increasing presence of polymer, which is expressed in attraction strength, ϕ_p. a) Average speed, measured by DDM 100 μm above the sample surface. b) The average surface concentration of motile bacteria c_B, measured by tracking and counting the number of ballistic bacteria. These samples were prepared at an optical density, OD = 0.3, a bacterial concentration 3 times higher than the other samples within this chapter. This was changed as the higher density is the standard bacterial density for population studies.

The measurements of active flux are reported in figure 4.9. We find the speed of bacteria increases with polymer concentration, up to $\sim$ 20 % higher as measured by bulk DDM measurements, figure 4.9a. Also, we observe no change in surface density with increasing polymer concentration within experimental fluctuation, measured by tracking and filtering out non-swimmers, figure 4.9b. This results in an active flux which increases by $\sim$20% over the polymer concentration range tested, figure 4.10a, where the bacterial concentration was assumed to be a constant value across all measurements, $c_B = 0.017\ \mu\text{m}^{-2}$

To remove the effect of increasing active flux from D, we plot the $\beta = D_{\text{act}}/J_A$, where J_A is the active flux, plotted in figure 4.10b (note, in two-dimensions, β is expressed in units of μm^3). The values for J_A at $\phi_p = 0.255$, 0.510 and 0.766 were estimated by linear interpolation. These results show that changes in the active flux do not account for the increase in active diffusivity observed and that the addition of polymer depletants increases the effect of activity enhancement on a per bacteria-tracer interaction. Again, there is still a slight anomaly for $\phi_p = 0.0$ due to a decreased hydrodynamic drag on the tracers for those samples.

Mino *et al.* also measured β for 1 and 2 μm diameter tracers, also in baths of *E. coli* [87], where the tracers were, on average, located $\sim$ 1 μm from the surface

and obtained $\beta(3D) = 5\ \mu m^4$. To compare results, we can convert our values of β to $\beta(3D)$ if we estimate the image's depth of field and thus calculate the volume density of bacteria. The image's depth of field, DOF $= \pm\lambda\sqrt{n^2 - NA^2}/2NA^2$, where λ is the wavelength of light, n is the refractive index of the medium and NA is the numerical aperture of the objective, giving a DOF $\sim 1\ \mu$m. So for $\phi_p = 0.0$, this gives $\beta(3D) \sim 5\ \mu m^4$, matching that of Mino *et al.*.

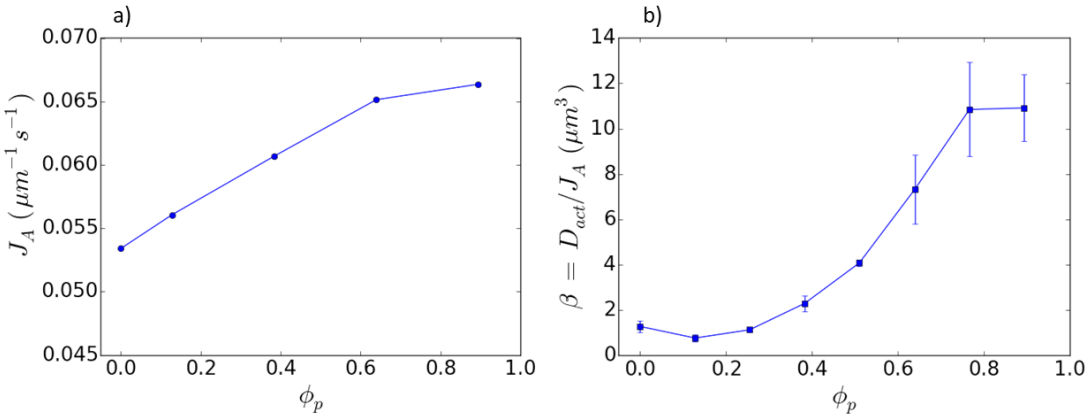

Figure 4.10 Accounting for a changing active flux, J_A. a) Active flux as a function of attraction strength ϕ_p, assuming a constant density, $c_B = 5.7 \times 10^{-3}\ \mu m^{-2}$. b) Values of the β coefficient, calculated by dividing measured activity enhancement of the diffusion constant, D_{act}, by the active flux. J_A.

4.6 Theory

For this two-dimensional system, the enhanced diffusion mechanism presented within this chapter is that tracers undergo Brownian motion interspersed with ballistic jumps due to sticky tracer-swimmer interactions. To further validate this model, in this chapter we will predict values for the enhanced diffusion constant, D_{act}, with an entrainment jump-diffusion model using data from additional experimental measurements.

Several models for enhanced diffusion have been developed over the last decade to describe a range of tracer-swimmer interactions. Instead of developing our own model, we take the framework for a jump-diffusion process which was initially used to describe enhanced diffusion of tracers by entrainment to fast and large swimming algae [58, 82], which is reproduced below.

The total diffusivity, D_{eff}, is described as a diffusive process from Brownian motion, D_0, and long-ranged hydrodynamic interactions with cells, D_{FF}, which is interspersed with ballistic jumps due to entrainment with motile cells, described by a diffusivity, D_{entr}. This two-dimensional continuum model is based on the idea that the tracer is either behaving diffusively or is undergoing an entrained jump. The tracers swap between these two states at separate and constant transition rates. In the limit that the switching rate from ballistic to diffusive motion is much larger than the reverse, which is true for low bacteria concentrations and therefore low frequency of tracer-bacterium interactions, the total diffusivity is described by

$$D_{\text{eff}} = D_0 + D_{\text{FF}} + D_{\text{entr}} \tag{4.26}$$

and the diffusivity due to entrainment events is

$$D_{\text{entr}} = \frac{\langle L \rangle^2}{2} \gamma v c_B \tag{4.27}$$

Where L is the length that a tracer is entrained from an interaction with a bacterium, v is the speed the tracer moves while entrained and c_B is the bacterial surface concentration. The final term, γ, can be considered a cross-sectional length, for which there is a probability that a tracer will be dragged by a swimmer if it is found within this length of the swimmer.

To model our system, we first ignore the hydrodynamic component, D_{FF} as previous publications suggest it is less significant for modelling enhanced diffusion in two dimensions [88, 90]. Secondly, we convert D_{entr} to D_{act}, by describing the cross-sectional length proportional as the length scale in which depletion forces act on a tracer as a swimmer undergoes a close approach.

To estimate D_{act}, the only new value we need to determine is the average length tracers are dragged per sticky interactions, L. For our results, it did not prove possible to extract L from direct analysis of the tracks, for example by determining prolonged correlated motion or changes to instantaneous speeds as described in the aforementioned algae experiments [58]. Instead, we calculate the instantaneous velocity of the tracers, v, over a timescale, $\tau \ll t_c$, allowing for the estimation of the dragged length as the tracer's velocity multiplied by it's correlation time, $L = vt_c$. The distributions of instantaneous velocities for

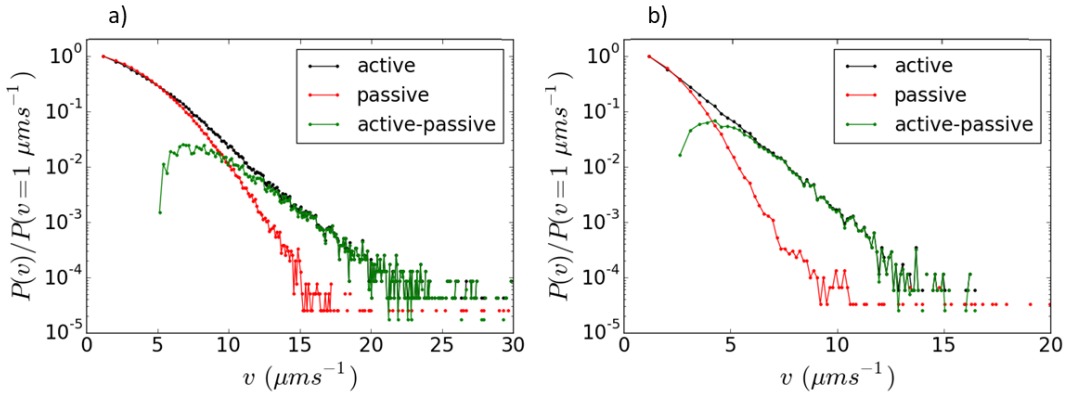

Figure 4.11 Distributions of instantaneous velocities, $P(v)$, over timescale, $\tau = 0.03\,\mathrm{s}$ for a) $\phi_p = 0.0$ and b) $\phi_p = 0.893$. Distributions for passive samples are plotted in red, active in black and active minus passive in green. Note the change in the x-axis scale between the figures.

samples where $\phi_p = 0.0$ and 0.893 are plotted in figure 4.11 a and b respectively. To estimate the displacements due to sticky tracer-swimmer interactions we again assume the tracers are either diffusing or are stuck to a swimmer, and therefore the diffusive velocities can be subtracted from the active velocity distributions. Note, the subtraction of passive from active velocities is a zeroth order approximation and accurate quantification of the instantaneous velocities would require thorough deconvolution of the data. The passive velocity distributions are plotted in red in figure 4.11, as measured from samples without bacteria, and the residual (active-passive) is plotted in green.

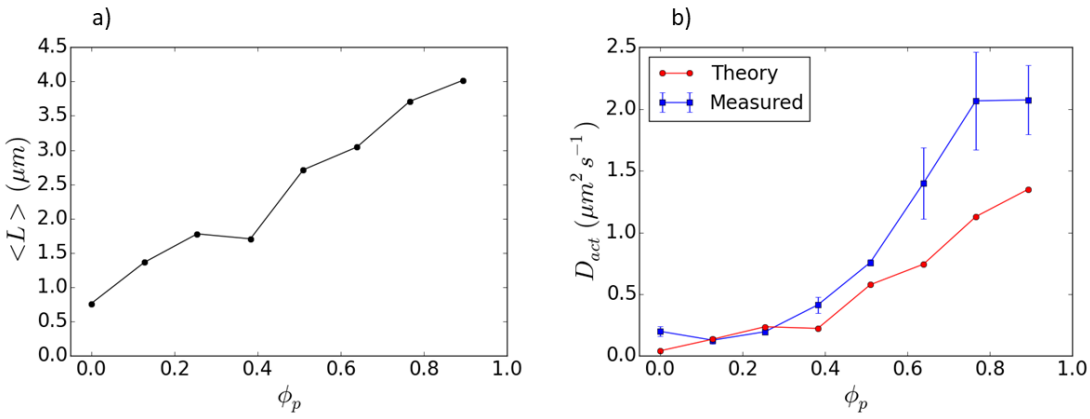

Figure 4.12 a) The dragged length, L as a function of attraction strength ϕ_p. b) Estimations of active diffusivities from equation 4.27, assuming $D_{\mathrm{act}} = D_{\mathrm{entr}}$, as a function of ϕ_p, plotted in red and measured values of D_{act} in blue, reprint from section 4.3.

The dragged length, L, is plotted as a function of attraction strength ϕ_p in figure 4.12a. For $\phi_p \leq 0.383$, L approximates the tracer's radius and might be better attributed to a bacterium pushing a tracer out of its path, rather than sticky tracer-swimmer interactions. For $\phi_p > 0.383$ we observe an increase in the dragged length, where stronger depletion forces allow the tracer to dragged further for each encounter with a bacterium. We previously presented a sequence of micrographs, figure 4.8, depicting the dragging of a tracer for ϕ_p=0.639 for ∼3.5 μm, very close to our average estimated value $L = 4.5$ μm

Finally, to estimate D_{act}, we need to define the constants in equation 4.27. We will assume the tracers move at the same speed as the free-swimming bacteria $v(\phi_p)$ = 9-11 μms^{-1}, the bacterial concentration, $c_B = 5.7 \times 10^{-3}\,\mu\text{m}^{-2}$ and we approximate the cross-sectional collision length scale, $\gamma = \sigma_{\text{bac}} + \sigma_{\text{tracer}} = 2.3$ μm.

The estimated values of D_{act} are plotted as a function of ϕ_p in figure 4.12b in red and measured values from fitting the mean square displacements are plotted in blue. We find good agreement between the measured values and the theoretical values obtained within this chapter. The theoretical values are generally lower than the measured ones, as expected, due to the omission of long-ranged hydrodynamic interactions increasing tracer diffusivity. This modelling shows that the enhancement of D_{act} with increasing depletion attractions is due to enhancement of sticky tracer-swimmer interactions. Note the scaling of our theoretical predictions are sensitive to the constants used, and therefore the quantitative result should be taken with reservations.

The application of this jump-diffusion model to our experiments validates our observations that, for high ϕ_p, sticky interactions are the main contribution to the diffusivity enhancement. The difference between theory and experiments at low ϕ_p may be due to long-ranged hydrodynamic interactions (D_{FF}), which were omitted from our calculations.

4.7 Conclusion

In this chapter, we developed a two-dimensional system of silica tracer particles in a bath of motile smooth swimming *E. coli*, which we use to study how the addition of polymer-induced depletion attractions modify the enhanced diffusivity effect.

We started by measuring the passive diffusivity of tracer particles. On initial sample preparation, the tracers quickly sediment to the bottom surface of the capillary where they undergo diffusion. To measure the tracer diffusivity, individual tracers were tracked and the mean square displacements calculated, from which we fitted a Brownian diffusion constant, D_0. Due to the proximity to a surface, the diffusivity is lower than the theoretical Brownian diffusivity. The ratio of the theoretical to measured diffusivities allowed for approximations of the, Z, between the particle surface and the capillary surface of ~ 30 nm. This distance is observed to be slightly higher for samples without polymer depletants, ~ 170 nm, which introduces some anomalous results where $\phi_p = 0$. The difference in Z between samples with and without polymer is due to the strong depletion attractions between a wall and sphere, which keeps the tracers close to the wall while still maintaining a finite gap, preserving the no-slip boundary.

Upon addition of motile bacteria, at short times the tracers maintain their passive diffusivity and at long times are observed to have an enhanced diffusivity, as observed in previous work [66]. We fit the mean square displacement with an additional Brownian diffusion term which is omitted in some studies of activity enhanced diffusion [99, 164], this simplification is possible when short-time behaviour is not examined.

For $\phi_p = 0.0$, the enhancement in diffusivity comes from a mixture of interactions between the tracer and a bacterium, where tracers are pushed out of the bacterium's path or alternatively the bacteria's hydrodynamic flow field pushing the tracer. As attraction strength is increased, for $\phi_p > 0.383$, the close approach of a bacterium allows for tracers to momentarily stick and be dragged for short distances, which increase with further increases to attraction strength. This then can be described as a jump-diffusion mechanism, where tracers swap between diffusion and ballistic jumps.

We verify the jump-diffusion model with theoretical predictions, adapted from theory for enhanced diffusion by entrainment processes [58]. To estimate values of the enhanced diffusion constant we measured a dragged length from the distribution of tracer displacement by linearly accounting for Brownian displacements. These theoretical estimates well approximate experimental results, and validate the jump-diffusion model.

We note that some of the enhanced diffusion effect, from added polymers, is due to a small increase in the active flux but this is insignificant compared to sticky

tracer-swimmer interaction effects.

Chapter 5

Activity Enhanced Diffusion in Three Dimensions

In this chapter, we re-examine tracer-swimmer interactions but for a three-dimensional system. We study how tracer-swimmer polymer induced depletion attractions effect diffusivity enhancement by using fluorescence DDM to probe tracer dynamics and phase-contrast to study bacteria dynamics. Due to unexpectedly large diffusivity enhancements by smooth swimmers, we also review the effect of tumbling for the system without polymer depletants.

5.1 Methods

5.1.1 Materials

Within this chapter, we change both the strain of E. coli and the buffer used to alter the tumbling rate. Unless otherwise stated we use our standard smooth swimmer, AB1157 ΔCheY in a phosphate buffer (6.2 mM K_2HPO_4, 3.8 mM KH_2PO_4, 0.1 mM EDTA at pH $\sim$ 7.5 with 0.3 wt% TWEEN20). We also use AB1157 wild-type (WT) which undergoes run-and-tumble motion in the same phosphate buffer (which has a low tumbling rate) or in the phosphate buffer with an additional 67 mM NaCl (high tumbling rate). The tracer used is a fluorescent 1.8 μm diameter polystyrene bead at a volume fraction, $\phi_c = 5 \times 10^{-5}$. The polymer depletant is still polystyrene sulphonate of radius of gyration, $r_g = 67$

nm.

The samples are prepared in the same 400 μm high, borosilicate capillaries but imaged 100 μm from the lower surface.

5.1.2 Cell Density Measurements

To prepare samples of targeted cell densities we use a UV-vis spectrophotometer which was calibrated by colony-forming unit (CFU) count experiments. A CFU is a single cell that when left on a surface with sufficient nutrients for growth, will multiply and form a colony that is visible by eye. The CFU density is measured by taking a stock of known optical density, OD, and preparing several dilutions (here the initial stock was diluted $10^7 - 10^9$ fold). Carefully measured volumes of each dilution are pipetted onto an individual LB agar plate and the droplet is spread over the surface by slowly rotating the plate at an angle. Plates were then left to grow overnight at 37 °C. The number of CFU can then be counted for the known initial inoculation volume. For the specific setup used in this work $\mathrm{OD}_{600} = 0.6 \cong 10.2 \pm 1.3 \times 10^8\,\mathrm{mL}^{-1}$. To calculate the motile cell density, the CFU density is then multiplied by the motile fraction as measured by DDM for that specific stock.

As outlined in section 2.4.5, DDM analysis returns the differential image correlation function,

$$\left\langle |F_D(q,\tau)|^2 \right\rangle = A(q)[1 - f(q,\tau)] + B(q) \tag{5.1}$$

where $A(q)$ depends on the optical setup and the particle's shape, density and arrangement, $B(q)$ also depends on the optical setup and describes camera noise and $f(q,\tau)$ is the intermediate scattering function.

For samples of bacteria in motility buffer, i.e. without polymer depletant or tracers, sample to sample relative densities can be calculated from $A(q)$ [61]

$$\frac{\rho_1}{\rho_0} = \left\langle \frac{A_1(q)}{A_0(q)} \right\rangle_q \tag{5.2}$$

Where the ratio of $A(q)$ is used to remove the strong q-dependence. The

utilisation of this *in situ* measurement suggests sample preparation error of cell density is $\sim 5\%$. Within this chapter, we use run-and-tumble (WT) and smooth swimming (ΔCheY) *E. coli* and observe that the ratio of cell densities in the bulk $c_{\mathrm{WT}}/c_{\Delta\mathrm{CheY}} \sim 1.1$. Note while these measurements would ideally be used to calibrate samples containing tracer particles, the strong scattering of the tracer swamps DDM results from phase-contrast movies, i.e. we cannot probe the bath properties if the sample contains tracer particles. These *in situ* density measurements should also not be used when polymer depletants are present because any aggregation will alter $A(q)$.

5.2 Fitting Differential Image Correlation Functions

We measure the diffusivity of passive tracer particles in the bulk using differential dynamic microscopy (DDM). To probe the dynamical properties of the passive tracers, separately from the active bath, we use fluorescent tracers and epifluorescent illumination. The samples were illuminated with 450-490 nm light from a GFP filter cube, where the fluorescence was previously observed to have minimal impact on the bacteria for low intensities and short exposures by Jepson *et al.* [59]. Movies were recorded for 40 s at 100 frames per second (512 $\times$ 512 pixels) using a Hamamatsu Orca 4.0 CMOS camera on a Nikon Ti-Eclipse inverted microscope with a 10$\times$/0.3 NA objective, focused 100 μm from the bottom of the capillary and imaged at four locations across each sample. To quantify the properties of the bacterial stock, separate phase-contrast movies are recorded and processed by DDM in the absence of the tracer particles.

The intermediate scattering function, $f(q,\tau)$, describes the system's dynamics, for diffusion

$$f(q,\tau) = e^{-Dq^2\tau} \tag{5.3}$$

for diffusivity, D. Jepson *et al.* observed that equation 5.3 still holds in the case of enhanced diffusion [59].

Figure 5.1 a and b shows the measured ISFs and corresponding diffusivities from the fitting of fluorescent tracers in a bath of smooth swimming *E. coli*. We find

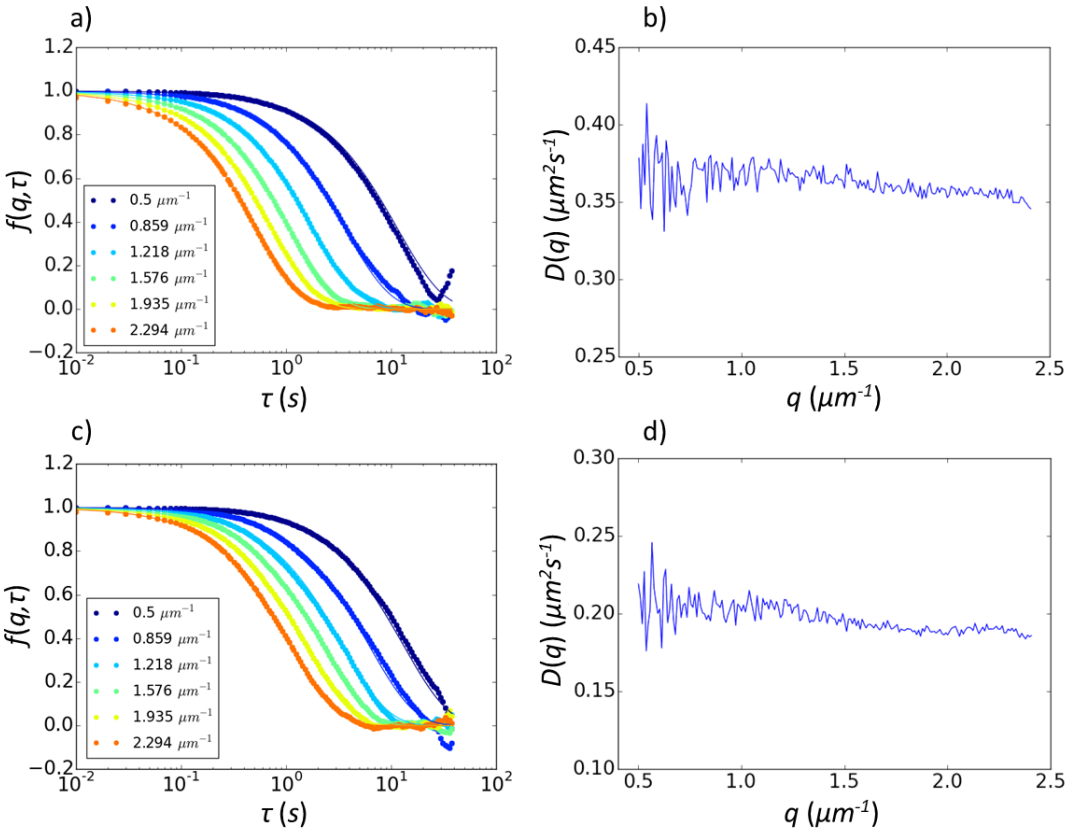

Figure 5.1 Fluorescence DDM results for passive 1.8 μm diameter polystyrene tracer particles in a bath of smooth swimming *E. coli*, $J_A \sim 13 \times 10^{-3}\,\mu\text{m}^{-2}\text{s}^{-1}$. a) and b) show results for a sample without polymer depletant ($\phi_p = 0.0$), c) and d) show results for a sample with polymer depletant ($\phi_p = 0.639$). a) and c) depict the intermediate scattering function, $f(q,\tau)$ obtained from DDM and corresponding fits to a diffusion model equation 5.3, b) and d) show the corresponding diffusion constant fits.

good fits for $0.5\,\mu\text{m}^{-1} < q < 2.4\,\mu\text{m}^{-1}$ for which the fitted diffusivities are broadly invariant in q (note, this q-range is the typical for this setup). We replicate these plots for samples with polymer depletants, $\phi_p = 0.639$, figure 5.1 c and d and show that the tracers still exhibit diffusive behaviour with the same small q-variance. The active bath is characterised by an active flux, $J_A \sim 13 \times 10^{-3}\ \mu\text{m}^{-2}\text{s}^{-1}$, kept approximately constant between samples and we will examine the effects of varying the flux more closely in the following sections

For enhanced diffusion, measurements of the mean square displacement have shown superdiffusive behaviour for timescales, $t_c < 1s$, for a range of distances from the surface [88, 90, 99, 164]. Brownian diffusion has also been observed even shorter times at the surface [66]. For our DDM results, superdiffusive

behaviour would correspond to D rapidly decreasing with increasing q. However, in agreement with previous measurements of enhanced diffusion by DDM, we find little indication of superdiffusive behaviour [59]. This difference in observations can be attributed to the large length scales probed by our DDM setup, $2\pi/q > 2.73\,\mu$m. These large length scales correspond to long time scales, for $D < 0.4\mu\text{m}^2/\text{s}$, $t = \pi^2/q^2D > 5$, i.e. the q-range measured is too low to observe superdiffusive behaviour.

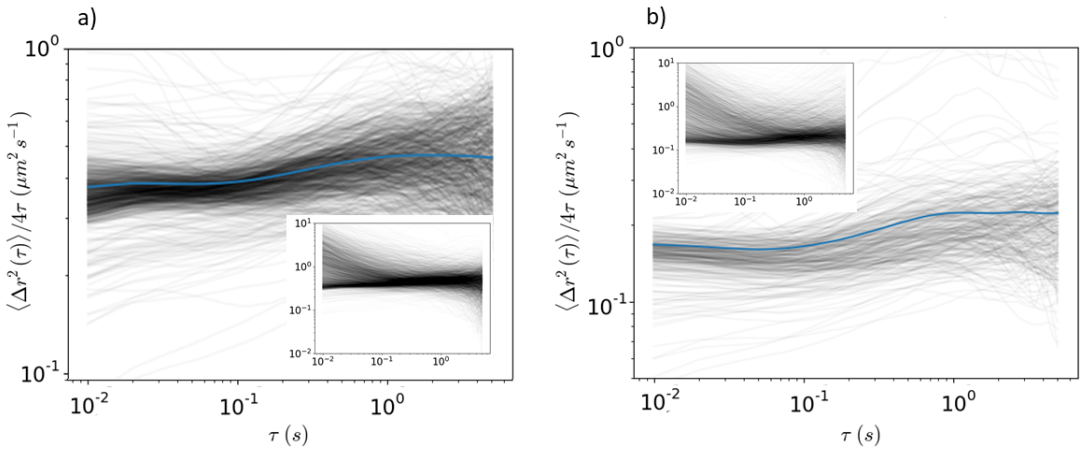

Figure 5.2 Two-dimensional mean square displacements of passive 1.8 μm diameter polystyrene tracer particles measured in the bulk of a bath of smooth swimming *E. coli*, $J_A \sim 13 \times 10^{-3}\,\mu\text{m}^{-2}\text{s}^{-1}$. a) $\phi_p = 0.0$ and b) $\phi_p = 0.639$. Figures show filtered data and insets show unfiltered (raw) data. The mean square displacement calculated for each individual trajectory is plotted with low transparency, where darker regions correspond to a higher density of trajectories. The average effective diffusivity is plotted in blue.

To extract rough estimates of the superdiffusive timescales present in these samples, we track the tracers in the same fluorescent movies and calculate their two-dimensional mean square displacement using the same methods as in chapter 4. The use of sub-pixel tracking with our low-resolution movies yields quantitatively inaccurate results due to pixel-biasing with a significant number of anomalous trajectories showing subdiffusive behaviour at short times. Fitting each trajectories mean square displacement to $D = \langle\Delta r^2(\tau)\rangle/4\tau$, we filter out poor trajectories by fitting each track to $D = a\tau^b$ and discard any trajectory if $b < -0.2$. We show the filtered data in figure 5.2 and the unfiltered data as insets.

The effective diffusivities are shown for $\phi_p = 0.0$ and 0.639 in figure 5.2a and b respectively, these measurements are from the same sample as in figure 5.1 but

here averaged over several areas. Both datasets show a lower diffusivity at short times and higher diffusivity at longer times with an intermediate superdiffusive regime. By eye, the crossover timescale $\tau_c \approx 0.2$-0.3, suggesting that DDM could measure D_0 in these samples for $q \sim 10\ \mu\text{m}^{-1}$. Such measurements are likely to require multiple optical setups to study the appropriate q ranges and may also require a re-evaluation of the ISF model to account for the intermediate superdiffusive regime.

5.3 Effect of Polymer Depletion on Enhanced Diffusion in the Bulk

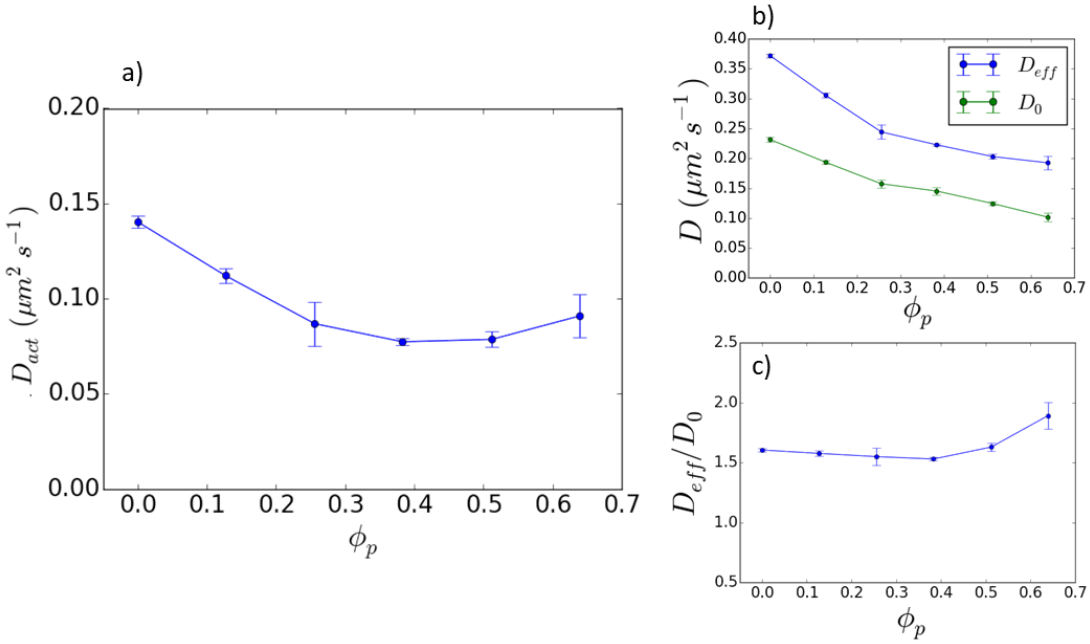

Figure 5.3 Fluorescence DDM measurements of the enhanced diffusivity, $D_{\text{act}} = D_{\text{eff}} - D_0$, as a function of attraction strength. The flux is kept approximately constant, $J_A \sim 13 \times 10^{-3}\,\mu\text{m}^{-2}\text{s}^{-1}$. a) D_{act}, b) measurements of D_{eff} and D_0, c) D_{eff}/D_0

The diffusion enhancement is measured as a function of polymer depletant concentration, where the enhancement is the measured diffusivity less the diffusivity for the same sample without any bacteria, $D_{\text{act}} = D_{\text{eff}} - D_0$. Figure 5.3a shows an initial decrease in D_{act} as polymer concentration increases, the raw data showing the contribution of Brownian motion is shown in figure 5.3b. Increasing ϕ_p, increases the viscosity, η, causing a decrease in D_0.

To rationalise the decrease in D_{act}, with increasing ϕ_p, we review how increasing viscosity changes the swimmer tracer interactions. Here the increasing viscosity decreases the rotational diffusivity of the swimmer, $D_{\mathrm{rot}} = k_B T/4\eta V_{bac}$ [157], where V_{bac} is the volume of a motile bacterium, which, in turn, increases the persistence length, $\lambda = v/D_{\mathrm{rot}}$. This increase in persistence length has been found in a decrease D_{act} in simulation studies [90, 110].

To compare our decrease in D_{act} with the previous simulations we estimate the initial change in λ for $\phi_p = 0.0 \rightarrow 0.256$ which corresponds to $\eta \approx 0.94 \rightarrow 1.44\mathrm{mPa\,s}$. To estimate the rotational diffusivity of a motile cell, it is commonly modelled as a prolate spheroid of length, $2a = 10\,\mu\mathrm{m}$ (body + flagella) and radius, $b = 0.5\,\mu\mathrm{m}$, for $V_{\mathrm{bac}} = 4\pi ab^2/3$, which for $v = 12\,\mu\mathrm{ms}^{-1}$, $\lambda = v/D_{\mathrm{rot}} = 58 \rightarrow 90\,\mu\mathrm{m}$. Over this range both simulation works predict D_{act} to decrease by $\sim 15\%$ [90, 110] compared to our decrease of $\sim 40\%$.

For $\phi_p > 0.256$ we observe a deviation in behaviour as D_{act} plateaus. The ratio D_{eff}/D_0 shows this deviation from the viscous dependant decrease more clearly, figure 5.3c. An increase in D_{eff}/D_0 for high ϕ_p hints that diffusion enhancement from sticky tracer-bacterium interactions is present in three-dimensions as well, as will be shown later in the text, and further that indicates the existence of a minimum in D_{act} around ϕ_p=0.45.

We are uncertain of how the active flux varies between samples in figure 5.3, as we are unable to measure the speed and density of swimmers *in situ* due to the presence of tracer particles. The diffusivity enhancement, D_{act} is known to be proportional to the active flux [59, 87, 90].

$$D_{\mathrm{act}} = D_{\mathrm{eff}} - D_0 = \beta J_A \tag{5.4}$$

Where the active flux, $J_A = c_B v$ and the constant β is a length scale to the fourth power which describes the tracer-swimmer interactions [59, 87, 90].

For a more accurate measure of diffusivity enhancement, we measure β for several values of ϕ_p. For each dataset, we measure J_A for samples without tracers but with the corresponding polymer concentrations. For $\phi_p = 0.0$, 0.320 and 0.639 we found the linear scaling of D_{act} with J_A remains and measured values of $\beta = 9.7 \pm 1.0$, 6.9 ± 0.7 and $7.86 \pm 0.8\ \mu\mathrm{m}^4$, shown in figure 5.4. These agree with the previous finding that the addition of polymer, at least initially, reduces diffusivity enhancement.

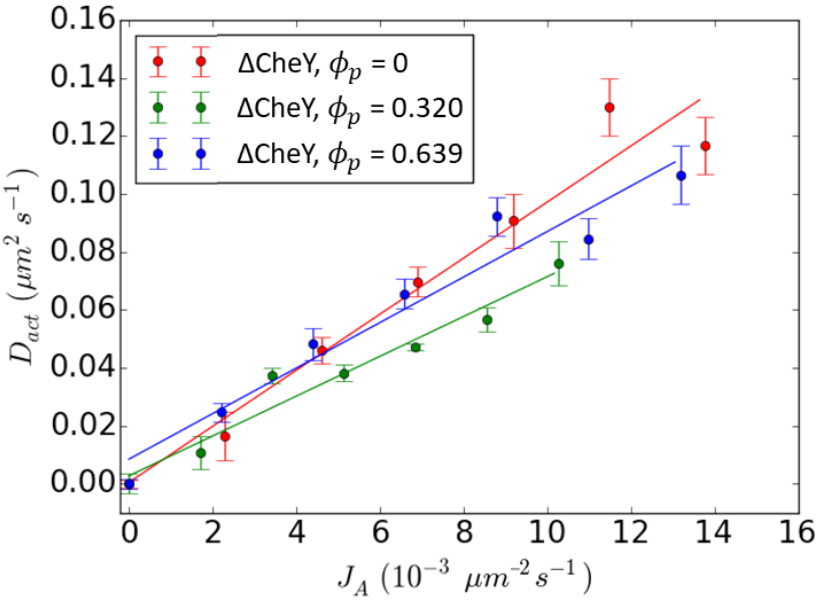

Figure 5.4 Diffusivity enhancement of passive tracer particles, D_{act}, in a bath of smooth swimming *E. coli* of active flux, J_A. Three polymer concentrations are tested, $\phi_p = 0.0$, 0.320 and 0.639 corresponding to $\beta = 9.7 \pm 1.0$, 6.9 ± 0.7 and 7.86 ± 0.8 μm^4

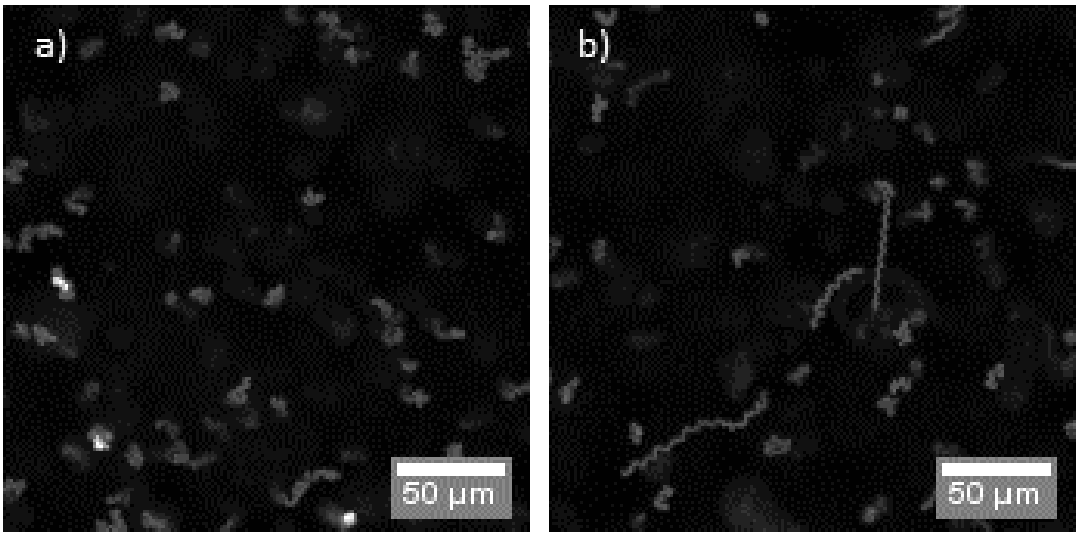

Figure 5.5 'Cheap tracks' of fluorescent tracer particles over 40 s for a) samples without polymer induced attractions, $\phi_p = 0.0$, and b) samples with polymer induced attractions $\phi_p = 0.639$

To examine if sticky tracer-swimmer interactions are present for this three-dimensional system and thus make contributions to β for large ϕ_p, we report representative trajectories of fluorescent tracer particles. To show tracer

trajectories, we generate 'cheap tracks' using the z-project feature in ImageJ, which is used to convert a movie into an image where each pixel corresponds to the maximum value observed for that pixel over the movie length. These cheap tracks give simplistic trajectories of the tracers, showing how the tracers move, the resolution here is too low to show loop-like displacements but can show persistent ballistic motion due to sticky tracer-swimmer interactions.

Cheap tracks are shown in figure 5.5a and b for fluorescence movies of tracers in a bath of smooth swimmers for $\phi_p = 0.0$ and 0.639 respectively. Both images are produced from z-projections of 40 s movies recorded with a $10\times/0.3$ N.A. objective with a depth of field ≈ 50 μm, where the brightness of each trajectory indicates the tracer's proximity to the focal plane. For $\phi_p = 0.0$, the tracers appear diffusive, however, for $\phi_p = 0.639$, tracers are observed moving ballistically for up to ~ 100 μm, where sinusoidal motion is induced due to the processive motion of the bacteria. Note, for the bacterial concentrations used within this chapter ($c_B < 10^{-3}\,\mu\text{m}^{-3}$), these sticky interactions are rare.

5.4 Effect of Tumbling Rates on β

In the previous section, we reported values of β for tracers in a bath of smooth swimming *E. coli*. Work by Jepson *et al.* on the enhanced diffusion on non-motile *E. coli* by a bath of wild-type *E. coli* (WT) report $\beta = 7.1$ μm^4 compared to our value of 9.7 μm^4 for samples without polymer. One of the key difference between these two experiments is the strain of *E. coli* used for the active bath, our bacteria are smooth swimmers compared to their run-and-tumblers. It is surprising then that we obtain larger values of β, as kinetic theoretical results suggest the inverse to be true [90, 110]. Also, we note that our tracer particles are spherical and slightly larger than their fluorescent non-motile *E. coli* tracers. It is an open issue of how tracer size effects enhanced diffusion [99], but a correction factor may be required for the change in tracer size and shape [90]. In this section, we will investigate this conflicting finding in detail. Note, Jepson *et al.* claim this dependence of D_A on λ to be accurate but to date, no experimental verification has been published. In this section, we shall take the opportunity to examine this experimentally.

To study the effect of persistence length we initially aimed to compare smooth swimmers (AB1157 ΔCheY) whose persistence length is controlled by rotational

diffusion with run-and-tumblers (AB1157 WT) whose persistence length is controlled by tumbling rate. Upon initial investigation, we discovered (or perhaps more appropriately re-discovered, see appendix A) that the tumbling rate of WT cells could be increased by the addition of NaCl. For the typical salt concentrations used in literature, [NaCl] = 67 mM, for WT cells we observe, by eye, the expected tumbling rate of $f_T \sim 1$ s^{-1} [12, 123]. However, throughout this thesis, we use [NaCl] = 0 mM, for which we observe, by eye, a decrease in tumbling, $f_T \sim 0.1$ s^{-1}. And, of course, for smooth swimmers, $f_T \sim 0$ s^{-1}.

Without specialised equipment for tracking cells in three-dimensions, it is difficult to extract exact tumbling rates for these bacteria in each condition, however, the trend can be inferred from the q dependence of v obtained from DDM [79, 131]. Theoretically, a swimmer with an infinitely straight trajectory has a speed which does not vary with length scale, $2\pi/q$. When swimmers deviate from a straight path they begin to swim further to travel the same length scale, so as reorientation rate increase, low-q speed decreases. This q-dependence is further affected by the experimental finite depth-of-field, where swimmers are seen disappearing into the plane of the movie, resulting in speeds that increase for lower q [79].

We report a qualitative measure of tumbling rates, R, which has previously been used to measure tumbling rates [131].

$$R = v(q_1)/v(q_2) \tag{5.5}$$

Where here we use $q_1 = 2.24$ μm^{-1} and $q_2 = 0.5$ μm^{-1}.

The swimming speed, v, as a function of q and corresponding values of R are reported in figure 5.6a and b respectively for the three separate baths. The R values qualitative match to direct observations where AB1157 ΔCheY has the lowest tumbling rate, AB1157 WT in buffer without sodium chloride has a small but finite tumbling rate and AB1157 WT in buffer with 67 mM sodium chloride has the highest tumbling rate.

Utilising these three separate active bath conditions, we re-evaluate the constant β for zero polymer conditions. Figure 5.7 shows diffusivity enhancement with the active flux and fits to equation 5.4. The fitting gives $\beta = 9.7 \pm 1.0$, 8.3 ± 0.5 and 9.0 ± 0.2 μm^4 for ΔChey, WT with 0 mM NaCl and WT with 67 mM NaCl respectively. Despite kinetic theory predictions to the contrary [90, 110], these results do not show a significant change in β with tumbling rate. These findings

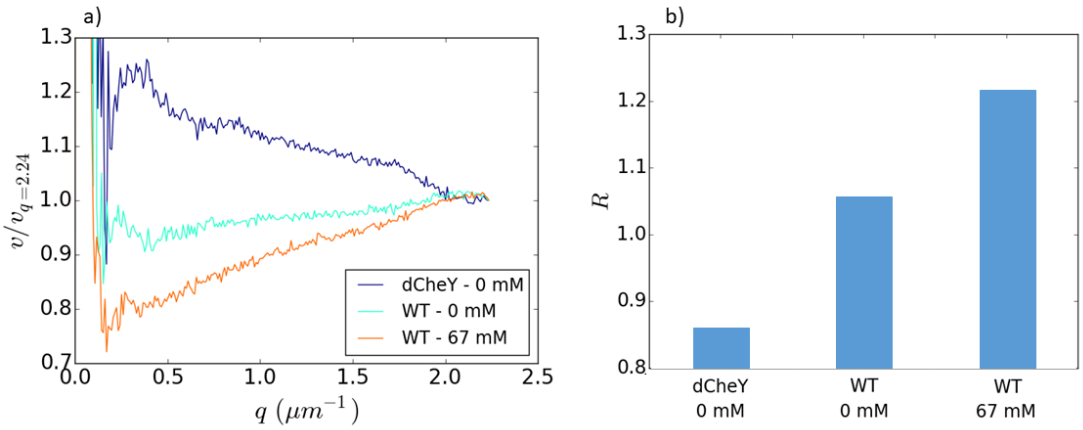

Figure 5.6 a) Fitted values for the swimming speed as a function of q from DDM, normalised by the swimming speed at high q. b) A measure of path straightness R, equation 5.5, where larger values indicate an increase in tumbling.

corroborate the large β values measured throughout this chapter.

Our measurements tracer diffusivity 100 μm from the capillary surface in a bath of WT with 67 mM NaCl is the same bath used by Jepson *et al.*. Despite small differences between our experiments (tracer shape, our higher frame rates and longer movies), there is no significant difference between our measured values of $\beta = 9.0 \pm 0.2\ \mu\text{m}^4$ and that of Jepson *et al.*, $\beta = 7.1 \pm 0.4\ \mu\text{m}^4$ [59].

5.5 Conclusion

In this chapter, we measured tracer diffusivity in the bulk of an active bath using differential dynamic microscopy. For the study of enhanced diffusion, current DDM setups are unable to probe a wide enough range of timescales to measure both short and long time diffusivities. We measure a single long time diffusivity for activity enhanced tracers and use separate samples without bacteria to measure the passive diffusivity for calculation of the diffusivity enhancement.

In a bath of smooth swimming bacteria, we observed the net effect of adding polymer depletants was to decrease the tracer's diffusivity enhancement in opposition to initial expectations. The small changes in viscosity used here do not significantly alter the speed or flow field of the bacterium and the changes to the tracer particles are accounted for. A possible explanation is that

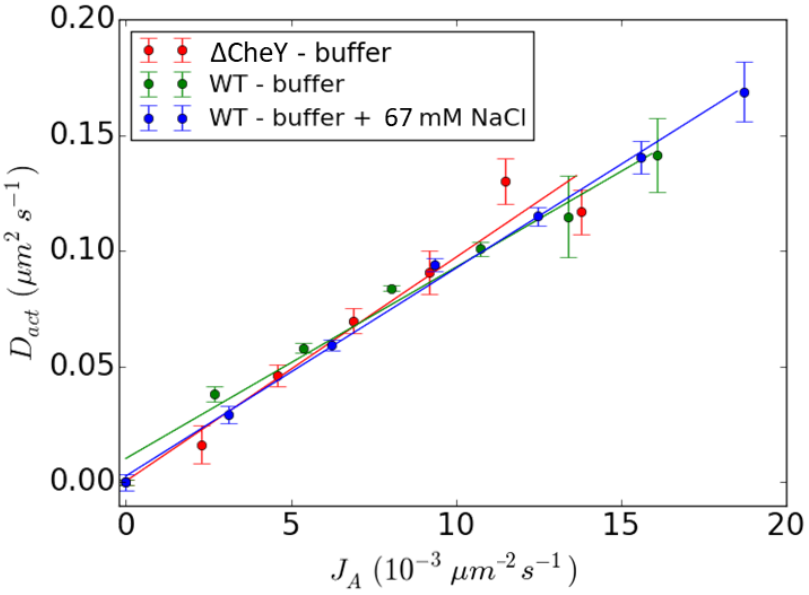

Figure 5.7 Diffusivity enhancement of passive tracer particles, D_{act}, in a bath of motile *E. coli* of active flux, J_A. Each dataset corresponds to a different tumbling rate $f_T \sim 0$, 0.1 and 1 s^{-1} for ΔChey, WT and WT + 67 mM NaCl respectively, corresponding to $\beta = 9.7 \pm 1.0$, 8.3 ± 0.5 and 9.0 ± 0.2 μm^4.

viscosity decreases the rotational diffusivity of the swimmers, straightening their trajectories, which is expected to reduce the net-displacement from a swimmer-tracer scattering event as tracers motion approaches a closed loop [90, 108, 110].

For our quasi-two-dimensional system (discussed in chapter 4), polymer depletion increases diffusivity enhancement. This enhancement in two-dimensions occurs due to sticky tracer-swimmer interactions where the tracer is dragged by the swimmer for a short period. These sticky interactions are observed in our three-dimensional system at high polymer concentrations but appear sporadically. This finding suggests that steric interactions are very infrequent in three-dimensions as compared to two-dimensions for similar bacterial concentrations and diffusivity enhancements. This difference is likely influenced by our use of *E. coli* which are pushers, their flow field pushes local tracers away, minimising the chance of both experiencing a short-ranged depletion attraction. It appears that sticky interactions only make a small contribution to diffusivity enhancement relative to far-field hydrodynamics. For baths of pullers, where near-field effects dominate diffusion enhancement [58, 82], sticky tracer-swimmer interactions may result in significant increases to diffusivity enhancements.

We measured $\beta = 9.0 \pm 0.2$ μm^4 for WT in motility buffer with 67 mM NaCl, similar to a value reported by Jepson *et al.* in the same mixture, $\beta = 7.1 \pm 0.4$ μm^4 [59]. Both of these measurements are similar to theoretical predictions for enhanced diffusion due to reorientations of the swimmers 7.24 μm^4 [90] and separate predictions for a combination enhanced diffusion due to reorientations and entrainment 9 μm^4 [108]. These theoretical predictions find that β can vary 1-2 μm^4 based on small changes in system parameters [90], accounting for the variation in measurements between us and Jepson et al.

Our findings, that diffusivity enhancement does not change with the tumbling rate but does decrease with increasing persistence length, appear to conflict. A possible explanation is the 'dead in the water' time that is introduced when a bacterium tumbles, since in this time no new tracer-swimmer interactions can occur. This time spent not swimming is zero for smooth swimmers and may reach $\sim$20% of the total time for the highest tumbling rates used here. Accounting for dead in the water time suggests that tracer-swimmer scattering events are more efficient for shorter persistence lengths, but for the case of tumbling, fewer tracer-swimmer interactions occur, indicating that it is coincidental that no change in diffusivity enhancement is observed when tumbling is introduced.

This dead in the water time is not accounted for in the above-mentioned simulation works and may account for the differences of our findings. It is clear that more work, both experimentally and theoretically, is required on this subject to explain the differences in observations.

Chapter 6

Introduction to Activity-Controlled Phase Behaviour

6.1 Studying Microscopic Behaviour

One of the reasons the study of colloids has been so fruitful is due to the abundance of information obtained from confocal scanning laser microscopy used to study bulk behaviour in three-dimensional studies. Confocal microscopy utilises a pinhole to exclude out of focus light and can thus excite and detect a single focussed region of a sample. The microscope then scans a three-dimensional region to build up a picture of the sample from a series of smaller volumes or voxels [91]. These samples can be $> 50\%$ particles by volume if the refractive index of the solvent and particle are matched [147].

However, the study of active matter with confocal microscopy is significantly more difficult due to the additional requirements introduced by activity. An ideal sample would be required to have matched refractive index and density between the active particle with the media, without disrupting the fuel supply. The development of such a sample has proved difficult, and thus work on dense active matter experiments has been mostly limited to two-dimensional studies [49]. While it is possible to prepare and study 3D dense and active samples, their study becomes difficult due to the aforementioned optical limitations and imaging speeds [136]. So our study of passive-active mixtures with attractions at high passive particle concentrations will be limited to two-dimensions, where the

entire sample can be observed and imaged.

6.2 Passive Colloidal Phase Behaviour

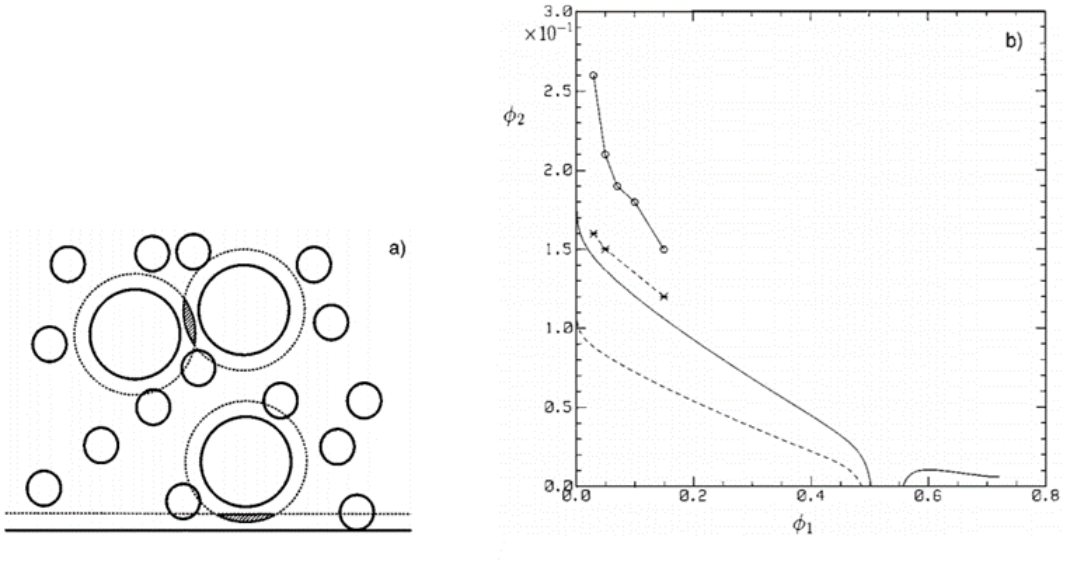

Figure 6.1 Taken from [34]. a) Schematic representation of the binary hard-sphere system. Particles are represented as circles with solid borders and depletion layers as dotted borders, and the wall of the container is depicted as a solid black line at the bottom, also with a depletion layer. In this system, the small particles act as depletants and induce attractions between the larger particles and large particles and the wall. b) The phase diagram of a binary hard-sphere mixture, where 1 denotes the large particle species and 2 denotes the smaller, where the particle size ratio, $\xi = 0.15$. The dashed lines describe phase separation at the wall and the continuous lines describe phase separation in the bulk, and the data points detail experimental observations and the rest is theoretical predictions.

For all of the extensive work on colloid-polymer mixtures in three-dimensions, it is surprising that our proposed system of spherical particles interacting on a two-dimensional plane has received less attention. One reason is that such a system is unintuitive because such particles are interacting in two-dimensions with three-dimensional interaction potentials and hydrodynamics whilst simultaneously experiencing wall effects like adhesion to solid walls [155] and particle drift [29]. Secondarily, when these systems initially started to receive attention, applications focused on three-dimensional systems and it was possible to acquire results for such experimental systems with the use of light scattering [106, 149] and confocal

microscopy [16, 55, 147].

To the writer's best knowledge, the closest work to colloid-polymer mixtures in 2D is the study of phase separation at the walls of 3D samples, where both colloid and polymer are in exchange within the bulk [34]. Such 3D samples have interesting interactions with walls due to the nature of the depletion induced attractions.

In mixtures of small and large particles, the small particles exert an osmotic pressure on the larger ones. When two large particles are close enough to exclude the smaller particles from the interparticle region, the osmotic pressure becomes anisotropic, resulting in an effective attraction between the large particles called a depletion attraction [6, 7, 158]. This is discussed in detail was section 1.4.3. These depletion attractions also occur between the large particles and the container walls, where the excluded volume and thus the depth of the depletion potential between a particle touching a wall is approximately twice as deep as that of two touching particles [62], depicted in figure 6.1a. This attraction to a wall results in an enhanced particle density at the wall, where the particles are still free to diffuse and experience depletions attractions to other particles at the wall or in the bulk. This pinning to a 2D plane and the further increase in density aids in the nucleation of crystals at lower depletant concentrations than in the bulk [18, 33, 65], where phase separation does still occur at higher depletant concentrations.

The observation of phase separation at the wall of the sample, before the bulk, is also observed for binary hard-sphere mixtures, if the size ratio of the spheres, $\xi = r_{small}/r_{large} \leq 0.15$ [34, 62, 103]. Here the small spheres act as depletants due to exclusion of their centres from the volumes around the larger particles and walls, depicted in figure 6.1a. The phase diagram of such mixtures is shown in 6.1b, reproduced from [34], where ϕ_1 is the larger particles volume fraction and ϕ_2 is the smaller particles volume fraction. The experimentally observed phase boundary at the wall is plotted with a dashed line and crosses and the subsequent bulk transition is marked with a solid line and circles.

6.3 Phase Behaviour of Purely Active Systems

The behaviour of passive systems is controlled by thermal forces from incessant collisions between solvent molecules and suspended particles. Active systems,

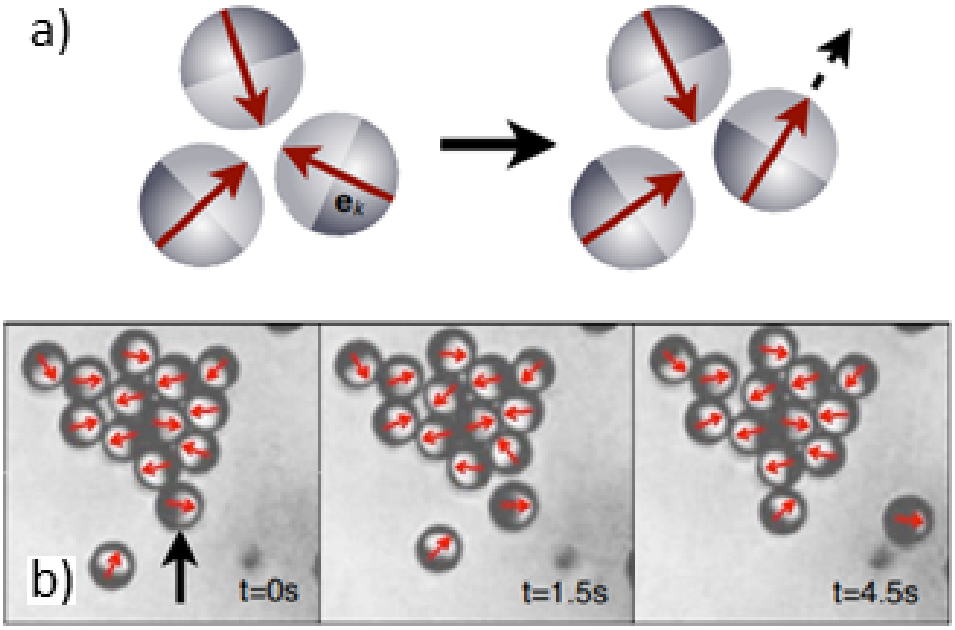

Figure 6.2 Taken from [24]. a) A sketch detailing the self-trapping mechanism. To nucleate a stable cluster, a minimum of three active particles are required to swim into each other. As the particles undergo rotation diffusion, they can form an unstable structure where a particle points outwards, freeing it from the cluster. b) Time-lapsed micrographs of a Janus particle cluster, with propulsion orientations of each particle marked by a red arrow. The cluster is held together by particles on the edge, which mostly face inwards. As an edge particle rotates to point away from the cluster, we observe it swim out of the cluster.

however, consume energy from their environment in the form of a fuel and undertake non-equilibrium activities, introducing additional forces which can dramatically alter the system's behaviour. Novel active behaviours that have received significant attention range from collective motion [30] to active nematics [36] and of particular interest to our work is their propensity to cluster and phase separate. Active or 'living' clusters not only show enhanced translational and rotational motion over their passive counterparts [64, 86, 122], and are also constantly breaking apart and reforming [47].

The simplest mechanism by which activity induces phase separation is particle self-trapping. When two active particles collide head-on they slide past each other due to their persistent motion, however when three particles collide and are all pointing inwards they are unable to slide past each other due to their excluded volumes and the active propulsion holds them together in a triplet, as

shown in figure 6.2a. For 3D systems, four active particles would be required to form a tetrahedron to initiate clustering. Additional particles can join the cluster by swimming in to it. All the particles within the cluster undergo rotational diffusion, and when particles on the cluster's perimeter point outwards, they break away from the cluster, as seen in figure 6.2b. As clusters grow, only the perimeter particles need to pointing inwards, the central particles are then randomly orientated, which results in an imbalanced directional force and torque on the cluster induces enhanced translation and rotation [47]. The aggregation and fragmentation of active clusters result in a finite mean cluster size cluster or steady state, which increases with particle speed and particle area fraction [24, 140]. This behaviour was predicted theoretically [137], then observed in simulations [43] and experiments [24].

Some experimental systems suffer from phoretic attractions, induced by their propulsion mechanism, an effect most well explored in Janus particle clustering [74, 75]. An example of a Janus particle is a polystyrene colloidal particle which is half coated in platinum. When submerged in aqueous solutions containing H_2O_2, the platinum face locally catalyses the decomposition to H_2O and O_2. In the decomposition of hydrogen peroxide, the reduction and oxidation reaction occur at different rates across the surface of the particle, producing an ionic current. The current generates an electric field which acts on ions in the Debye layer that propels the particle [20, 21]. The phoresis induced chemical gradients can interact with neighbouring particles and induce particle-particle attractions, where the strength of the attraction scales with activity [47]. Sufficiently strong attractions can dominate the clustering behaviour over self-trapping, allowing the perimeter particles to have random orientations, increasing active clusters translational and diffusional motion [47].

Striking examples of activity-induced attractions occur in populations of the fast swimming bacteria species *S. marcescens* and *Thiovulum majus* [27, 100]. As these species approach a surface, they can become dynamically bound with their flagella preferentially pointing normal to the surface due to hydrodynamic interactions. The hydrodynamic forces also induce long-ranged attractions on other cells at the surface, resulting in clustering of cells at the surface.

More common methods for bacterial aggregation occur via motility induced phase separation, where the bacteria slow down as local density increases. Such density dependence may be a result of increased collision frequency or quorum sensing, the ability of a bacterial species to communicate by secretion of signalling

molecules, which can slow bacteria down via biological pathways [45]. Density dependant speed initiates a positive feedback loop where bacteria slow down due to accumulation and then further accumulate due to slowing down. At some critical bacterial density, the speed of bacteria will be suppressed enough to phase separate [25].

The phase diagram of active systems becomes richer when attractions are decoupled from activity, for example in the case of motile *E. coli* interacting via polymer-induced depletion interactions [121, 122, 124]. Without polymer depletants, both motile and non-motile *E. coli* behave as a homogeneous fluid. As polymer depletants are added, bacteria-bacteria attraction strength increases, it is observed that non-motile populations undergo phase separation before motile ones. This occurs because the active forces oppose the attractive forces, reducing the effective depth and range of the interaction potential, and thus to overcome this effect, motile populations require stronger attractions to induce phase separation. At attraction strengths just shy of inducing phase separation, motile *E. coli* are observed to form clusters with unidirectional rotation, where their rotational speed is proportional to the inverse cluster radius. These clusters form from proto-clusters of non-motile cells, which are then later activated by motile cells adhering to their surface and inducing unidirectional rotation.

Phase separation of active particles with attractions has been studied thoroughly by simulations in the Péclet number, Pe and attraction strength U plane [112], reproduced in figure 6.3. Here, $\mathrm{Pe} = v\sigma/D$, where v is the particle velocity, σ is its diameter and D is its Brownian diffusion constant. For low Pe and high attraction strengths, gel-like phase separation is observed, shown in green, where the active forces are not sufficient to break the structure but still increase the rate at which it coarsens. As Pe increases, the gel structure is destroyed resulting in a fluid phase, shown in red, which requires higher swimming speeds to overcome stronger attractions. In the high Pe limit, the system undergoes phase separation again, triggered by self-trapping acting cooperatively with attractions, shown in blue. This reentrant behaviour, where the system goes from phase-separated to a homogeneous fluid and back to phase-separated as swimming speed increases, highlights the range of control afforded to active systems.

The competition between gel-like phase separation and an active fluid is often described in terms of an effective temperature. Such descriptions are unhelpful when examining phase separation of active systems because it ignores the reduction of effective interaction range [105, 122].

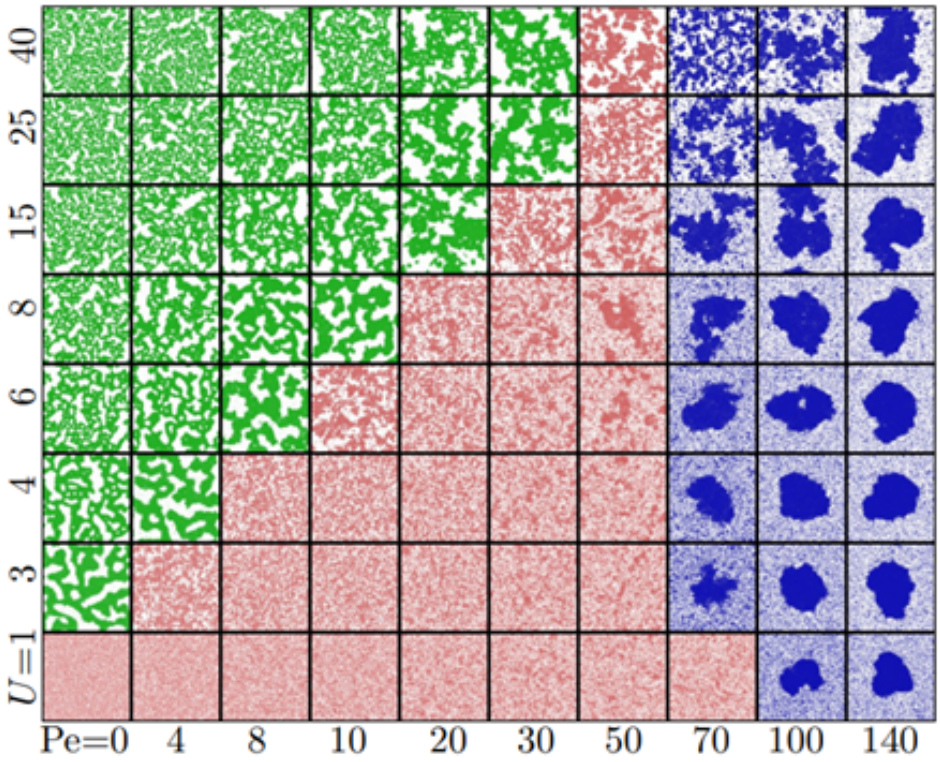

Figure 6.3 Taken from [112]. Phase diagram of active spherical particles with attractions in the Pe-U plane, describing swimming speed and attraction strength respectively. They identify three separate phases, at the top-left of the diagram a kinetically arrested gel, labelled in green, where activity opposes particle interactions and the samples slowly coarsens. In the centre, a fluid, labelled in red, where activity overcomes the particle-particle attractions. On right, a self-trapped phase-separated state, labelled in blue, where the activity is high enough to induce an active phase-separation mechanism. The attractions are modelled as Lennard-Jones potentials, with a minimum of U in k_BT, and the area fraction, $\phi = 0.4$.

The work discussed so far has been focused on two-dimensional samples. Most properties appear to be preserved as samples transition to three-dimensions, with a few exceptions[89, 133]. Phase separation in three-dimensions often occurs from the nucleation of a single cluster, whereas in two-dimensions nucleation is more homogeneous which then coarsen into a single cluster. The critical Péclet number for self-trapping is also higher for three-dimensions. The clusters formed in three-dimensions are less crystalline. Finally, the long-time aggregation kinetics appear slightly enhanced for three-dimensions.

Further, the transition from two to three-dimensions corresponds to an increased

importance of hydrodynamic interactions [37, 42]. For passively aggregating particles in three-dimensions, the inclusion of hydrodynamics dramatically alters the local particle structure, forming anisotropic threads of particles instead of compact clusters [116]. This effect has been noted to suppress motility induce phase separation in simulations [92]. The fact that hydrodynamic interactions of aggregating particles are ignored by many of the simulation and theoretical studies to date make it very important to attempt to replicate any of their findings qualitatively with experiments.

6.4 Phase Behaviour of Active-Passive Mixtures

Engineering materials using active particles to have desired active properties has proved difficult [31]. Because active particles are often expensive or difficult to produce in large quantities, realistic applications would aim to use as small a concentration as possible. One method to retain active properties at low densities is to dope active particles into passive systems. The effect of active particles on passive systems can be varied and depend upon system-specific features.

First, we shall review how activity alters interactions between passive particles. Work by Angelani *et al.* on 5 μm silica particles found that the presence of a bath of motile *E. coli* pushed the particles together resulting in short-lived spatial correlations or effective attraction [3].

The presence of activity-induced attractions can be explained by swim pressure, the concept that an active particle would swim away in space unless confined by walls and thus applies an active pressure on those walls [126, 138]. Swim pressure predicts that in the limit of short persistence length, $l_p < \sigma$, that active particles can be treated like depletants and thus an activity-induced depletion force can be derived. These activity-induced attractions have been shown to induce crystallisation of hard-sphere mixtures [70, 134]. Phase separation of passive particles also is still observed when the active particles have a density dependant speed [113, 163, 165]. Further, experiments and simulations have shown that the presence of active particles within polycrystals dramatically enhances the annealing process, yielding a fast method to produce near-perfect crystals [84, 85, 111].

However, in the limit $l_p > \sigma$, active particles can no longer reorientate quickly

and will accumulate in funnels [4, 46]. Gaps between aggregated particles can also act as traps for active particles, producing a pressure upon the aggregate which effectively weakens passive particle-particle attractions and can result in aggregate breakup [53, 125].

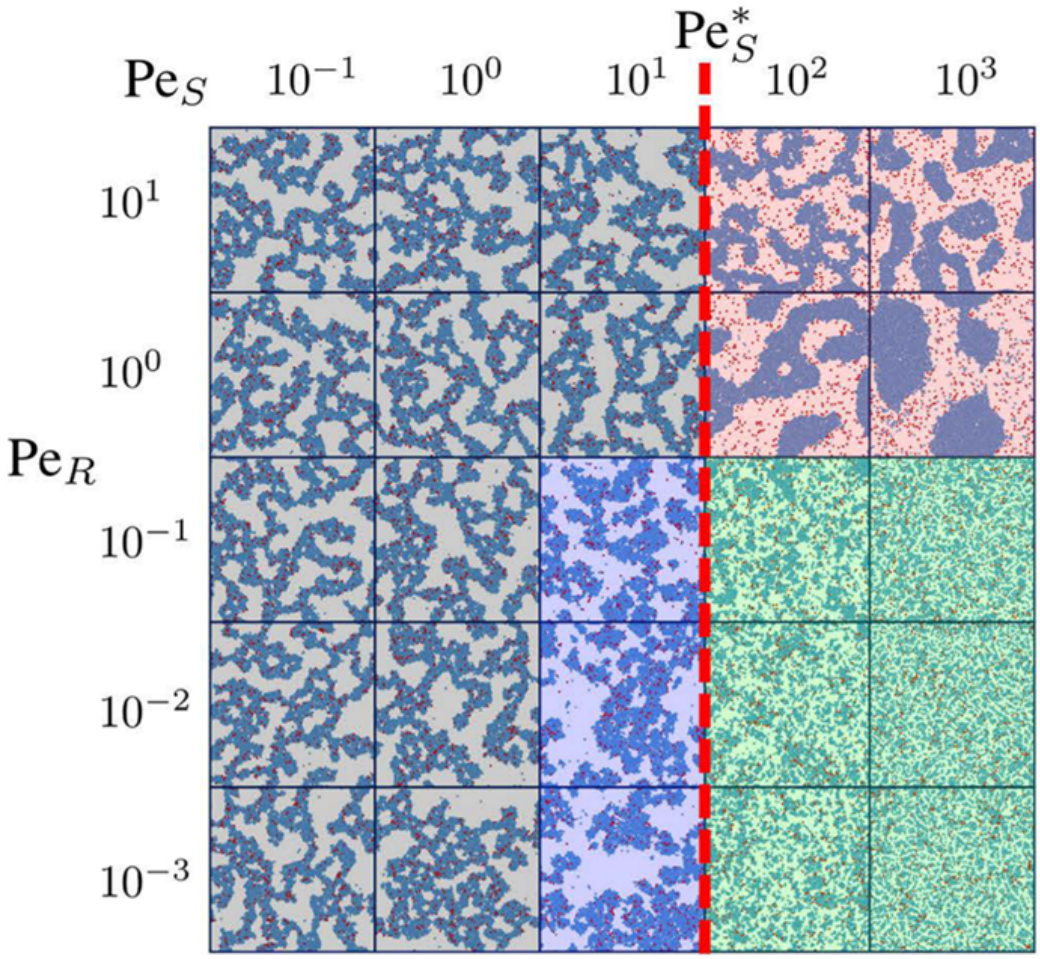

Figure 6.4 Taken from [97]. The phase diagram of a mixture of passive particles and active particles interacting via an Akasura-Oosawa depletion potential with well depth, $U = 6\ k_BT$ and range 0.12σ. The passive area fraction is set as $\phi_{pass} = 0.4$ and the active fraction is $\phi_{act} = 0.04$. The phase space is explored by changing the dynamics of the active particles, being the Péclet number, here described as a swim Péclet number or Pe_S and its reorientational Péclet number, $Pe_R = \sigma/2l_p$. The separate phases are identified by their background colour; grey-gel, blue-coarsening gel, red- activity-induced phase separation and green-fluid. Passive particles are plotted in blue and active particles in red

Only recently Omar *et al.* have started to explore how active particles change the

phase behaviour of passive particles with attractions [97], a system very similar to the one studied in this chapter. They studied, by Brownian dynamics simulations, a mixture of passive and active particles interacting via a depletion potential of depth $U = 6\ k_BT$ and range 0.12σ, with passive area fraction $\phi_{pass} = 0.4$ and active fraction $\phi_{act} = 0.04$. They explored the system's phase space by changing the active particle's swimming speed and reorientation time. The Péclet number is defined as a 'swim' Péclet number, $\mathrm{Pe}_S = \zeta v a/k_BT$, for swimming speed v and drag coefficient ζ. They also define the reorientation Péclet number as the ratio of a swimmers size to its persistence length, $\mathrm{Pe}_R = a/l_p$. As both Péclet numbers are varied, the active particle radius a is kept constant.

The phase diagram by Omar *et al.* is reproduced in figure 6.4. For slow swimming speeds, $\mathrm{Pe}_S < 100$, Omar *et al.* identified a gel phase, shown in grey and blue. These gel phases occur when the active particles are not strong enough to overcome the depletion forces and thus cannot sustainably disrupt the network of passive particles. For $\mathrm{Pe}_S = 10$ and $\mathrm{Pe}_R \leq 0.1$, shown in blue, there are signs of the active particles increasing the rate at which the gel structure coarsens, but note, the boundary between gels and activity coarsened gels will be dependent on the observation time window.

For strong swimming, $\mathrm{Pe}_S \geq 100$, Omar *et al.* observed two contrasting phases which are highly sensitive to Pe_R. For short persistence lengths, $\mathrm{Pe}_R \geq 1$, the active particles can overcome the attractive forces between passive particles and coarsen the gel network on a timescale several orders faster than for a purely passive gel. Whereas for long persistence lengths, $\mathrm{Pe}_R \leq 0.1$, the active particles break the majority of passive-passive bonds in the system, destroying the gel network, yielding a fluid phase.

This behaviour can be described by the effective interaction force between two passive particles, F^{dep}. In the limit of fast reorientations, $\mathrm{Pe}_R \to \infty$, the active particles can be treated as depletants. This interaction can be expressed in an Akasura-Oosawa form, where the contact potential is

$$F^{dep}/\phi F^{swim} = -\frac{\sqrt{1+2\beta}}{\pi \mathrm{Pe}_R} \tag{6.1}$$

where β is the ratio of passive to active particle sizes and the force is normalised by the strength of the swimmers and the swimmer area fraction, here described as ϕ. Here, the value of F^{dep} is always negative, i.e. the force is attractive. The force

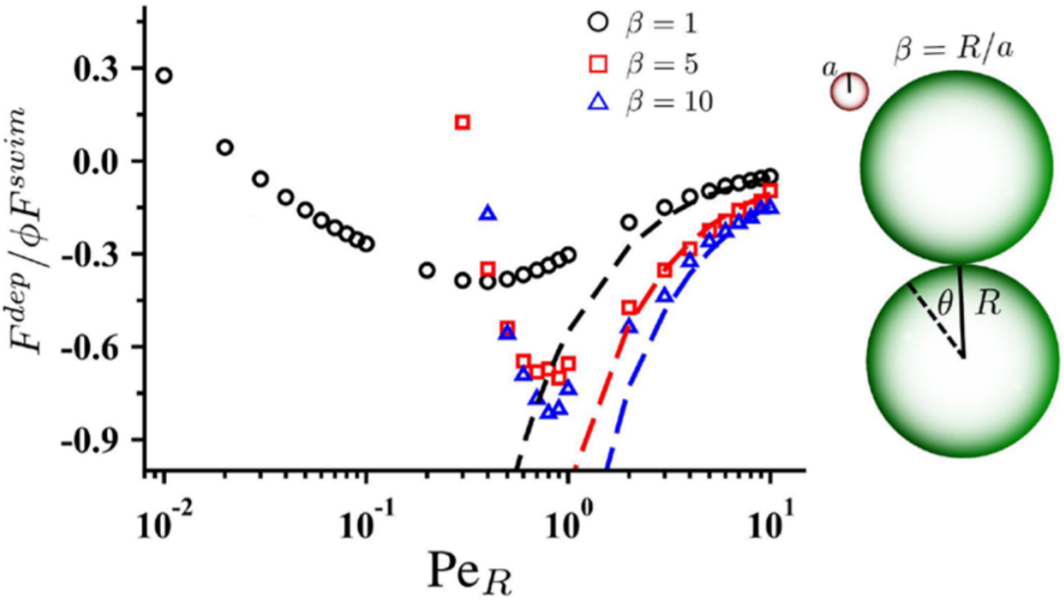

Figure 6.5 Taken from [97]. Data points show simulation results for passive particle interactions, scaled by the strength of the active bath $F^{dep}/\phi F^{swim}$, where ϕ describes the active particle area fraction, as a function of reorientational Péclet number $\mathrm{Pe}_R = \sigma/2l_p$. This is plotted for several ratios of the passive to active particle size, β, described by the inset. The dotted lines detail a predicted value for F^{dep} from a treatment of the active particles as depletants, valid in the limit of fast reorientations, $\mathrm{Pe}_R \to \infty$.

required to hold two hard discs in contact, F^{dep}, was measured from simulations. Two particles are held in contact in a large active bath, where F^{dep} is the sum of the collisional forces imparted by the active particles.

Equation 6.1 is plotted in figure 6.5 as dotted lines, along with simulation results of the interaction force between a pair of passive particles in an active bath, plotted as data points. These results show that in the limit of 'hot' Brownian particles (i.e. when the persistence is smaller than the particle diameter), you can indeed treat active particles as depletants. Unlike for depletion in binary hard-sphere mixtures, depletion still occurs for active depletants when $\beta \leq 6.\dot{6}$, or using passive nomenclature, $\xi \geq 0.15$ [15].

However for $\mathrm{Pe}_R < 1$, equation 6.1 is no longer valid, and the passive particle-particle interaction becomes repulsive. This occurs when an active particle becomes wedged in between the two passive particles. Since both the active force is stronger than the passive particle-particle interaction, and the active particle cannot reorient, the active particle swims through the pair pushing them

apart. This effective repulsion is found to increase as the active particle becomes smaller, as active particles are more easily trapped in the wedge between the passive particles [4, 46, 53].

Findings from Omar *et al.* allow some generic predictions of active-passive mixtures. Our experimental system is comprised of passive silica particles with a diameter of 1.5 μm and motile *E. coli* of width 0.85 μm and therefore $\beta = 1.75$. Taking the persistence length of the bacteria as, $l_p = v\tau_r \approx 75$ μm [123], where τ_r is the reorientation timescale and using the diameter of the bacteria as 1 μm, we find $\mathrm{Pe}_R = \sigma/2l_p \approx 10^{-2}$. The swim Péclet number, $\mathrm{Pe}_S = \zeta va/k_BT \approx 10^2$, for swimming speed, $v = 15$ $\mu\mathrm{ms}^{-1}$. This would suggest that the bacteria will introduce an effective repulsion between the passive particles.

Activity is an effective tool to explore the concept of designer phase behaviour, however, more experimental work is required to make this a reality. The work within this chapter aims to verify the ability of activity to control the phase behaviour of passive attractive systems experimentally and then further expand our knowledge of the kinetics of such systems.

Chapter 7

Activity-Induced Microphase Separation in Colloid-Polymer Mixtures

In this chapter, an experimental system is developed to study the role of motile *E. coli* on a passive phase separating system. A variety of methods are used to track the onset of phase separation and characterise the resulting microphase. These findings are then discussed within the framework of a Smoluchowski model.

7.1 Methods

Descriptions of microscope setup, sample preparation, bacteria growth protocols and particle tracking methods are described in the general methods section, section 2. Here we describe the experimental methods specific to the work in this chapter.

7.1.1 Cluster Size Measurements

The cluster size distribution is a key characteristic of a system undergoing aggregation. In this section, we identify two possible measurements of cluster sizes, which we will then review later, in section 7.4.

First, we review particle tracking and cluster identification by local proximity of neighbours. The method for identification and tracking of individual particles is outlined in section 2.4.3, to find cluster sizes we use a custom python script, which first identifies each particle's nearest neighbours. As we are dealing with depletion interactions, we simply define bound neighbours by proximity to particle i and loop through all particles. The cutoff range for neighbours is set as the $\sigma+2r_g+0.1\,\mu m \approx 1.70\,\mu m$, where the additional $0.1\,\mu m$ accounts for any particle polydispersity. We take the lists of nearest neighbours and combine any that share any particle i. The result is a series of lists each containing a unique set of particles, representing a cluster. The cluster size distribution is then the histogram of list lengths.

The weakness of tracking is its small field of view, which not only minimises the statistical significance of each experiment but also introduces errors from clusters only being partially within the field of view. So ideally, a measurement of the cluster size distribution involves sampling the largest individual areas possible. To increase the field of view we developed an unresolved-particle imaging method, which estimates cluster size from the area of each cluster.

To image the clusters without resolving individual particles, images were recorded in bright-field, with a $10\times/0.3$ NA objective recording at $3.\dot{3}$ frames-per-second. The use of an exposure time of 300 ms and bright-field imaging blurs and obscures the motile bacteria from the image. A 1 pixel gaussian blur was applied to further obscure any non-motile bacteria before a threshold was applied to the image to identify the clusters. Illumination and threshold settings were kept constant across measurements to minimise experimental variation. From the thresholded image, each cluster size is taken as being proportional to its area (we will validate this assumption in section 7.4, by direct comparison to particle resolved tracking).

Unresolved imaging is a faster method because of the larger field of view, allowing more samples to be run simultaneously. This is particularly beneficial for our experiments because immediately upon preparation, the swim speed of our bacteria slowly degrades. Running simultaneous measurements allows us to use the same bacteria stock across 5-10 samples, reducing the variation in the bacteria's swim speed and motile fraction.

Later within this chapter, we study how clusters of particle change in size over time. We utilise the 'mark' and 'recall' functions of Micro-Manager with an automated stage to ensure we study the same areas throughout each experiment.

7.2 Development of Model Passive System and Corresponding Measurements in Two-Dimensions

7.2.1 Attraction Strength

In this chapter, we tune particle-particle attractions of silica particles in quasi-two-dimensions using polymer depletion. Here, again we use sodium polystyrene sulphonate, with the radius of gyration, $r_g = 45\ nm$ and size ratio, $\xi = 0.06$. To maintain a healthy osmotic pressure on the bacteria, we use a buffer solution of 6.2 mM K_2HPO_4, 3.8 mM KH_2PO_4, 0.1 mM EDTA at pH $\sim$ 7.5. Further to stop the bacteria, and later particles, from adhering to the walls of the glass capillary, we add 0.3 wt% TWEEN20 [123]. The presence of the multivalent ions in the buffer and the surfactant, TWEEN20, also alter the particle-particle interactions [11, 125]. Comparison between the experimentally measured interaction potential and the expected values from the Asakura-Oosawa potential (equation 1.14) will allow for an estimation of the attractions induced by the salts and TWEEN20.

For low polymer concentrations, ϕ_p, and vanishing particle area fraction, η_c we can calculate the effective interaction potential, $U(r)$, from $g(r)$ [128].

$$\mathrm{g(r)}_{\eta_c \to 0} = \exp\left[-\frac{\mathrm{U(r)}}{\mathrm{k_B T}} \right] \tag{7.1}$$

where $g(r)$ is the radial distribution function, defined as

$$g(r) = \frac{1}{2\pi N r^2 \rho} \sum_{i=1}^{N} \omega_i(r) \tag{7.2}$$

$\omega_i(r)$ is the number of particles found at a radius r, for a total number of particles N and particle number density ρ.

The radial distribution function describes the probability of finding a particle centre r away from another particle centre, relative to a random distribution of points. For an ideal gas, $U(r > 1) = 0$ and $g(r > 1) = 1$ because they cannot overlap and are otherwise randomly distributed. Slight deviations in $U(r)$

correspond to slight changes in local density and thus $g(r)$. At low particle densities, $g(r)$ only probes the interaction behaviour of pairs of particles. As density increases, $g(r)$ probes the interactions of 3+ particles and no longer approximates the pair interaction potential.

For a range of low attraction strengths, with $\eta_c \approx 0.02$, $U(r)$ was calculated from $g(r)$ measurements and is plotted in figure 7.1a. Firstly, there is a significant attraction at zero polymer concentration. Secondly, these results do not look like traditional depletion potentials between hard-spheres, this maybe due to the small degree of polydispersity present in particle and polymer stocks [159]. To compare these potentials, we utilise the property that short-ranged attractions of any well shape, can be mapped onto each other if they have the same reduced second virial coefficient, B_2^* [94].

$$B_2^* = \frac{24}{\sigma^3} \int_0^\infty \left(1 - \exp\left[\frac{-U(r)}{k_B T}\right]\right) r^2 dr \tag{7.3}$$

To account for the finite attraction at zero polymer concentration, we assume the interaction strength can be defined as $\Delta U = U_{AO} + U_0$, where U_{AO} is the depletion well minimum for the Akasura-Oosawa potential and U_0 is the well minimum from electrostatic attractions mapped onto the same shape potential. The addition of these two interaction potentials is supported by studies of the potential of colloids interacting through electrostatic repulsion and polymer depletion [115]. To determine U_0, we minimise the square difference between our experimental findings and that of an ideal Akasura-Oosawa potential of the same polymer-colloid size ratio ($\xi = 0.06$), figure 7.1b. We find $U_0 = 1.5\ k_B T$, which should not effect our findings, but this detailed analysis of particle-particle interactions will be important for comparison between systems.

7.2.2 Particle Adhesion to the Surface

The disadvantage of our 2D system resting on a glass surface is particle adhesion to the glass, which can disrupt particle aggregation and phase separation. If a particle adheres to the surface, it stops diffusing, but can still aggregate with other diffusive particles. A cluster containing a single stuck particle no longer diffuse and can only rotate. The adhesion of a second particle stops the cluster rotating. Our samples contain 0.3 %wt TWEEN20 to minimise adhesion which

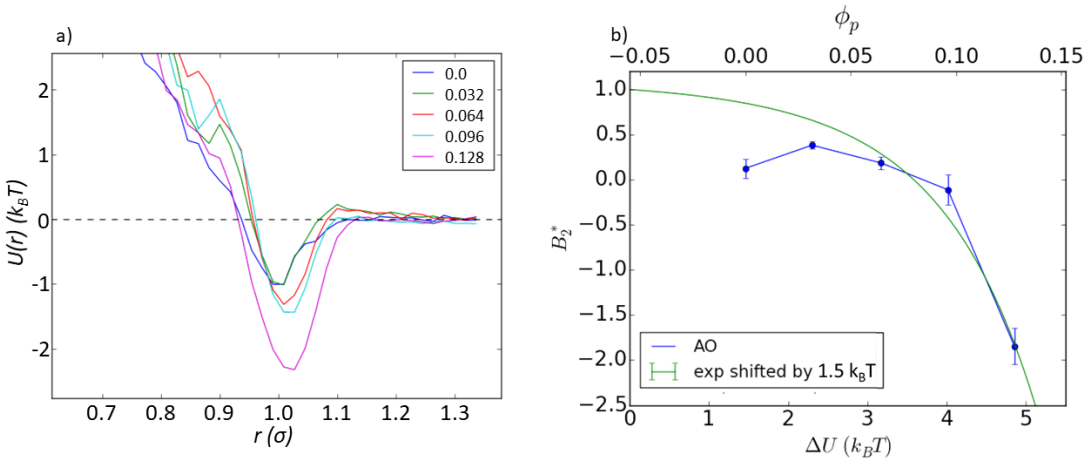

Figure 7.1 Measurements of the attraction strength between passive silica particles. a) Attractive potentials estimated from g(r) for a series of polymer concentrations, ϕ_p. b) Reduced second virial coefficients for the potentials in a, where we minimised the square difference to theory (green) with an initial offset as given by, $\Delta U = U_{AO} + U_0$ (remember $\phi_p \propto U_{AO}$). Here $U_0 = 1.5\ k_BT$.

reduces the adhered fraction significantly but does not stop adhesion totally.

Unfortunately, a detailed analysis of this important feature was prevented due to Covid-19 lab restrictions. However, with data already collected, we can still estimate the initial adhered fraction. Six capillaries were prepared with $\eta_c = 0.01$ (we will call the area fraction of particles, η_c, which is not to be confused with the polymer volume fraction, ϕ_p). The capillaries were allowed to rest on the microscope stage for 7 minutes to allow all the particles to reach the bottom and start diffusing, time-lapse images were then recorded in 3 separate locations. Each particle in the movies was then identified as either diffusive or adhered, giving a final adhered fraction of 0.05 ± 0.05 (number of adhered particles/total number of particles), where the variation was observed between capillaries and not across each sample. This fraction may increase over the duration of the experiment [156].

7.3 Passive Phase Diagram

The phase behaviour of the passive colloid-polymer system, with a polymer-colloid size ratio of $\xi = 0.06$, is plotted in figure 7.2a. Each sample was allowed to age for $\approx$ 2 hours, by which time the phase of the system is clear by direct

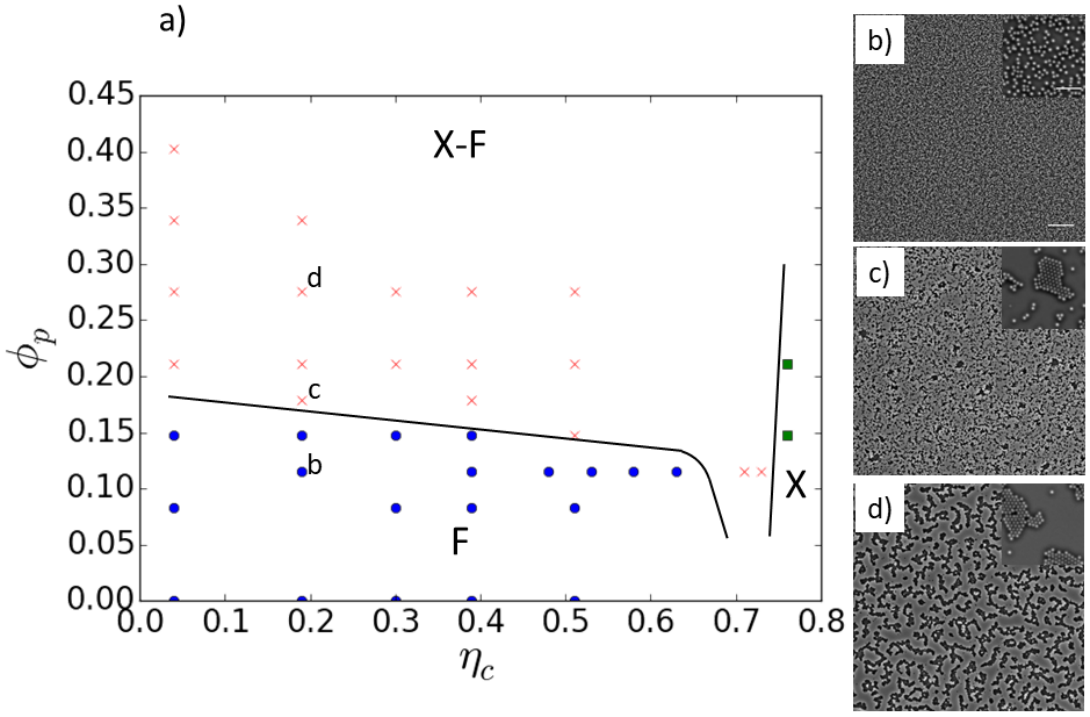

Figure 7.2 Phase behaviour of the 2D passive system. Blue circles = fluid, red crosses = crystal-fluid equilibrium and green squares = crystal. The dotted lines mark the phase boundary and are there to guide the eye. The scale bar represents 50 μm and the inset scale bar represents 10 μm.

observation alone, as shown in figure 7.2b-d. At low ϕ_p (b), we observe a fluid in which the particles freely diffuse. As the polymer concentration is increased to $\phi_p = 0.166$ (c) we see the emergence of crystalline rafts within the fluid. As ϕ_p is further increased (d), the crystalline fraction increases and the fluid fraction decreases. The fluid and fluid-crystal coexistence regions of the phase diagram are labelled as F and F-X respectively.

We find good agreement between the observed phase behaviour of our system and that of the limited literature for 2D colloid-polymer mixtures [34, 35]. These experimental and simulations study the onset of fluid-crystal coexistence at the wall in mixtures of binary hard spheres, where the smaller spheres act as depletants and the larger ones undergo phase separation. Note, here both types of particles can diffuse into the bulk. For a system with size ratio, $\xi = \sigma_S/\sigma_L = 0.11$, Dinsmore *et al.* observe the onset fluid-crystal coexistence at the wall for $\phi_L \approx 0.07$ and $\phi_S \approx 0.14$ [35]. The boundary identified by Dinsmore *et al.* is close to ours (albeit slightly lower) and the shape of the boundary agrees well (a slight decrease with increasing large particle fraction). These literature results informed

the shapes of the phase boundaries plotted for η_c >0.5, where we have limited results.

Due to the monodisperse particle stock, the initial aggregation forms crystal grains. As grains come into contact they aggregate, but often have misaligned unit cell axes, and thus the final crystalline cluster will contain a grain boundary. The number of these grain boundaries within a cluster increases with the number of crystal grains that aggregated to form it, i.e. they become polycrystalline. For high polymer concentrations, $\phi_p > 0.230$, and low to moderate area fractions, $\eta_c < 0.4$, the aggregation of several crystalline grains with misaligned axes results in a macroscopically gel-like structure. Therefore, even though these structures are technically polycrystalline, it makes more sense to think of them as crystalline gels.

For this system, there is a finite probability that when a particle reaches the bottom surface, it will land on top of a pre-formed cluster. Furthermore, as ϕ_p increases, it becomes less likely that these strong tetrahedral clusters can rearrange into planar clusters. Such events can lead to the formation of a second layer of particles and the probability that it occurs increases with both η_c and ϕ_p. For high densities, $\eta_c = 0.75$ we are able to form reasonable monolayer polycrystals for a small range of attractions, labelled as X in figure 7.2a. Less buoyant particles will suppress the formation of a second layer and should expand the accessible polycrystalline region.

We will focus on experiments at $\eta_c = 0.2$ for the remainder of this chapter unless otherwise specified. At this low particle density, the second layer effects are minimised, but clusters can grow to reasonable sizes within the experimental timescale. It is possible to do some basic experiments within the crystalline phase, which we will review in section 7.11.

7.4 Cluster Size Measurements

Two separate methods for measuring cluster size in real space were outlined in section 7.1.1, by either tracking all of the particles within an image and building clusters by local proximity or by careful image processing to measure the area covered by each cluster in pixels. The analysis of clusters by tracking individual particles is the more traditional of these approaches but suffers from slower data

acquisition, larger data volume requirements and longer analysis times than the image processing method. We will proceed to show that these methods generate the same results, which will allow us to use the faster data acquisition of the image processing method to run many samples in parallel with an identical bacteria stock.

To compare the two methods, we initially perform a direct comparison across the same experimental field of view. To ensure a fair comparison, we took a single micrograph for image processing at $\times 10$ magnification, and then rastered across the same area taking photos for particle tracking $\times 50$ magnification using the Micro-Manager 'create grid' function. For the particle tracking method, this required stitching these images together in ImageJ. The process of re-imaging the same area at high magnification takes several minutes, so to ensure a fair comparison, we prepared a sample which would not significantly change during the imaging sequence. To suppress clusters evolution, TWEEN20 was removed from the buffer solution with PSS, $\phi_p = 0.326$. Upon sedimentation, the silica particles still diffuse and aggregate normally, but within a few hours, a significant fraction of the particles adhere to the surface, stopping further cluster evolution.

The results are reported in figure 7.3, and show good agreement for most cluster sizes. There is a strong disagreement at very small sizes because the tracking method generates many more false particles, this occurs because we initially stitched 25 images, resulting in $\times 25$ more dirt in the tracked raw data than for the processed results. These anomalous data points can be removed in dynamic particle tracking, as they are observed to not move.

We repeat this cluster size analysis comparison for samples containing motile bacteria, as these are the samples we are most interested in. To avoid analysing the bacteria, we need to take care when processing the data. For tracking, this involves applying a $\sim$1 pixel blur to the image and followed by a careful choice of threshold. For the image processing method, we select a large exposure time of 300 ms, which blurs swimming bacteria over $\sim$3 body lengths.

Figure 7.4 shows the comparison of cluster size distribution measurement methods for a sample with parameters, $\phi_p = 0.454$ and $c_B = 1.7 \times 10^{-3}\,\mu m^{-2}$. The measured number of clusters c_n of size n is normalised by the total number of clusters identified c. The use of lower magnifications allows the image processing method to sample a significantly larger area of the sample than the particle tracking, greatly reducing noise from the measurement. For example, in the

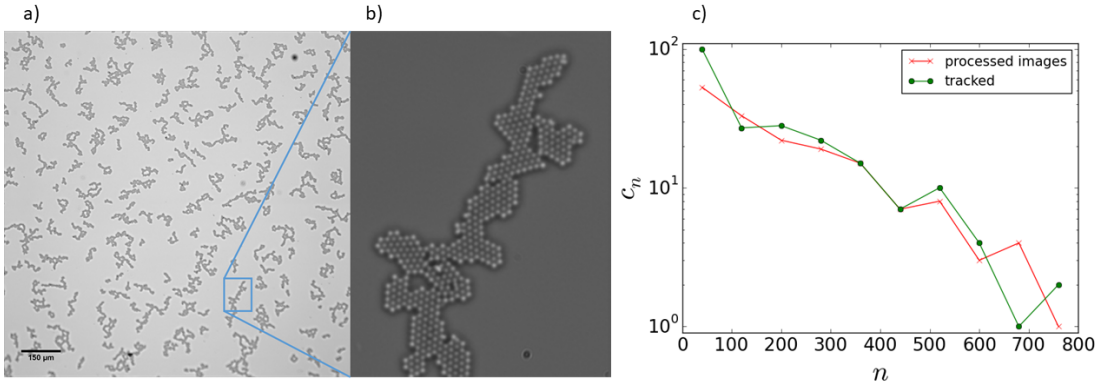

Figure 7.3 Comparison of methods for identifying and measuring cluster size distribution. a) Micrograph recorded with a ×10 objective, which was then analysed by the image processing method. b) An enhanced section of the stitched micrograph recorded with ×50 objective, which was then analysed by particle tracking c) Comparison of cluster size distributions from processed images and particle tracked images.

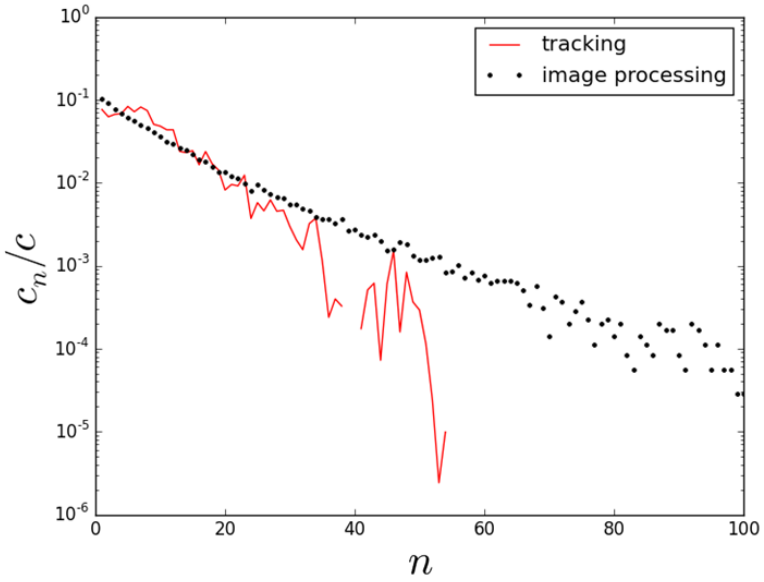

Figure 7.4 Comparison of methods for identifying and measuring cluster size distribution for samples containing bacteria. Sample parameters are $\phi_p = 0.454$ and $c_B = 1.7 \times 10^{-3}\,\mu m^{-2}$.

tracking measurement, noise at large n is seen as a sudden drop in c_n around $n = 50$, which is amplified by the logarithmic axis. Image processing also has the advantage of acquisition speed, allowing multiple experiments to be done in parallel with an identical bacterial stock, as such will be the sole cluster size

measurement used from here on.

7.5 Suppression of Phase Separation by Smooth Swimmers

In this section, we will study the effect of motile bacteria on the phase behaviour of a 2D colloid polymer by direct observation. A range of samples were prepared and allowed to quench on a microscope stage for ~ 2 hours, after which they were imaged with a $\times 50$ magnification objective. Representative cropped images of each sample is shown in figure 7.5. Focusing on the top row, increasing ϕ_p from left to right reproduces the previously discussed passive phase diagram, with fluid phases for $\phi_p \leq 0.134$, highlighted in red, and crystal-fluid coexistence at $\phi_p > 0.166$, highlighted in blue. For high polymer concentrations, $\phi_p \geq 0.262$, this equilibrium description is no longer suitable as each cluster starts to appear gel-like due to the onset of diffusion-limited cluster aggregation (DLCA). Samples undergoing DLCA will keep aggregating until a system-wide particle network has formed, and not tend to the equilibrium state of one large crystal in the middle of the sample in exchange with an almost non-existent gas fraction.

As we transition to the lower panels, we slowly increase the bacterial concentration, c_B. The bacteria are visible in these bright-field micrographs as faint obround shapes. For low polymer concentrations, $\phi_p \leq 0.134$, the addition of bacteria have little noticeable effect on the phase behaviour of the colloids but do appear to yield a small increase in local colloid density. However for $\phi_p = 0.166$, the addition of bacteria appears to limit the formation of large crystalline clusters, and for the largest bacterial concentrations, almost no crystal is present. As $\phi_p \rightarrow 0.422$, the presence of bacteria appears to limit the formation of clusters by diffusion-limited cluster aggregation and instead yields more round clusters. The addition of bacteria to mixtures with high attraction strengths also yields an increase in the concentration of smaller clusters, this becomes increasingly significant as $c_B \rightarrow 5.7 \times 10^{-2}\,\mu m^{-2}$, where the entire system is unable to form large crystalline clusters. We will go on to show that these samples are microphase-separated, highlighted in green.

As shown in figure 7.5, it is clear that the addition of smooth swimming *E. coli* results in a suppression of phase separation of the 2D colloid-polymer mixture.

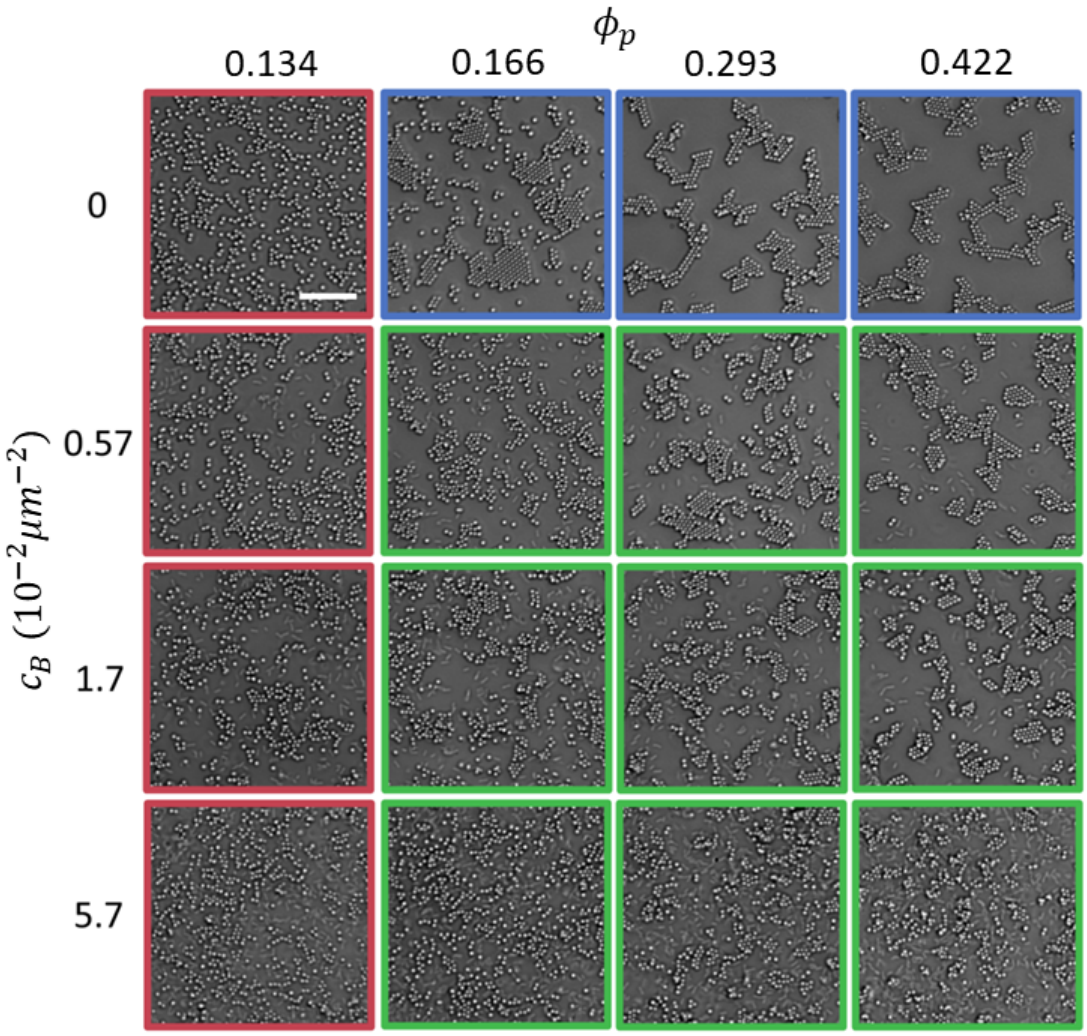

Figure 7.5 Representative micrographs of the system as polymer concentration, ϕ_p and bacterial concentration c_B are varied. We identify 3 separate phases; fluid (red), phase-separated (blue) and microphase-separated (green), obtained using the particle-resolved imaging. Imaged after 120 minutes. Scale bar represents 20 μm.

To understand how the bacteria hinder phase separation, we will explore one representative example of a bacteria breaking a cluster apart. Figure 7.6 shows a bacterium (highlighted in green) on a collision course with a crystalline colloidal cluster ($\phi_p = 0.422$). On collision, the head of the bacterium becomes pinned between the surface of glass and two particles for $\sim$0.5 s, while stuck the precessive motion of the bacterium is still observed. After $\sim$0.5 s, the bacterium dislodges several colloidal bonds to cut the cluster along a crystal unit cell axis, allowing the bacterium to swim through the cluster. The act of a bacterium swimming through the cluster pushes the two halves the bacterium's diameter

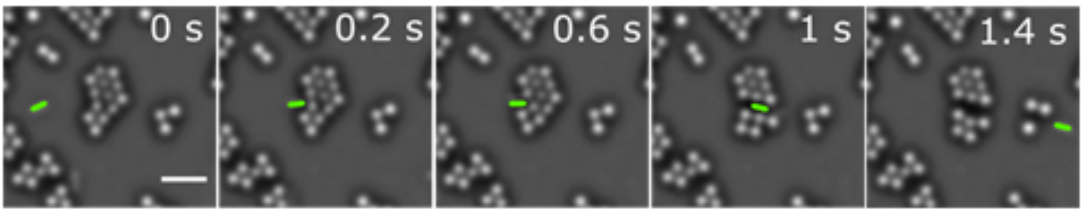

Figure 7.6 A series of micrographs over a period of 1.4 s, depicting a bacterium (manually highlighted in green) colliding with a small crystalline cluster and breaking it in two, with parameters, $\phi_p = 0.422$, and $c_B = 1.7 \times 10^{-4}\,\mu m^{-2}$. The scale bar represents 5 μm

apart, which is out of the range of depletion attraction, stopping the cluster from immediately reforming. For systems with low polymer concentrations, $\phi_p \leq 0.230$, the forces holding clusters together are significantly weaker allowing the bacteria to immediately break clusters apart.

7.6 System Dynamics

So far within this work, we have observed how motile bacteria can enhance particle diffusion, which could lead to enhanced cluster aggregation rates and we have also observed bacteria fragmenting clusters, which suppresses aggregation. It becomes interesting then to ask, how does the addition of motile bacteria affect the aggregation rate of passive particles?

For the aggregation of passive, purely attractive colloids clustering by diffusion-limited cluster aggregation (DLCA), the mean size, $\bar{n}$, obeys $\bar{n} \propto t^Z$ for a time t and exponent Z. For cluster dilute systems, being systems in their stages initial aggregation or of very low particle fraction ($\eta_c \sim 0.01$), $Z \sim 0.8$ [83], and as the system becomes cluster dense the exponent increases to $Z = 1$ due to crowding effects [44, 76, 101]. The process of DLCA will continue until the system only contains a single cluster.

We examine the aggregation dynamics in detail for samples with $\phi_p = 0.326$. The average cluster size, $\bar{n}(t)$, is measured over time for a sample without bacteria, $c_B = 0$, and plotted in blue in figure 7.7a. The initial exponent $Z \sim 0.6$ is lower than expected for true DLCA and slowly but continuously decreases with time.

There are two key differences between our experiments and the previously

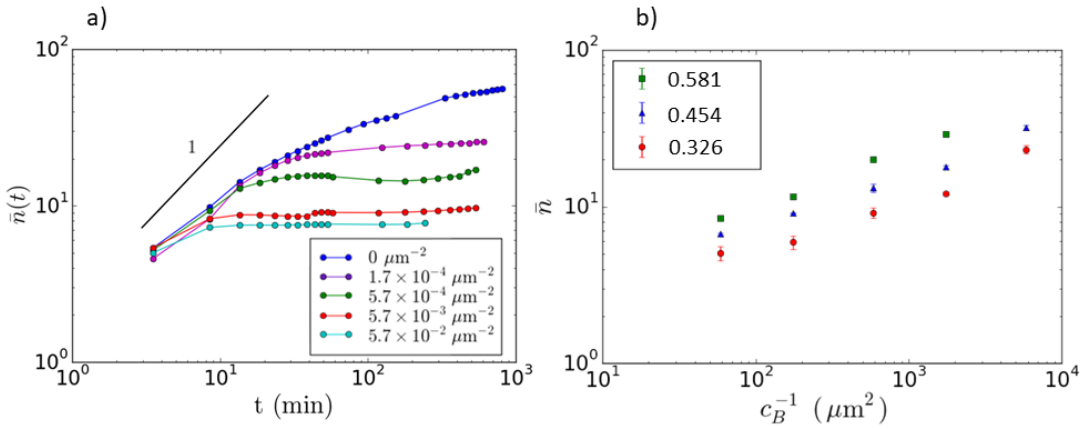

Figure 7.7 a) Average cluster size, $\bar{n}(t)$, for systems with various bacteria concentrations over time, $\phi_p = 0.326$. The black line has an exponent of 1. b) Scaling of the average cluster size at steady state, $\bar{n}$, with the inverse bacterial concentration, for a series of polymer concentrations, ϕ_p. Error bars depict standard error across samples.

mentioned experiments simulations and theory that account for the difference in Z [44, 76, 101]. Firstly the start time of the aggregation process is poorly defined as some particles start on the surface at $t = 0$ and can immediately start aggregating, while the rest slowly reach the surface over 5 minutes. The second problem is that a small fraction of the particles can adhere to the surface and stop diffusing. If a single particle in a cluster adheres to the surface, that cluster will no longer be able to diffuse and if a second particle adheres, the cluster will not be able to rotate either. Even if the number of adhered particles is fixed, the impact on the aggregation rates increases over time as the number of clusters decreases as aggregation proceeds, and thus the probability of a cluster partially adhering to the surface continuously increases. An added complication is that for colloids on glass surfaces, the fraction of particles adhered to the surface increases over time [156], which will compound the reduction in the aggregation rates.

Next, we examine how the addition of motile bacteria changes the passive aggregation dynamics. In figure 7.7a we plot $\bar{n}(t)$ for a range of bacterial concentrations, c_B. All samples show a negligible difference to the passive sample at short times, but suddenly reach a steady-state value which decreases with increasing bacterial concentration. The constant values for the average cluster size over an order of magnitude of time indicate that the sample will never completely phase separate, and the samples are therefore in a microphase-separated state. Note, the slight deviations in steady-state value of $\bar{n}(t)$ for 5.7

$\times 10^{-4}$ and 5.7×10^{-3} μm^{-2} coincide with deviations in bacterial speed due to oxygen consumption and later depletion [123].

Taking the steady-state cluster size, $\bar{n}$, as the average size measured after $t =$ 120 minutes, we investigate the dependence on c_B and ϕ_p. There appears to be a power law relationship between c_B and $\bar{n}$, see in figure 7.7b, which is investigated in detail in section 7.9.

Increasing ϕ_p corresponds to an increase in steady-state size for all c_B. As noted by direct observation, the bacteria do not immediately break clusters apart on contact, they get wedged at the edge of the clusters for a short period of order 0.1 s for $\phi_p = 0.326$ until the bacteria push into the cluster. This breakup timescale is well documented for passive colloidal systems, known as the Kramers escape time [68, 127]. The passive escape time has been adapted for the escape time of two bacteria swimming in opposing directions, and matches experimental observations [122], both active and passive models predict an increase in timescale with attraction strength. While our system is more complex than these theoretical systems from the literature, we expect an increase in escape time with increasing ϕ_p, which will result in a lower breakup event frequency and thus a larger average cluster size. This effect also controls the relationship between $\bar{n}$ and c_B, where higher concentrations of bacteria yield more frequent breakups and smaller average cluster sizes. For dopant levels of motile bacteria, this simplistic model would suggest that the breakup rate increases linearly with c_B, which will be reviewed in section 7.9.

These bacteria containing samples are not able to completely phase separate, i.e. they are microphase-separated. Microphase separation is a well-studied phenomenon within soft matter, which occurs when two opposing forces are present on the phase separating material, one force promotes phase separation while the second suppresses it. While most well studied in block copolymers [9, 78], microphase separation is also known to occur for colloids with short-ranged attraction and long-ranged repulsion [115, 135]. Microphase separation has also been found in systems of active particles with short-ranged attractions [122, 143], where the active forces act as a repulsion. For our system, microphase separation occurs due to the competition between the short-ranged depletion attraction and bacteria-induced breakup of the clusters, which can be considered as an effective repulsion. This represents a new method to achieve microphase separation due to the temporal and spatial heterogeneity of the effective repulsion.

7.7 Analysis of the Phase Boundary

We have observed that motile bacteria can swim through clusters, fragmenting them and stopping full phase separation. On the other hand, literature reports that for non-phase separating systems, the addition of motile bacteria can push colloids together, creating effective attractions between the colloids for the short time period that the bacteria continue to push them, order of 0.1 s [3]. The presence of activity-induced attractions between particles may lead to enhanced phase separation, or at least shift the phase boundary. To help understand these opposing effects, and resolve whether either lead to a shift in the phase boundary with increasing activity, we investigate if the addition of motile bacteria changes the onset of phase separation.

The phase behaviour of passive colloid polymer mixtures is well understood and was reproduced for our system in section 7.3, where the boundary is marked by a dramatic shift from small lived clusters of 3-4 particles to stable crystalline rafts of 100s of particles, which continuously grow. For our samples containing motile bacteria, such a dramatic shift is not observed.

To develop a robust understanding of the phase transition we shall review several methods for analysing the same experimental data and compare the results. We will start with the simplest method, the number of neighbours, $\bar{N}_j$, where neighbours are defined by proximity. We then proceed with the bond-orientational order parameter, ψ_6, which analyses the bond angles of neighbours with the aim of identifying crystalline structures. Finally, we will review the radial distribution function, $g(r)$, which details the relative probability of finding a particle, at radius r, from an initial particle and averaged over all particles in the system. We will expand on $g(r)$ analysis by defining a new order parameter, Λ, extracted from $g(r)$ results, which identifies the formation of a second shell of crystalline particles.

The average number of neighbours, $\bar{N}_j$, where a nearby particle is defined as a neighbour if their centre-to-centre distance of less than 1.3 σ. The cut-off limit is larger than the particle diameter plus the polymer depletant diameter, $\sigma + 2$ $r_g = 1.06$ σ, to account for polydispersity effects. If each particle is separated from every other particle by at least 1.3σ, then $\bar{N}_j = 0$, whereas for a perfect hexagonal close packing, $\bar{N}_j = 6$. For fluid states, some particles appear in contact momentarily, giving a non-zero value for $\bar{N}_j$.

The average number of neighbours is detailed over a range of attraction strengths in figure 7.8, for a series of bacterial concentrations. For the passive samples (black), we observe an abrupt increase $\bar{N}_j$ around $\phi_p = 0.134$, representing the phase transition and $\bar{N}_j$ decays fractionally for $\phi_p \geq 0.262$, indicating the transition from round clusters formed by reaction-limited cluster aggregation (RLCA) to string-like clusters formed by diffusion-limited cluster aggregation (DLCA).

For the lowest concentration of bacteria (purple), $\bar{N}_j$ has similar values to the passive samples for low and high ϕ_p but omits the RLCA peak. Active samples have been observed to have larger concentrations of smaller clusters and single particles, which causes $\bar{N}_j$ to decrease with increasing bacterial concentration. The relative trend in $\bar{N}_j$, i.e. at what attraction strength it starts to grow, is the important feature for samples containing bacteria, for which there is no significant difference between any of the samples. This suggests that the phase boundary does not shift with increasing bacterial concentration, but just that within the phase-separated region, increasing bacterial concentration decreases the degree of phase separation.

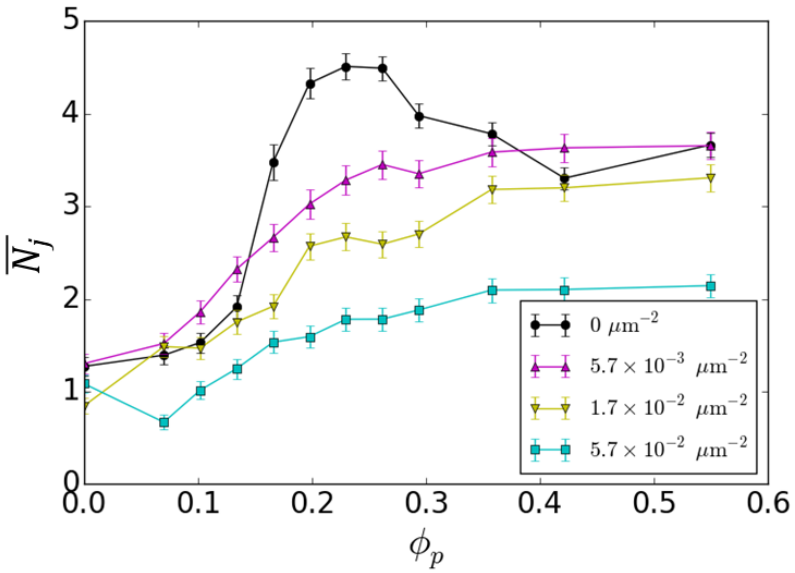

Figure 7.8 The average number of neighbours, $\bar{N}_j$, as a function of attraction strength over a range of bacterial concentrations

Alternatively, we can use the crystalline microstructure of the phase-separated sample to study the phase boundary. A popular method for determining the onset of crystallisation is the bond-orientation order parameter, ψ_6 [132, 168]. This method relies on the fact that for a perfect hexagonal close-packed crystal,

every particle i has 6 neighbours each in contact and evenly spaced 60° apart. The bond angle, θ_{ij}, is defined as the angle between particle i and j and an arbitrary and constant reference axis. For each particle, an order parameter is calculated

$$q_6(i) \equiv \frac{1}{N_j} \sum_{j \in \mathcal{N}(i)} e^{i6\theta_{ij}} \tag{7.4}$$

with N the total number of particles and N_j the number of neighbours to particle j, where the definition of a neighbour remains based on proximity alone, i.e. two particles with a centre-to-centre distance of less than 1.3 σ. Note that the exponent i in equation 7.4 is the imaginary unit, and does not refer to particle i. Here we specify N_j for particle i, instead of dividing by 6, otherwise, the results would be dominated by edge effects.

The value $|q_6(i)|^2$ describes the local ordering around particle i, where for perfect hexagonal close packing, $|q_6(i)|^2 = 1$, and for a sample with no crystalline order, $|q_6(i)|^2 = 0$. The bond-orientational order parameter is then defined as the average over all particles i

$$\psi_6 \equiv \left\langle \left| q_6(i) \right|^2 \right\rangle \tag{7.5}$$

The bond-orientational order parameter is plotted as a function of ϕ_p, for a range of bacterial concentrations, in figure 7.9. For the passive samples, shown in black, at low attraction strengths, any clusters are non-crystalline resulting in $\psi_6 = 0$. Above $\phi_p = 0.134$, clusters enter the RLCA regime and are able to undergo rearrangements, resulting in a highly crystalline structure. As ϕ_p increases further, rearrangements become significantly slowed as the system crosses into the DLCA regime, which results in more grain boundaries and importantly the formation of tetrahedral structures within the 2D crystals. The emergence of particles on top of the monolayer form tetrahedra, which disrupts particle tracking, leading to an artificially low value of ψ_6. This fluid to RLCA to DLCA is again represented as a peak in the order parameter as a function of ϕ_p.

Upon addition of bacteria, ψ_6 still starts to increase around $\phi_p = 0.134$, but instead of reaching a peak value, ψ_6 reaches a plateau around $\phi_p = 0.358$. As bacterial concentration is increased, the sample becomes less crystalline at all

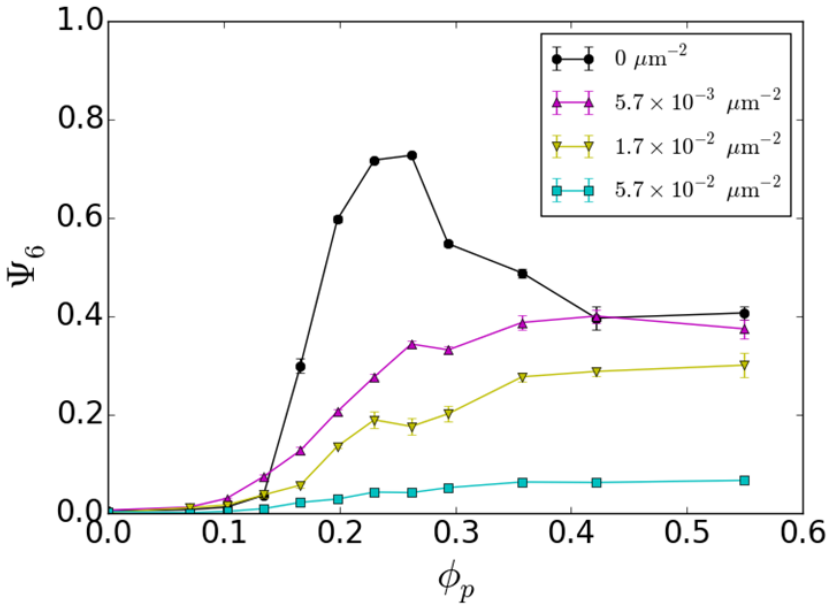

Figure 7.9 The bond orientational order parameter, ψ_6, as a function of attraction strength over a range of bacterial concentrations

attraction strengths tested.

The final method we will review is the radial distribution function, $g(r)$. As described earlier, the radial distribution function is defined as

$$g(r) = \frac{1}{2\pi N r^2 \rho} \sum_{i=1}^{N} \omega_i(r) \tag{7.6}$$

where $\omega_i(r)$ is the number of particles found at a radius r, for a total number of particles N and particle number density ρ.

The radial distribution function, $g(r)$, has previously been shown to be effective for studying phase transitions in samples undergoing a freezing transition by observing the splitting of the second peak in monodisperse samples [19, 141] or the shift of the first minima in polydisperse samples [117]. For passive samples just above and below the phase transition $g(r)$ is plotted in figure 7.10, as attraction strength is increased each sample is shifted by 1 for clarity. Due to the highly monodisperse sample, the phase transition is observed as the formation of a new peak at $\sqrt{3}\sigma$, highlighted in yellow (as opposed to the splitting of the 2σ peak). The peak at $\sqrt{3}\sigma$ is the first peak uniquely associated with the hexagonal close-packed structure, where the particles are located at the far vertices of a rhombus,

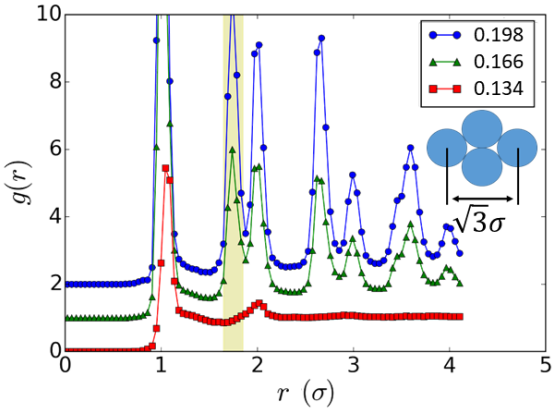

Figure 7.10 Radial distribution functions, $g(r)$, for passive samples over a range of attraction strengths, showing the growth of crystalline peaks in the transition from a fluid ($\phi_p = 0.134$) to fluid-crystal coexistence ($\phi_p \geq 0.166$). As attraction strength is increased, each subsequent distributions is offset by +1 for clarity. The inset shows the crystalline structure which gives rise to the peak at $g(r = 1.73\sigma)$, these peaks are highlighted in yellow.

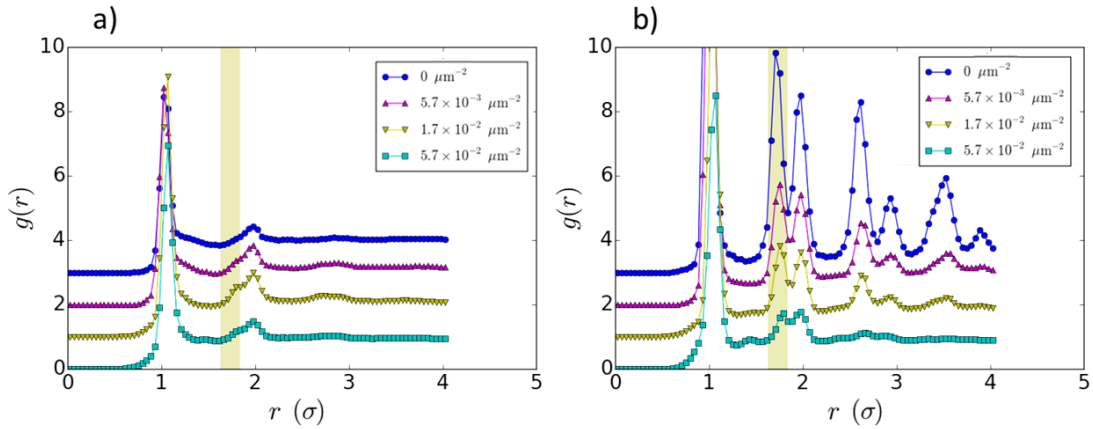

Figure 7.11 Radial distribution functions, $g(r)$, for samples with varying bacterial concentrations, plotted for a) $\phi_p = 0.134$ and b) $\phi_p = 0.294$. The highest bacterial concentrations are plotted at the bottom and subsequent distributions are offset by +1 for clarity. The region in yellow highlights the $r = 1.73\sigma$ peak, the first peak purely associated with crystalline ordering, see the inset in figure 7.10 for the related structure.

as depicted in the inset of 7.10.

The radial distribution function is also plotted for samples with $\phi_p = 0.134$ and 0.294 over a range of bacterial concentrations, figure 7.11a and b respectively. The bacterial concentration is increased going from the blue to the cyan data. For ϕ_p

= 0.134 a slight shoulder emerges at $r = \sqrt{3}\sigma$ for samples containing bacteria, which indicates that there might be a small shift in the phase transition, but the difference in behaviour is so small is not particularly significant. Observations by Angelani *et al.* [3], that the addition of motile bacteria to a dilute colloidal suspension induces effective attractions between the colloids may explain this pre-transition behaviour, i.e a combination of polymer depletion and activity-induced attractions may allow for the formation of small short-lived clusters.

However, for samples with $\phi_p = 0.294$, $g(r)$ plots show a suppression of phase separation with increasing activity, as indicated by the suppression of the peaks in figure 7.11b. For the highest bacterial concentration tested (cyan), some peaks are entirely lost due to the decrease in the steady-state cluster size. However, at the highest bacterial concentration, there is a small broad peak that forms at $r \approx 1.4\,\sigma$, the additional separation of 0.4σ is approximately a bacterium's width indicating this new peak is likely caused by frequent fragmentation events. Such peaks will likely become more prominent as bacterial concentration is increased beyond a dopant level [3].

It is clear that the $g(r)$ is an effective tool to study the details of this phase transition, however not to compare a large number of data sets. For the purpose of comparing many samples we calculate the integral of the peak around $\sqrt{3}\sigma$, defined as

$$\Lambda_{\sqrt{3}} = \frac{1}{2\Delta \mathrm{r}} \int_{\mathrm{r}'-\Delta \mathrm{r}}^{\mathrm{r}'+\Delta \mathrm{r}} \mathrm{g(r)dr} \tag{7.7}$$

where $r' = \sqrt{3}\sigma$ and $\Delta r = 0.1\sigma$. This value is a measure of the number of mid-range crystalline neighbours, meaning it is a measure of crystallinity but also cluster shape. Note for a hard-sphere fluid $\Lambda_{\sqrt{3}} = 1$, and any increase is an indication of an increase in crystallinity.

The mid-range crystalline order parameter, $\Lambda_{\sqrt{3}}$, is plotted as a function of ϕ_p for the same range of bacterial concentrations in figure 7.12. For the passive sample, we again observe an increase in crystallinity around $\phi_p = 0.134$, with a maximum around 0.230, followed by a decrease to an intermediate value. Again, this is associated with the transition from fluid to RLCA to DLCA and the corresponding change in cluster shape as well as the addition of some tetrahedral

structures within the crystal causing tracking errors.

Samples containing bacteria for $\phi_p < 0.134$ all have slightly higher values of $\Lambda_{\sqrt{3}}$ than the passive sample. The increase for low attraction strengths is due to the emergence of a small peak at $r = \sqrt{3}\sigma$, as discussed above, this slight increase in phase separation is due to activity-induced effective attractions [3]. As ϕ_p is increased, we again see the active samples starting to undergo crystallisation around $\phi_p = 0.134$. For samples with $\phi_p > 0.134$, the depletion interactions become the dominant form of attraction and increasing activity results in cluster breakup, this causes the degree of phase separation to decrease with increasing bacterial concentration.

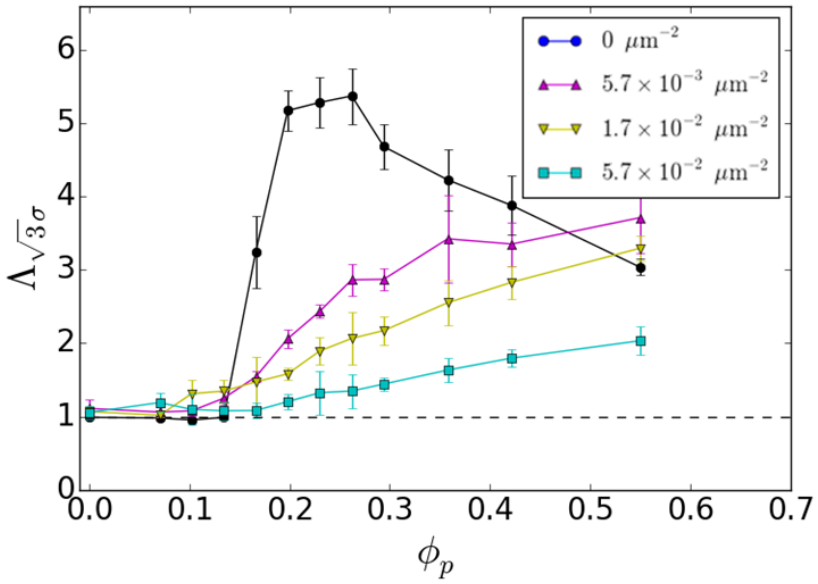

Figure 7.12 Integrated radial distribution peaks around $r = \sqrt{3}\sigma$ as a function of polymer concentration ϕ_p, for a range of bacterial concentrations, c_B. For a detailed description of $\Lambda_{\sqrt{3}\sigma}$ see text.

All of the methods used to examine phase separation yield very similar insight to the underlying processes within the system. At low polymer concentration, $\phi_p < 0.134$, all behave fluid-like. For all bacteria concentrations, we observe the onset of phase separation around $\phi_p = 0.134$, i.e. the phase boundary has little to no dependence on activity. However, the bacteria do act to limit phase separation within the phase-separated region, where increasing bacterial concentration further suppresses phase separation.

For samples containing bacteria with $\phi_p < 0.134$, the $g(r)$ results indicate the presence of small crystalline clusters. A possible explanation can be found by

considering previous work by Angelani *et al.*, who found that motile bacteria can induce effective attractions between colloids in the limit of the well depth, $U = 0\ k_BT$ [3]. A combination of activity-induced attractions and polymer depletion may be enough to allow for the formation the short-lived clusters.

Surprisingly, the addition of activity does not significantly shift the phase boundary for our experiments because activity has previously been found to shift phase transitions within the literature. For example, Schwarz-Linek *et al.* found that for samples of *E. coli* with a polymer depletant, depletant concentration required to induce phase separation increased fivefold when motility was switched on [122]. The key difference between our system and those with an activity-dependent phase boundary is that here passive-passive interactions dominate since active-passive interactions are both temporally and spatially heterogeneous.

7.8 Cluster Size Distribution

Next, we will review the cluster size distributions for samples without bacteria undergoing aggregation and also samples with bacteria while in steady state.

The cluster size distribution, $c_n(t)$ is defined as the number of clusters of size n observed at a time, t, within a given area. The cluster size distribution for DLCA has been found to follow the scaling form [151]

$$c_n(t) = M_1 s(t)^{-2} f(n/s(t)) \tag{7.8}$$

The moments are defined as $M_x = \sum_n n^x c_n$, M_1 is simply the total number of particles in the system and is time independent and $s(t) = M_2/M_1$ and the function $f(n/s(t))$ describes the shape of the distribution. This form has been verified by additional experiments and simulations for DLCA and found to give poor data collapse for RLCA [50, 54].

The cluster size distribution for a sample with parameters $\phi_p = 0.326$ and $c_B = 0$ are plotted for various times in figure 7.13a, the legend details the time in minutes at which each distribution was measured. The cluster size distribution is normalised by the total number of clusters, c, so $\sum_n c_n/c = 1$. As the sample ages, the average cluster size increases and the entire distribution shifts to the right.

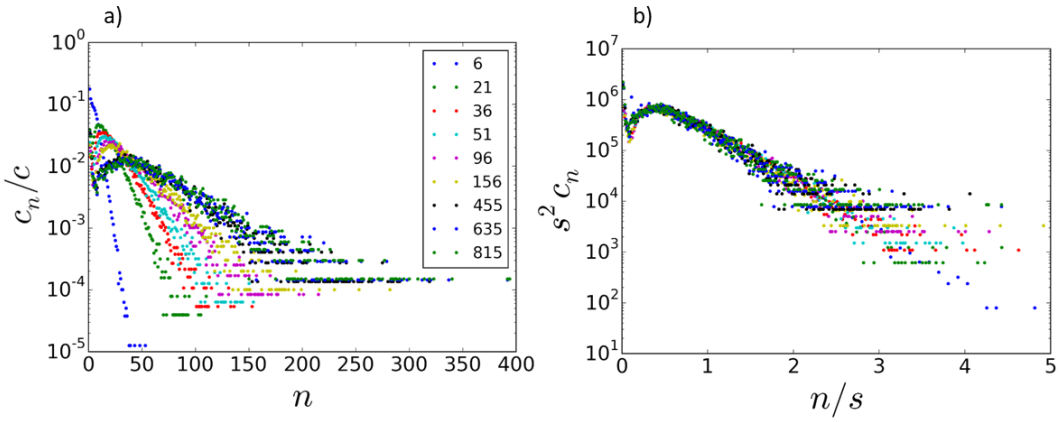

Figure 7.13 a) Unscaled and b) Scaled forms of cluster size distributions for passively aggregating clusters. The legend details the time in minutes of when the measurement was taken and the attraction strength, $\phi_p = 0.326$. The scaling of the cluster size distribution is described by equation 7.8.

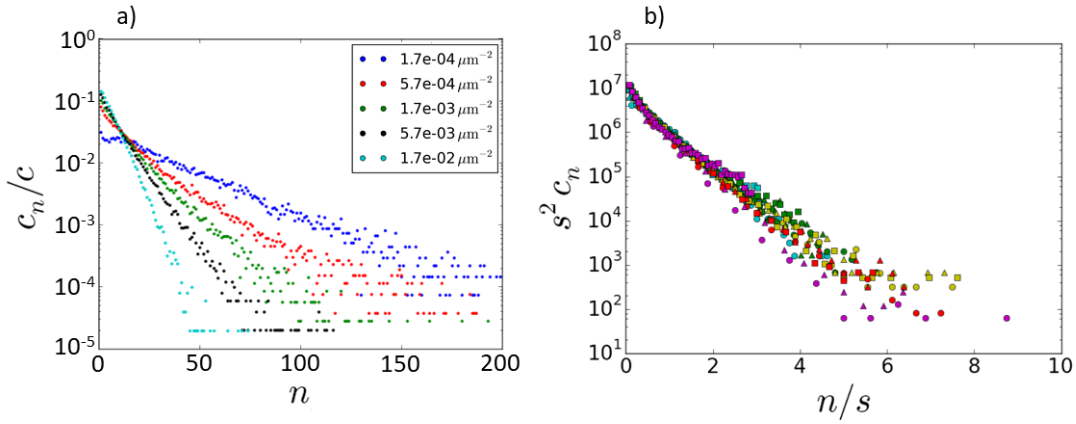

Figure 7.14 a) Unscaled cluster size distributions for samples containing motile bacteria in steady state with parameters $\phi_p = 0.326$ and bacterial concentrations detailed in the legend. b) Scaled forms of cluster size distributions for samples containing motile bacteria in steady state and varying attraction strength. Circles, triangles and squares represent $\phi_p = 0.326$, 0.454 and 0.581 respectively and bacterial concentrations 1.7×10^{-4}, 1.7×10^{-4}, 5.7×10^{-3}, 5.7×10^{-3} and 1.7×10^{-2} μm^{-2} are plotted in cyan, green, yellow, red and purple. Data within the red box is enlarged in the inset. Again, the cluster size distributions are scaled according to equation 7.8.

The distributions are scaled replotted in figure 7.13b in accordance with equation 7.8. Overall, the scaling provides good data collapse, with only a small deviation for the initial distribution at $t = 6$ minutes, where due to the quenching process, not all particles will have start undergoing aggregation. The scaled distribution

agrees well with the unimodal distribution observed in simulations for 2D DLCA [50], with the exception of our anomalously large concentrations of small clusters $n < 10$. We believe this discrepancy to be a result of the small fraction of particles adhering to the surface, which can limit cluster growth or even their initial formation.

Next, we review the cluster size distributions for samples with a range of bacterial concentrations in steady-state conditions, figure 7.14a. The addition of motile bacteria results in a significant change in the cluster size distributions, going from unimodal distributions in the passive case to quasi-exponential decays with bacteria. This change is most likely the result of activity-induced cluster fragmentation resulting in the increased concentration of smaller cluster sizes.

We scale the cluster size distributions for samples with varying polymer concentration, $\phi_p = 0.326$ - 0.581 and bacterial concentrations $c_B = 1.7\times10^{-4}$ - 1.7×10^{-2} μm^{-2}, shown in figure 7.14b. We observe that for the active samples, the cluster size distribution still scales well with equation 7.8. There is a slight exception for small clusters at the lowest bacterial concentrations, where for decreasing size, we observe a plateau in c_n followed by a sharp increase, which is obscured by this plot, but is apparent for the unscaled data, figure 7.14a. This deviation from scaling is apparent for all attraction strengths at the lowest bacterial concentration, $c_B = 1.7 \times 10^{-4}$ μm^{-2}.

One would expect that the form of the cluster size distribution, $f(n/s)$, would transition away from the active form and towards the passive form at some low bacterial concentration. The slight deviation in $f(n/s)$ at low bacterial concentration may indicate that we are close to a transition, beyond which the few bacteria would alter the cluster size distribution. We will review the form of $f(n/s)$ for the active samples in detail within the next section.

The addition of bacteria results in a significant change in the shape of the normalised distribution by increasing the concentration of small cluster sizes. This makes sense in light of the breakup mechanism, where a single bacterium can break large clusters in to two smaller ones. Interestingly, we observe excellent scaling across all bacteria concentrations and attraction strengths, suggesting that the underlying processes do not change with system parameters. We will introduce a more thorough explanation of the active cluster size distributions within the next section.

7.9 Smoluchowski Model for Aggregation-Fragmentation

The system described within this chapter, is one which constantly undergoes aggregation and fragmentation. Aggregation-fragmentation is a well-studied phenomenon and the process is described by the Smoluchowski aggregation-fragmentation equation, which describes how the concentration of clusters of size n, c_n, changes over time

$$\frac{\mathrm{d}c_n}{\mathrm{d}t} = \frac{1}{2}\sum_{i+j=n} A(i,j)c_j c_i - \sum_{j=1}^{\infty} A(n,j)c_n c_j + \sum_{j=1}^{\infty} F(n,j)c_{n+j} - \frac{1}{2}\sum_{i+j=n} F(i,j)c_{i+j}\,, \tag{7.9}$$

where $A(i,j)$ is the aggregation kernel which describes the rate of aggregation of clusters of i and j. Conversely, $F(i,j)$ is the fragmentation kernel which describes the rate of fragmentation of clusters of size $i+j$. This population balance equation has two aggregation terms due to the creation and loss of clusters of size n by aggregation, similarly for fragmentation. The factors of a $1/2$ are to get rid of double counting. The kernels are time-independent, and so the rates are only dependant on cluster concentrations and time-independent geometrical factors. Note, this is a mean field theory, meaning there are no spatial correlations between clusters, and therefore the system needs to be sufficiently dilute so the clusters can aggregate by diffusion

This model is impossible to solve analytically in general because it is an infinite set of coupled non-linear first-order differential equations. Solutions are known for simple and generally unrealistic kernels like $A(i,j) = c$ (constant) and $A(i,j) = i + j$ (additive) [14, 32], or for examples where the differentially equation can be dramatically simplified like setting $j = 1$ for the modelling of Janus particle clustering [47]. Solutions do exist for realistic systems if we are able to make a few assumptions. Below, we reproduce a general solution to the Smoluchowski model, initially shown by Family *et al.* [41] and review the assumptions therein.

There are two key assumptions made in this derivation, the first being that the kernels are homogeneous functions of their arguments $A(xi, xj) = x^{\lambda}A(i,j)$ and $F(xi, xj) = x^{\alpha}F(i,j)$, for a multiplicative factor x. The values of the homogeneity constants, λ and α, simply describe how aggregation and fragmentation scale

with cluster size respectively, i.e. rates increase with size for positive values, are independent of size for a value of 0 and decrease with size for negative values. The homogeneous scaling of the aggregation kernel has been well studied by experiments, simulations and theory [40, 76, 96, 101, 154], which show that for ideal reaction-limited cluster aggregation (RLCA) samples possess $\lambda = 1$ and diffusion-limited cluster aggregation (DLCA) $\lambda = 0$. For non-ideal samples, for example, the salt-induced aggregation of an old batch of gold colloids, where attraction strength can vary across a particle's surface due to absorption of impurities, $\lambda = -0.6$ has been reported [76, 96].

The second key assumption is that the time dependent cluster size distribution scales as described by equation 7.8 in section 7.8, reproduced below

$$c_n(t) = M_1 s(t)^{-2} f(n/s(t)) \tag{7.10}$$

Again, the moments are defined as $M_x = \sum_n n^x c_n$, M_1 is simply the total number of particles in the system and is time independent and $s(t) = M_2/M_1$. The function $f(n/s(t))$ describes the shape of the distribution and is dependent on the aggregation and fragmentation mechanisms, for $\lambda = \alpha = 0$, $f(n/s(t))$ is an exponential decay [39, 148].

To find the time derivative of the xth moment of the cluster size distribution, the Smoluchowski equation is multiplied by $(i+j)^x$ and summed over all $(i+j)$ [129]. For x=2, in continuous form, where u and v are cluster sizes

$$\frac{dM_2}{dt} = \int_0^\infty du \int_0^\infty dv\, vu[A(u,v)n_u n_v - F(u,v)n_{u+v}] \tag{7.11}$$

Substituting equation 7.10 into equation 7.11 and utilising the homogeneous scaling of the kernels yields

$$\begin{aligned}\frac{dM_2}{dt} = M_1^2 s^\lambda \int_0^\infty dU \int_0^\infty dV\, UV A(U,V) f(U) f(V) \\ - M_1 s^{\alpha+2} \int_0^\infty dU \int_0^\infty dV\, UV F(U,V) f(U+V)\end{aligned} \tag{7.12}$$

where $U = u/s(t)$ and $V = v/s(t)$.

Defining the strengths of the kernels as,

$$A(i,j) = k_A \Psi(i,j) \tag{7.13}$$

and,

$$F(i,j) = k_F \Phi(i,j) \tag{7.14}$$

where $\Psi(1,1) = \Phi(1,1) = 1$, and k_A and k_F are the aggregation and fragmentation rate constants respectively, then equation 7.12 becomes,

$$\begin{aligned}\frac{dM_2}{dt} = M_1^2 s^\lambda k_A \int_0^\infty dU \int_0^\infty dV\, UV\Psi(U,V) f(U) f(V) \\ - M_1 s^{\alpha+2} k_F \int_0^\infty dU \int_0^\infty dV\, UV\Phi(U,V) f(U+V)\end{aligned} \tag{7.15}$$

Since M_1 is a constant, due to it being the total number of particles in the system, and $\frac{ds}{dt} = \frac{1}{M_1}\frac{dM_2}{dt}$, leads to the final expression for the time derivative of the size,

$$\frac{ds}{dt} = M_1 a k_A s^\lambda - b k_F s^{\alpha+2} \tag{7.16}$$

where

$$a = \int_0^\infty dU \int_0^\infty dV\, UV\Psi(U,V) f(U) f(V) \tag{7.17}$$

and

$$b = \int_0^\infty dU \int_0^\infty dV\, UV\Phi(U,V) f(U+V) \tag{7.18}$$

The values of a and b are not strictly constant [153], but assuming they are results in minimal error [39], and allows for the prediction of the steady-state average cluster size.

When $\frac{ds}{dt} = 0$, the system has reached steady state. If at steady state we say

$s = s_0$, equation 7.16 becomes

$$s_0 = \left(\frac{M_1 a k_A}{b k_F} \right)^y \tag{7.19}$$

where

$$y = (2 - \lambda + \alpha)^{-1} \tag{7.20}$$

The exponent, y, describes the relationship between aggregation and fragmentation. Stable clusters can only form when $y \geq 0$, as dictated by equation 7.16. Systems with $y < 0$ are dominated by fragmentation, where any cluster of particles will continuously tend towards a state of individual particles.

We now proceed to test the predicted power-law dependence of s_0 vs k_A/k_F. In order to do so, we first need to test whether the assumptions made in deriving this power law are valid. First, we investigate the scaling of the homogeneity constants. To measure the homogeneity constants experimentally we need to extract the relative rates that clusters of size i convert to size j after a short time, τ.

The homogeneity constants are not expected to change with the system parameters c_B and ϕ_p because within parameter space explore here, aggregation remains firmly diffusion-limited and the fragmentation mechanism is not observed to vary, so here we will focus on one sample. The parameters $\phi_p = 0.454$ and $c_B = 1.7 \times 10^{-3}$ μm^{-2} were chosen as they are situated at the centre of the phase space of interest. After the sample was prepared, it was left on a microscope stage for 2 hours and allowed to reach steady state. Several movies were then recorded each at separate positions throughout the capillary using a $50\times/0.8$ NA objective at 50 fps with the standard protocol of bright-field illumination and a narrow aperture to enhance the visibility of the silica particles and obscure the bacteria. The clusters are tracked, and aggregation and fragmentation events are logged by custom python scripts detailed in section 7.1.1.

To calculate the relative rates that clusters of all sizes convert to all other sizes, we start by extracting the number of observed events for clusters of initial size $n_{t=\tau}$ at time, $t = \tau$, changing by aggregation/fragmentation to a cluster of final size $t = \tau + \delta$ for $\delta = 0.4$ s. The number of occurrences are normalised by

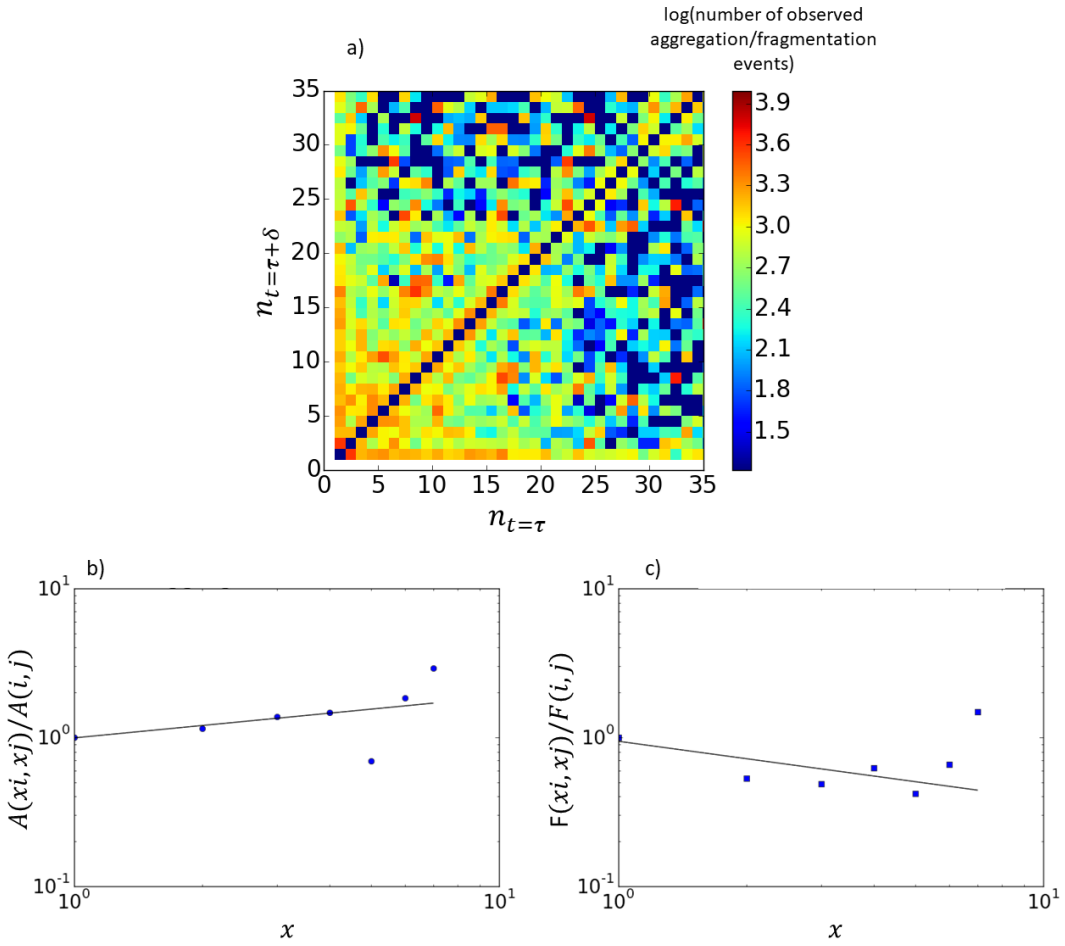

Figure 7.15 Analysis of how clusters aggregate and fragment for a sample with $\phi_p = 0.454$ and $c_B = 1.7 \times 10^{-3}$ μm^{-2} a) cluster size transition matrix, a 2D histogram detailing the number of changes from size n at time τ to the size at $\tau + \delta$, for $\delta = 0.4/, s$ (the plot only details clusters which change size in $\delta = 0.4/, s$). These values are presented as the logarithm of the number of events with aggregation events normalised by $c_1^2/(c_i c_j)$ and fragmentation by c_1/c_{i+j}. Calculation of homogeneity constants by comparing aggregation and fragmentation kernels for a given multiplier x, b) aggregation, giving $\lambda = 0.28$ and c) fragmentation, giving $\alpha =$ -0.39.

$c_1^2/(c_i c_j)$ for aggregation events and c_1/c_{i+j} for fragmentation to yield the relative rates of aggregation and fragmentation across all observed sizes. The logarithm of the number of aggregation/fragmentation events is plotted in figure 7.15a, where aggregation ($n_{t=\tau} < n_{t=\tau+\delta}$) is plotted in the upper left and fragmentation ($n_{t=\tau} > n_{t=\tau+\delta}$) is plotted in the lower right. Due to the nature of quasi-exponential cluster size distribution (figure 7.14b), we observe many more events in proximity to

the origin and thus, moving away from the origin, noise in the data becomes increasingly large.

The only other active system for which an aggregation-fragmentation transition matrix has been measured for is an experimental mixture of Janus particle clusters. Clusters of self-propelled Janus particles undergo the processes of aggregation and fragmentation of single particles with the bulk, yielding a transition matrix with dramatically larger values along the axes and diagonal [47]. For our experimental system of passive clusters being fragmented by motile bacteria, we observe little bias depicting that clusters of any two sizes can aggregate and a cluster can fragment into any pair of sizes. Even though our results are only shown up to a cluster size limit, $n = 35$, we expect clusters of any possible size to be able to fragment to any other size. Due to the fractal nature of the clusters formed, branch thickness does not increase as size, therefore very large clusters are expected to fragment in a similar manner to the smaller ones observed in this work.

We use the data collected in figure 7.15a to test the assumption of the homogeneous scaling of the kernels, equations 7.13 and 7.14. The noise in the data for $n > 20$ makes it difficult to explore the scaling of $A(xi, xj)/A(i, j)$ and $F(xi, xj)/F(i, j)$ over even a single order of magnitude of x. We loop through $i < 3$ and $i < j < 6$, for $x < 8$ and plot the average in figures 7.15 b and c. We find, within the limited scope of the experiments, good agreement with the assumption that these kernels scale as power laws, and obtain sensible values for the homogeneity constants of $\lambda = 0.28$ and $\alpha =$ -0.39 for aggregation and fragmentation respectively, which yields a value for the exponent, $y = 0.75$.

The measured value of the homogeneity constant is larger than expected for DLCA (where $\lambda = 0$). We have already observed that motile bacteria can dramatically increase the diffusivity of single particles within this system, as shown in chapter 4. This enhanced diffusivity will impact the aggregation kinetics to some degree, but the positive value for λ suggests that bacteria enhance the aggregation rates of larger clusters more than that of smaller ones. It is unclear if this is the result of enhanced rotational, translational diffusion or a combination of the two.

For fragmentation, the measurement of $\alpha =$ -0.39, indicates that larger clusters fragment slower than smaller ones. To rationalise this, first consider the small cluster size limit, where a cluster can be treated as a circle, the number of bonds

required to break to undergo fragmentation increases with size, thus increasing the difficultly of fragmenting larger clusters.

For the large cluster limit, the fractal nature of the structure means the branch thickness and thus number of bonds required to break a branch does not vary with size. However, large clusters are often interconnected and may require the scission of two or more branches, meaning fragmentation still becomes more difficult as size increases. The continuous increase in difficultly to fragment larger clusters results in a negative value of α.

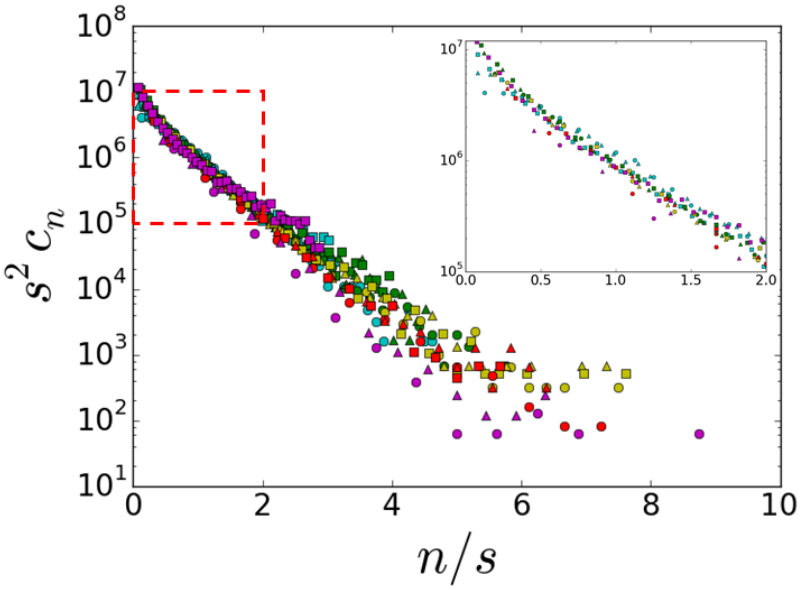

Figure 7.16 Normalised cluster size distributions for samples in steady state. Circles, triangles and squares represent $\phi_p = 0.326$, 0454 and 0.581 respectively and bacterial concentrations 1.7×10^{-4}, 1.7×10^{-4}, 5.7×10^{-3}, 5.7×10^{-3} and 1.7×10^{-2} μm^{-2} are plotted in cyan, green, yellow, red and purple. Data within the red box is enlarged in the inset.

The second assumption made in the derivation is that the cluster size distribution scales, as described by equation 7.10. We observed that both active and passive cluster size distributions scale well in section 7.8, the scaled active cluster size distribution is reproduced again in figure 7.16.

The shape of the normalised cluster size distribution reveals the form of the scaling function, $f(n/s(t))$. The scaling across all samples implies that the underlying processes do not significantly change across our samples. We find the scaling function to be exponential for $n/s(t) > 1$, but as $n/s(t) \to 0$ we note an increase in $s^2 c_n$ away from exponential behaviour. By numerically solving the Smoluchowski

equation, Elminyawi *et al.* also found the same deviation for $\lambda > \alpha$ and further noted that as $\lambda \to \alpha$ the cluster size distribution tends to an exponential, and when $\lambda < \alpha$, the deviation inverts and a plateau in the cluster size distribution is observed for $n/s(t) > 1$ [39]. Note, for the values of a and b (equations 7.17 and 7.18) are truly constant when the cluster size distribution is exponential [153].

We have directly observed that an increase in c_B yields an increase in k_F, and in chapter 4, we observed that diffusion was enhanced by an increase in c_B, which will likely result in an increase in k_A, so it is not clear what the dependence of k_A/k_F is on c_B. With the assumptions of this theory validated experimentally, we can investigate the dependence of c_B on k_A/k_F Equation 7.19 predicts that s_0, the steady-state value of the ratio of the second moment to the first moment of the cluster size distribution, scales with k_A/k_F to an exponent y, where we have determined $y = 0.75$ by measurement of λ and α.

Experimentally, we have observed that we can increase k_A/k_F by decreasing the bacterial concentration c_B. To determine the relationship between k_A/k_F and c_B, we plot s_0 as a function of c_B^{-1}, figure 7.17. We define the scaling for the experimental fitting as $s_0 \propto c_B^{-W}$ to avoid confusion between W and the exponent from the Smoluchowski model, y. We extract values of exponent $W = 0.38$, 0.38 and 0.48 for $\phi_p = 0.326$, 0.454 and 0.581 respectively. We do not study enough separate attraction strengths to know if the increase in the exponent, W, for $\phi_p = 0.581$ is a real effect. The idea that W, or in effect y, may depend on ϕ_p, is not supported by scaled cluster size distributions, figure 7.16, i.e. if y changes, we would not expect to see the observed overlap for all ϕ_p. However, W does change with ϕ_p, but we do not have the results to discuss if λ, α or both are changing. We will proceed by assuming W is constant, and take the mean value of 0.41, suggesting that $s_0 \propto c_B^{-0.41} \propto (k_A/k_F)^{0.75}$, from which we can estimate $(k_A/k_F) \propto c_B^{-0.55}$. The relationship between (k_A/k_F) and c_B is non-trivial, this is because both k_A and k_F depend on c_B. As shown throughout this chapter, the fragmentation rate of clusters increase with bacterial concentration. But within chapter 4, we explored how the diffusivity of discrete passive particles was enhanced by c_B for the same system. Further interpretation of k_A and k_F would require specific models for their dependence on c_B. We conclude that providing $(k_A/k_F) \propto c_B^{-0.55}$, the Smoluchowski theory accurately describes our experiments.

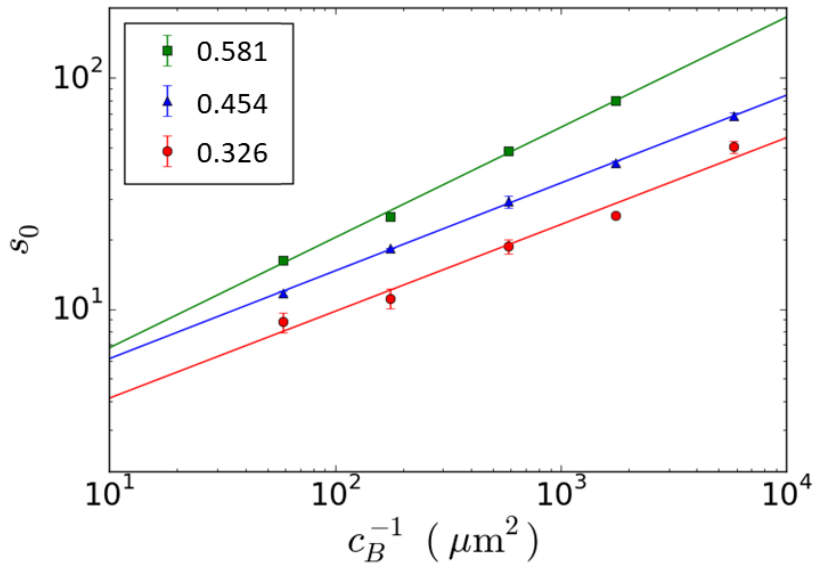

Figure 7.17 Scaling of steady-state cluster size, $s_0 = M_2/M_1$, with bacterial concentration, c_B, over a range of polymer concentration, ϕ_p. The data is replotted from figure 7.7b with fits to equation 7.19. The exponent from fits for ϕ_p 0.326-0.581 are 0.38, 0.38 and 0.48 respectively. Error bars depict standard error across samples.

7.10 In Search on Enhanced Phase Separation

In this chapter so far we have explored how smooth swimming bacteria alter the phase behaviour of a passive colloid-polymer mixture, and we observed a suppression of phase separation. These findings agree with findings from simulations by Omar *et al.*, who also predicts that this behaviour is a sharp function of the active particle's persistence length [97], where for very fast tumbling they observe coarsening of the passive gel structure, instead of cluster breakup. Here we attempt to verify these findings experimentally by altering the persistence length of the bacteria.

To describe the persistence of the swimmers, the swim diffusivity Péclet number is defined as $Pe_R = va/v^2\tau_R = a/l_p$, where v is the particles speed, a is the radius, τ_R is the reorientation time scale and l_p the persistence length. For $Pe_R \leq 1$, Omar *et al.* observed significant coarsening of the passive particle network into large rafts after 100 τ_B, after quenching from a monodisperse system.

To replicate these parameters for the active particle experimental we used AB1157 ΔCheZ, which does not bundle their flagella and thus undergoes constant

tumbling [56]. Unfortunately, we find the use of glucose to extend the swim time also induces bundling of the flagella and loss of their desired constant tumbling behaviour. To match the time limit of the experiment to 100 τ_B = 25 minutes, limits the maximum usable bacterial concentration, due to oxygen depletion of approximately, so we use c_B =$1.7 \times 10^{-2}\,\mu m^{-2}$ or equivalently $\eta_{bac} \sim 0.02$, which is half of that used by Omar *et al.*. For consistency within our own work, we continue to use a particle area fraction, $\eta_c = 0.2$, with is also half of that used by Omar *et al.*. Finally, we matched their attraction strength, well depth $U = 6.5$ k_BT using a polymer concentration, $\phi_p = 0.262$.

Within these scoping experiments, we observed no enhancement of phase separation with the addition of AB1157 ΔCheZ. From observation of the sample, it appears that the bacteria struggle to approach the clusters, and thus would not be able to initiate any particle rearrangements. In the experiments, the unbundled flagella are likely inducing some steric hindrance here and stopping close approach of bacteria and clusters. Therefore the lack of enhanced phase separation may just be a system-specific property.

7.11 Role of Activity at Very High Density

With the experimental system developed within this chapter, it would be remiss to not explore what happens when bacteria are added to dense polycrystalline samples. To date, there have been a few experimental and simulation studies of passive polycrystalline samples doped with active particles of the same size and short persistence length. It has been observed that active particles migrate to the grain boundaries and slowly disturb particle bonds there, which results in the shrinkage of small grains and growth of the large ones eventually resulting in a homogeneous crystal [70, 84, 85].

For our passive system, only a small fraction of the crystal phase is accessible due to the preferential formation of a second layer of particles. For low polymer concentrations, $\phi_p < 0.166$, particle rearrangement occurs within minutes as clusters are not strong enough to hold the weight of the particles on top of them. The quality of the formed monolayer is very sensitive to silica particle density and will never realistically be perfect. A sample with parameters $\phi_p = 0.134$, $\eta_c \approx 0.75$ and $c_B = 1.1 \times 10^{-3}\ \mu m^{-2}$ was prepared and allowed to age for 20 minutes. The sample is observed by bright-field microscopy and a characteristic

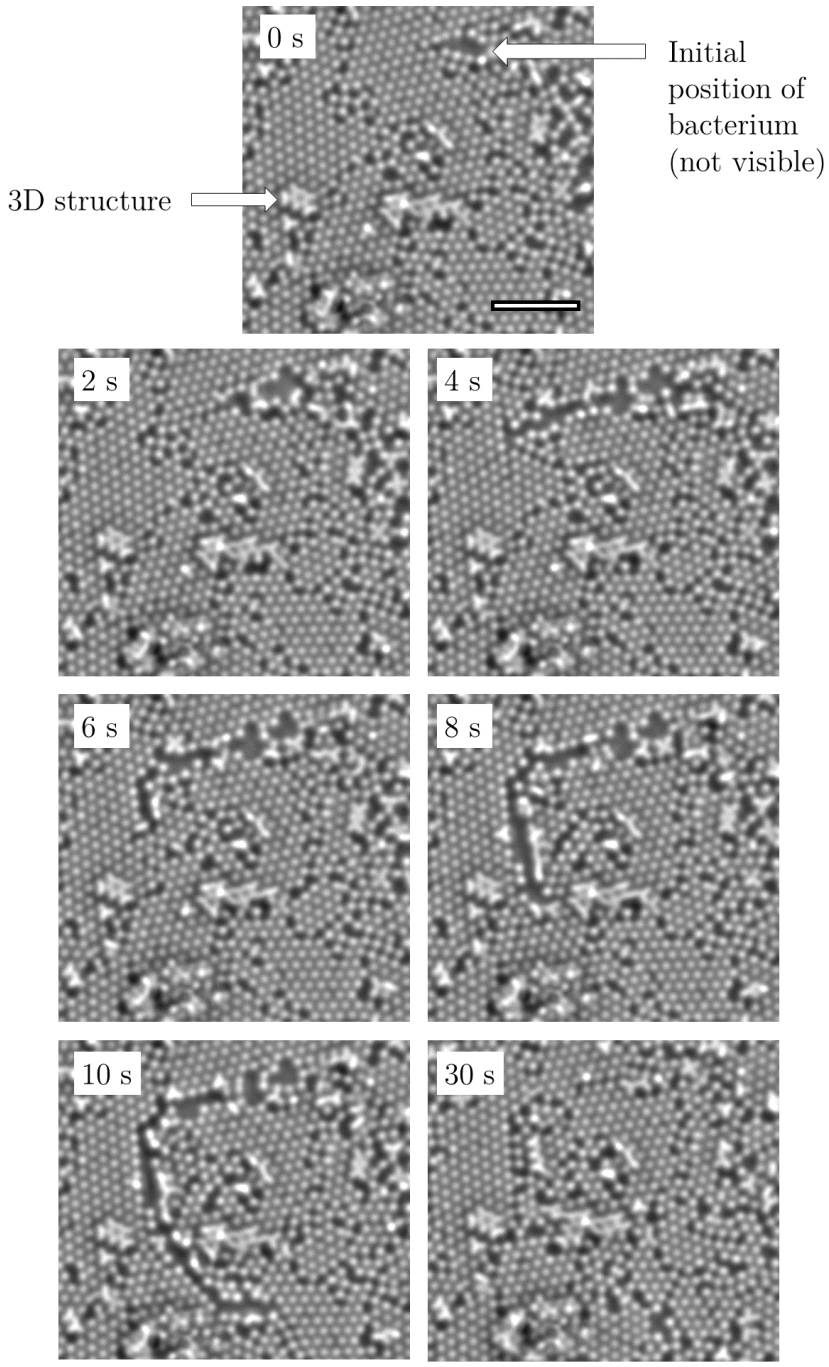

Figure 7.18 Series of cropped micrographs depicting the movement of a bacterium through a polycrystalline sample, at timestamps of 0, 2 ,4, 6, 8, 10 and 30 s. Sample parameters $\phi_p = 0.134$ and $\eta_c \approx 0.75$. The bacterium is not visible due to lensing by neighbouring particles. Scale bar represents 10 μm.

interaction between a bacterium and the polycrystalline particles is detailed in figure 7.18.

As with the experiments at low particle density, the bacteria can enter and leave the surface. In these experiments we are unable to resolve individual bacteria due to lensing effects of neighbouring particles, however, we can infer their positions from videos due to the characteristic jiggling they exert on neighbouring particles. A bacterium initially inserts into the polycrystal towards the top right corner of the micrograph of 7.18, the subsequent images detail the sample position over time. The bacterium takes a second to orientate and then proceeds to swim along a grains unit cell axis, the majority of the colloids in the path are pushed out of the plane and start to form a second layer. When the bacteria reaches a grain boundary it immediately stops and attempts to reorientate, when aligned with one of the new grains unit cell axes it starts moving again until the next grain boundary. This process repeats until the bacterium escapes the surface. Most of the particles displaced by the bacterium's movement return to the surface within a minute, but a scar is left as the particles rarely reform the perfect crystal structure. Over the course of a 30 minute experiment, the average grain size was observed to decrease, but the long term trends in grain size were not studied.

The difference between the observations reported here and that for previous Janus particle studies [70, 84, 85] is the dynamics and shape of the active particle. Work by Brown *et al.* has already compared Janus particle's and *E. coli's* motion through uniform crystalline samples [23], where they also found that *E. coli* swim along unit cell axes, whereas Janus particles orbit a particle and jump stochastically. The reason that *E. coli* swim along the unit cell axes is that steric hindrance of the flagella limits their ability to turn sharply enough to change direction. The bacteria are still able to make sharp turns in our experiment, but only when they move from one grain to another, where they will get momentarily stuck until they can reorient towards a new unit cell axis. Brown *et al.* also noted that bacteria with shorter flagella may find it easier to reorient within the crystal [23], while this may hold true for our samples, our experiments allow for the flagella bundle to be oriented slightly out of the plane which will reduce steric hindrance and may allow for some of the tight reorientations observed.

Simulations of polycrystals compromised of passive particles have found that the added Janus particles will accumulate at grain boundaries and slowly coarsen the crystal domains, removing the grain boundaries [84, 85]. For our experiments with smooth swimming *E. coli*, it appears that the high aspect ratio of the bacteria plus bundled flagella stop the bacteria reorientating easily within the polycrystal, and therefore do not accumulate at grain boundaries and instead swim through

the crystal grains. As *E. coli* swim through the crystals, they can push particles out of the plane, as the particles return to the surface the chance that reform a perfect crystal again appears low, and instead favour the formation of new grain boundaries. Further study on these samples is warranted to measure the average crystal grain size over time, to more carefully detail the effects of smooth swimming *E. coli* of these samples.

7.12 Conclusion

In this chapter, we developed a model two-dimensional system comprising of silica particles, polymer depletion induced attractions, which we dope with smooth swimming *E. coli*. At sufficiently high attraction strength, the particles phase separate in to gel-like polycrystals that undergo constant aggregation. Smooth swimming bacteria within such mixtures act to sterically break the clusters apart by swimming through them, primarily along a crystal grain's unit cell axis. The passive aggregation and counter-acting active breakup results in microphase separation, where the mean cluster size increases with increasing attraction strength and decreasing bacterial concentration. In this description, we can consider the bacteria to induce a repulsion between the particles. This system presents an unusual method to achieve microphase separation due to the temporal and spatial heterogeneity of the effective repulsion.

The choice to develop this 2D system on a glass surface has had advantages and disadvantages over more common methods for studying Brownian particles in 2D, e.g. a soap film. One of the main advantages is the in-depth understanding of how *E. coli* behave in such an environment, which removes any confusion as to how they might interact with silica particles. A second being the removal of all turbulent airflow, removing any inconsistent or anomalous diffusion behaviour. However, the adhesion of particles and bacteria to the surface introduced errors in to the aggregation behaviour of the particles, for which we were unable to account for. The quenching method, where all the particles needed to sediment to the surface to start aggregation, also introduced problems due to some particles becoming stuck on a second layer, causing tracking problems. The formation of a double layer could be easily minimised in future work by the use of less buoyant particles.

We reviewed the phase transition of the system in detail. Within the fluid

region, we expected that activity-induced passive-passive attractions may enhance clustering [3], however, there was little evidence to support enhanced clustering at low attraction strength and there was no scaling with bacterial concentration.

On the other hand, studies of purely active systems with attractions have found that activity suppresses phase separation [112, 122, 143]. Surprisingly, we found no suppression of phase separation either, i.e. the phase boundary shows no significant change with activity. We understand this behaviour is due to the phase transition being dominated by passive-passive interactions, as the active-passive interactions are heterogeneous, meaning that activity cannot effectively stop on the initial onset of phase separation and thus the transition has activity dependence.

An unexpected negative result was that bacterial concentration does not significantly alter the initial aggregation rate. Due to the enhanced diffusion of passive particles in an active bath we might expect to observe an increase in initial aggregation rate, while the cluster sizes are small and breakup events are negligible, however, we observed no change.

Our findings that active particles with strong swimming speeds and long persistence lengths can break apart clusters compromised of attractive passive particles has been replicated by recent simulations by Omar *et al.* [97]. The agreement between our initial findings inspired us to investigate whether we could find experimental evidence for activity-induced coarsening of the crystalline clusters. We were not able to coarsen our samples with constantly tumbling bacteria, however, this may have been due to the bacteria's flagella hindering their ability to approach clusters.

The Smoluchowski aggregation-fragmentation model provided a framework to study the underlying processes causing microphase separation with the system. The model allows for the separation of aggregation and fragmentation rates within the system. Both are found to increase with bacterial concentration, but favouring fragmentation. Further study of this model and its application to experimental systems would aid in the development of designer phase behaviour.

We can compare this microphase-separated behaviour to that of non-driven systems by recognising that the act of bacteria breaking up clusters resembles a repulsive force. Studies of colloidal mixtures with short-ranged attraction and long-ranged repulsion (SALR) are known to also form microphase-separated states at low densities. Interestingly, as density increases in SALR systems, gels

can form [119]. Therefore, one would expect that at higher densities our system of attractive particles with activity-induced repulsions would also form a gel. Such a gel would likely be living, undergoing constant aggregation and scission, much like what is observed for purely active gel systems [112, 143].

In summary, the new experimental system developed and studied within this chapter is completely different to any published experimental work and only very recent simulations have started to examine a similar system [97]. This work highlights new experimental methods for controlling passive matter with small concentrations of active particles.

Chapter 8

Future Work

In this chapter, we will introduce a new system containing bacteria (without added passive particles), which we developed here, but requires further study. We combine two separate works from here at the University of Edinburgh. Firstly, the depletion forces required to induce phase separation in mixtures of *E. coli* increase when activity is introduced [121, 122, 124]. Secondly, the development of a strain of *E. coli*, AD10, whose motility can be induced by green light (in the absence of any other source of inducing motility, such as oxygen or glucose) [5] and further how spatially and temporal variations in light intensity can be used to control local density [61, 67]. We will show how the careful combination of AD10 and polymer depletants allows for spatial and temporal control of the systems phase behaviour and begin to explore the designer structures possible with this system.

In this chapter, we use a custom optical setup which that developed by J. Arlt. This work was further inspired by unpublished work by A. Brown on the sedimentation of AD10 gels.

8.1 Optical Setup

To perform the necessary experiments on AD10, the setup needs to be able to image the entire field of view while inducing swimming within sub-regions. We utilise red light to image the sample, which does not induce swimming [5] and we then illuminate the sample, from a second source, with a spatially modulated

green light.

The setup revolves around the integration of a digital micromirror device (DMD) into the optical axis of an inverted microscope. The DMD (DLP6500, Texas Instruments) is a 1920×1080 array of micromirrors, where each mirror can be individually switched between an angle of 12° and -12°, used to reflect light towards or away from a desired target. The DMD can be programmed to reflect spatially and temporally evolving patterns.

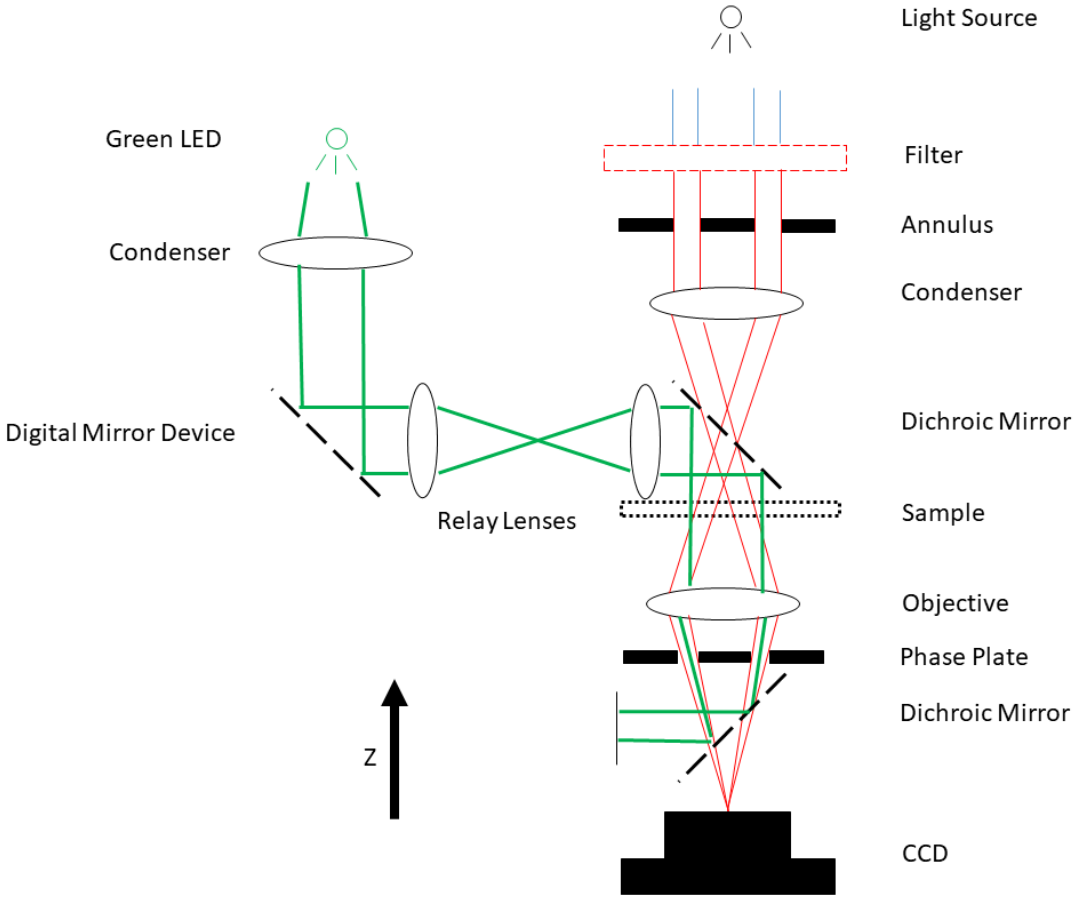

Figure 8.1 Schematic diagram showing the phase contrast imaging in red light with a digital mirror device in tandem.

A diagram detailing the integration of the DMD with an inverted phase-contrast microscope (Nikon TE2000) is depicted in figure 8.1. A red filter (RG360 Schott Glass) is placed in front of the microscope's light source, ensuring the light used for imaging the sample does not activate the proteorhodopsin in AD10 and induce swimming. The red light is passed through a Ph1 phase ring, focused onto the sample and through a 10×/0.3 NA Ph1 objective before being captured by a CMOS MC1462 Mikrotron camera. A LED filtered to green wavelengths 510-

560nm is used to illuminate the DMD, which depending on mirror orientation, either deflects the light away from the microscope or transmits it to the first dichroic mirror through relay optics, positioned above the sample. The relay optics demagnify the image from the DMD and project it on to the sample. The projected image can be up to ~ 5 mm circle, significantly larger the field of view, $1.5 \times 1.5\ mm^2$. The image from the DMD is collected by the objective but deflected away from the camera by an epi-fluorescence filter cube (Nikon G-2A).

The DMD can apply a wide range of 2D images onto the sample, here we will report on a single static image which has a series of illuminated rectangles of width ranging 25 to 225 μm spaced by 50 μm, figure 8.2. The pattern shown has been cropped to correspond to microscope images. Here, by increasing the size of the illuminated region, we increase the number of bacteria collected in the dark region, increasing the cell density strengthening the gel structure formed [167].

8.2 Spatially Controlled Phase Behaviour

Here we report on a sample with a carefully chosen polymer concentration, sufficient to induce aggregation between non-motile cells but not swimmers. This activity dependant phase behaviour has already been thoroughly reviewed by Schwarz-Linek *et al.* [121, 122, 124]. This is then combined with the light-induced activity of AD10 to make a sample whose phase behaviour can be controlled locally by illumination.

Figure 8.3 depicts a sample containing $c_B = 6.0 \times 10^9$ mL^{-1} and $\phi_p = 0.57$ (PSS, $r_g = 45$ nm) in motility buffer, sealed in a 100 μm high capillary.

To induce light activation, we allow the bacteria to exhaust the oxygen supply, by leaving the sealed sample for 30 minutes, leaving the sample without any fuel present. After oxygen depletion, activity is induced by illumination with green light. For an initially uniform sample, the lines pattern is projected for 5 minutes and the sample is continuously imaged for a further 1000 minutes, figure 8.3. The bacteria quickly swim out of the illuminated regions and aggregate in the dark, while non-motile cells remain with the illuminated region. After the pattern is switched off, we observe no significant motion of the bacteria aggregates.

Without the polymer present, this structure retention does not occur [5], instead the structure decays due to the diffusion of the bacteria. While not shown (due to

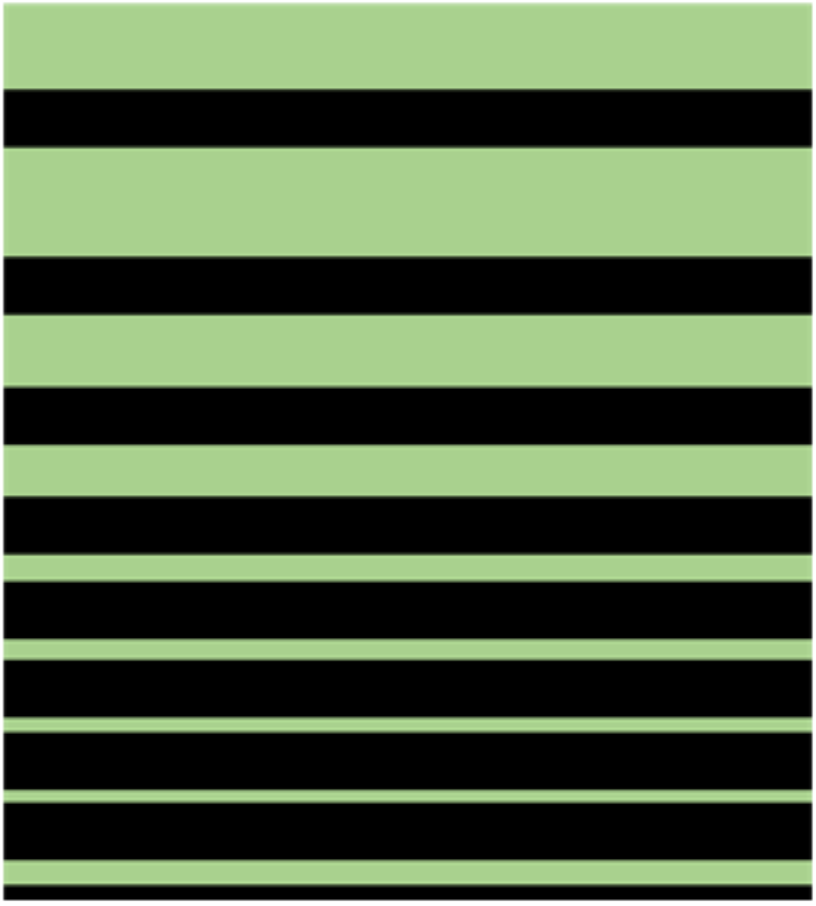

Figure 8.2 The image applied to the sample by the digital mirror device comprising of a series of dark bars of width $\sim$ 50 μm spaced by a range of illuminated bars of widths ranging from 25 to 225 μm, where the entire image is 1.10 $\times$ 0.93 mm^2. The patterns shown correspond to the field of view.

a lack of images), our long-lasting structures can be broken down by illumination of a large region surrounding them. Note, due to the limitation of diffusion in this system, to re-create a perfectly uniform structure the entire sample must be illuminated, so no dark-light boundary is present for accumulation to occur at.

8.3 Further Development

We have shown that spatial control of the phase behaviour is possible for light-activated bacteria at depletant concentrations which induce aggregation between non-swimmers but not swimmers. We did not review the composition of the sample in detail and there likely remains room for optimisation. A question

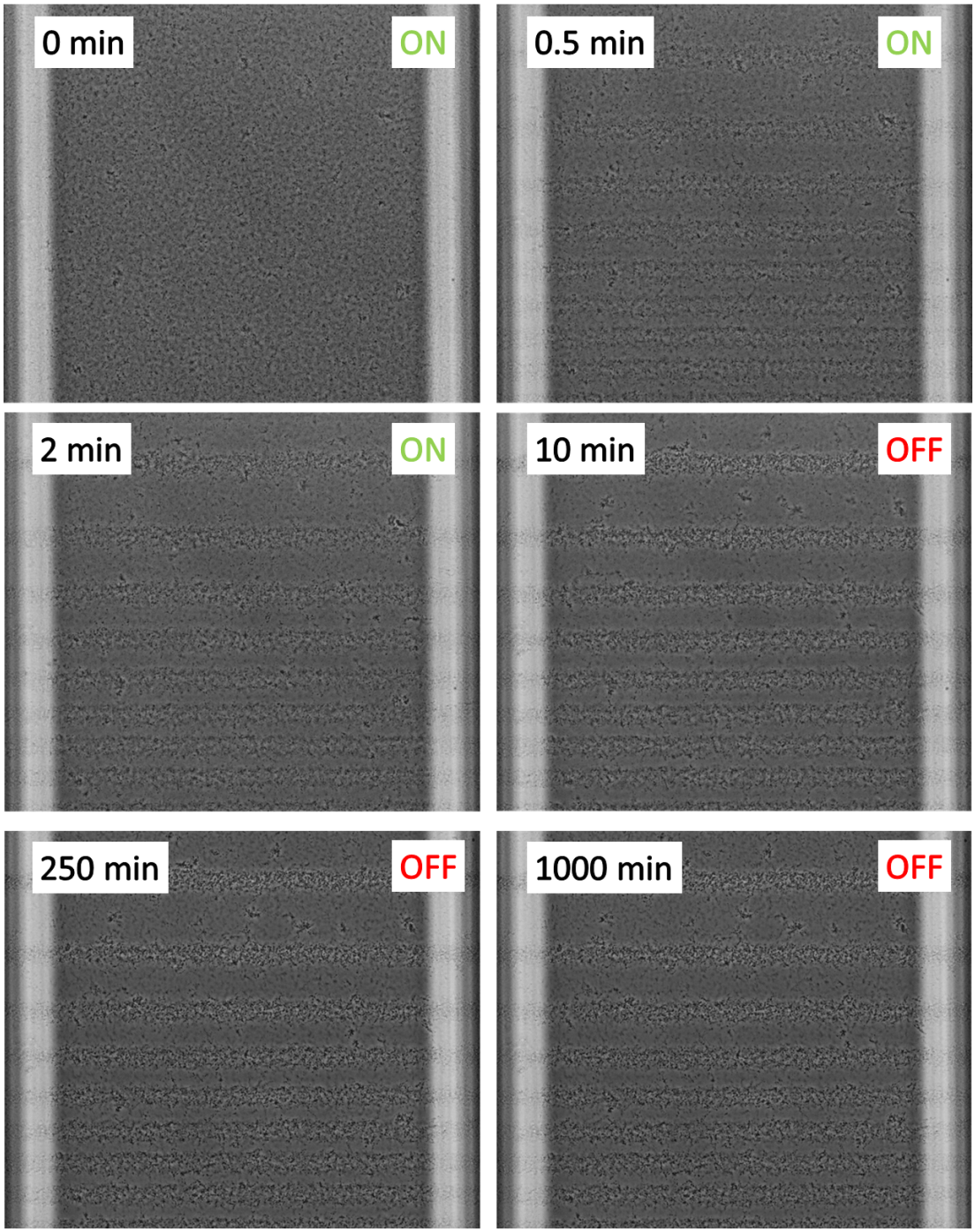

Figure 8.3 Micrographs showing the time evolution of a representative sample with polymer depletant. The sample is illuminated with the lines pattern for 5 minutes, it is then switched off and while imaging continues up to 1000 minutes. The sample is composed of $c_B = 6.0 \times 10^9$ mL^{-1} and $c_p = 0.25$ %wt (PSS, $r_g = 45$ nm) in phosphate buffer. The sample is sealed in a 100 μm high capillary and imaged at the bottom surface.

remains, is this spatial control still possible when you dope increasing levels of passive colloids into the sample?

A possible extension of our work would be to create three-dimensional structures. To create such structures, the optics would have to be redeveloped to allow three-dimensional patterns. Clever use of optics may yield cones or square-based pyramids, however, more complex structures will require the use of holographic projections. To create three-dimensional structures, one will need to work around the sedimentation of the structure. There exists several tried and tested methods for limiting sedimentation of colloidal gels which may help here, including strengthening the gel by increasing bacteria concentration, attraction strength or by reducing stress on the structure by density matching the solvent and bacteria [8, 167]

Another possible development for this system is to use the designer structure as a template for a silica structure. Based on the experiments that use *E. coli* as scaffolding for colloidal spherocylinders made of silica using the Stöber process [93], long silanization processes will yield blocks of silica around the templated *E. coli* structures. This is not a trivial reaction to apply here as water is the initiator in the Stöber process and therefore the dispersion medium needs to be exchanged to another media, generally ethanol. We propose that to successfully exchange the medium, the bacteria should first be covalently cross-linked either directly or by attaching a cross-linking agent to the polymer depletant. The development of such designer silica structures may be of use in the creation of microchips.

Further, work by A. Brown on AD10 depletion induced gels, suggests that at high attraction strength, where swimmers can no longer escape the depletion well, activity can agitate the gel and cause enhanced sedimentation. Systematic studies of enhanced sedimentation have not yet been completed and the underlying process remains unconfirmed.

Chapter 9

Concluding Remarks

9.1 Conclusion

In this thesis, we report on experiments that used polymer depletion to alter interactions between motile *E. coli* and passive colloids. By adding active-passive attractions we observe a dramatic change behaviour which further increases the wide array of non-equilibrium behaviour accessible to active systems.

In chapters 4 and 5 we measured how the activity enhanced diffusion of passive particles is altered by depletion attractions. The main conclusion from this work is that, for *E. coli*, short-ranged attraction increases diffusion enhancement in quasi-two-dimensions, but this effect is significantly diminished in three-dimensions. Strong depletion forces allow passive tracers to stick onto passing swimmers which allow for diffusion enhancement beyond that of hydrodynamic interactions. These sticky interactions are observed in both two and three-dimensions by the presence of large jumps in the otherwise diffusive movement of the passive tracer. The frequency of these interactions and subsequent diffusion enhancement is dependant on the dimensionality. Currently, we assume that close range interactions are more frequent in quasi-two-dimensions due to the presence of a surface, where the surface suppresses the long-range hydrodynamic flows induced by swimming allowing for particles to get closer to an approaching swimmer.

In chapter 7 we observed how the phase behaviour of passive particles with depletion attractions changed when doped with motile *E. coli*. We found that activity limited the degree of phase separation, known as microphase separation,

where the size of the polycrystalline clusters was found to depend on the attraction strength and the *E. coli* surface density. Surprisingly, we noted that activity did not significantly alter the short-time aggregation kinetics. We also showed that our findings are well characterised by the Smoluchowski aggregation-fragmentation model

Finally, in chapter 8, we built upon recent advances in controlling the spatial distribution and phase behaviour of *E. coli* to show that we can spatially control phase behaviour and use this to build gel-like structures that last at least several hours without signs of decay. This behaviour requires careful control of attraction strength, where the aim is to induce aggregation in non-motile cells while allowing the motile cells to swim free.

9.2 Outlook

For our work on diffusion enhancement (chapters 4 and 5), further work will likely require the use of simulations. Using simulations would allow for the interactions between passive and active particles to be more extensively tuned and which may produce further support for the sticking mechanism further increasing enhanced diffusion. Further, simulations would allow hydrodynamics to be switched on and off, which would allow testing of our current understanding, that hydrodynamic interactions control the frequency of sticking interactions.

For our work on micro-phase separation (chapter 7), again simulations would be very helpful in extending the experimental findings. It would be of particular interest to use simulations to further explore aggregation-fragmentation dynamics. Due to the limited scope of our current experiment results, the aggregation and fragmentation homogeneity constants, λ and α, have only been measured for one sample over small changes in cluster size. Simulations can help validate if aggregation and fragmentation homogeneity constants hold for larger clusters, i.e. review $A(xi, xj)/A(i, j) = x^{\lambda}$ and $F(xi, xj)/F(i, j) = x^{\alpha}$ for $x \rightarrow 100$. Also, simulations can be used to test whether the homogeneity constants vary with system parameters like c_B or ϕ_p.

Experimentally, now that we have a good understanding of the phase behaviour active-passive mixtures with attractions, it follows to review this behaviour in three-dimensions. For our current system, while possible to directly observe

samples by confocal microscopy, these measurements would be limited by the difficulty in index-matching the solvent, while retaining an environment that promotes motility in *E. coli*. Alternatively, the system could be studied by rheology, where the mechanical difference between gels and microphase separated states can be measured directly.

Appendix A

Changing in Motility with Buffer Strengths

E. coli is perhaps the most studied active colloid [123] and yet in the completion of this work we identified some unexpected responses of *E. coli* to the presence of salt. Here we will present a couple of results, the explanation for which will be due to complex biophysics out of the scope of the work presented in this thesis.

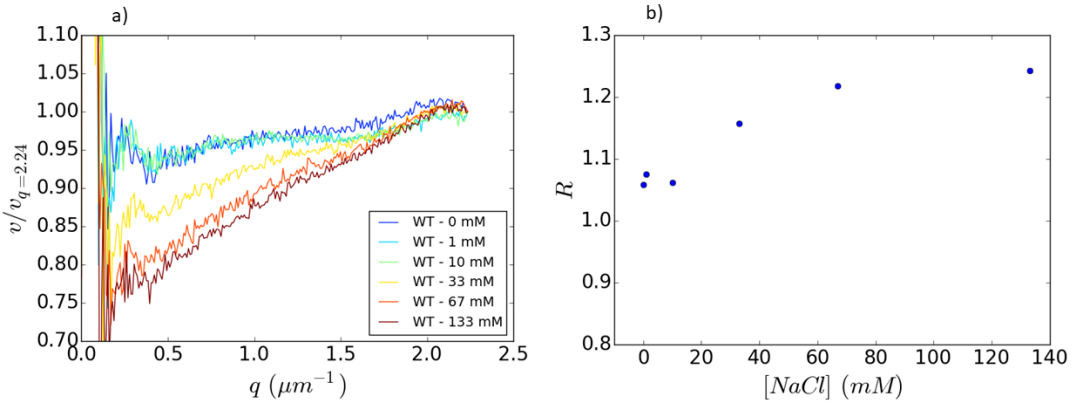

Figure A.1 The full set of results, initially presented in figure 5.6. The effect of salt concentration on the tumbling rates of AB1157 WT as inferred by the q dependence of the velocity from DDM.

The first set of results is an expansion of the results presented in chapter 5.4. We studied the tumbling rates of WT *E. coli* in motility buffer with varying concentrations of NaCl, by observing the q dependence of the speed as measured by DDM. As a populations tumbling rate increases, it takes longer for a cell to

swim long length scales i.e. low q, meaning that as tumbling rate increases the low-q velocity decreases. The relative tumbling rate can be quantified by

$$R = v(q = 2.24\mu\text{m}^{-1})/v(q = 0.5\mu\text{m}^{-1}) \tag{A.1}$$

As NaCl increases, we observe an increase in tumbling rate, shown in figure A.1. It is standard to use [NaCl]= 67 mM [123]. To the author's best knowledge, the first use of NaCl in the buffer appears within the seminal work of Berg where tumbling rates were initially measured by single cell tracking [12], so it is unlikely that these findings are new to Biologists.

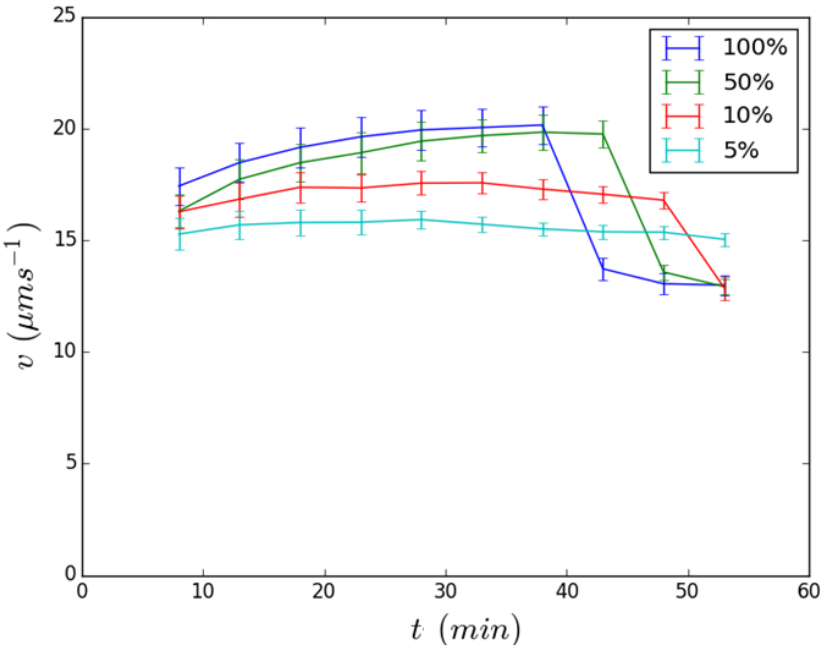

Figure A.2 DDM measurements of the velocity of smooth swimming *E. coli* as buffer strength is decreased.

The second set of results observes how salt concentration changes oxygen consumption. When a carbon fuel source is present in abundance, here glucose, in a sealed environment, *E. coli* consume all oxygen before depleting the carbon source. As oxygen concentration drops, *E. coli* is observed to increase swimming speed, which then quickly drops to a plateau value after oxygen depletion [123].

We tested how buffer strength effected the velocity of *E. coli* over time. Here, we refer to a relative buffer strength, where 100 % refers to our standard motility buffer of 6.2 mM K_2HPO_4, 3.8 mM KH_2PO_4, 0.1 mM EDTA at pH $\sim$ 7.5 and 0

% is deionised water. We use a stock of AB1157 ΔCheY, $c_B = 10^8$ mL^{-1} with an excessive glucose concentration of 3 mM and report the average velocity over time as measured by DDM, figure A.2. The measurements were performed in parallel on the same batch of cells.

We find that as the buffer is weakened the velocity peak is lowered and shifted to longer times. The shifting of velocity drop indicates that oxygen consumption slows as the buffer strength decreases. These initial results also suggest that after oxygen depletion, the buffer strength does not change the swimming velocity.

Bibliography

[1] Adler, J. "Chemotaxis in bacteria." *Science* 153, 3737: (1966) 708–716.

[2] Adler, J., and B. Templeton. "The effect of environmental conditions on the motility of Escherichia coli." *Microbiology* 46, 2: (1967) 175–184.

[3] Angelani, L., C. Maggi, M. L. Bernardini, A. Rizzo, and R. Di Leonardo. "Effective Interactions between Colloidal Particles Suspended in a Bath of Swimming Cells." *Phys. Rev. Lett.* 107: (2011) 138,302.

[4] Angelani, L., R. Di Leonardo, and G. Ruocco. "Self-starting micromotors in a bacterial bath." *Physical review letters* 102, 4: (2009) 048,104.

[5] Arlt, J., V. A. Martinez, A. Dawson, T. Pilizota, and W. C. Poon. "Painting with light-powered bacteria." *Nature communications* 9, 1: (2018) 768.

[6] Asakura, S., and F. Oosawa. "Interaction between particles suspended in solutions of macromolecules." *Journal of Polymer Science* 33, 126: (1958) 183–192.

[7] ———. "Interaction between particles suspended in solutions of macromolecules." *Journal of Polymer Science* 33, 126: (1958) 183–192.

[8] Bartlett, P., L. J. Teece, and M. A. Faers. "Sudden collapse of a colloidal gel." *Physical Review E* 85, 2: (2012) 021,404.

[9] Bates, F. S. "Polymer-polymer phase behavior." *Science* 251, 4996: (1991) 898–905.

[10] Bechinger, C., R. Di Leonardo, H. Löwen, C. Reichhardt, G. Volpe, and G. Volpe. "Active particles in complex and crowded environments." *Rev. Mod. Phys.* 88: (2016) 045,006.

[11] Belloni, L. "Colloidal interactions." *Journal of Physics: Condensed Matter* 12, 46: (2000) R549.

[12] Berg, H. C., D. A. Brown, et al. "Chemotaxis in Escherichia coli analysed by three-dimensional tracking." *Nature* 239, 5374: (1972) 500–504.

[13] Berne, B. J., and R. Pecora. *Dynamic light scattering: with applications to chemistry, biology, and physics*. Courier Corporation, 2000.

[14] Bertoin, J. "Eternal Solutions to Smoluchowski's Coagulation Equation with Additive Kernel and Their Probabilistic Interpretations." *The Annals of Applied Probability* 12, 2: (2002) 547–564.

[15] Biben, T., and J.-P. Hansen. "Phase separation of asymmetric binary hard-sphere fluids." *Physical review letters* 66, 17: (1991) 2215.

[16] van Blaaderen, A. "Imaging individual particles in concentrated colloidal dispersions by confocal scanning light microscopy." *Advanced Materials* 5, 1: (1993) 52–54.

[17] Blake, J., and A. Chwang. "Fundamental singularities of viscous flow." *Journal of Engineering Mathematics* 8, 1: (1974) 23–29.

[18] Brader, J., M. Dijkstra, and R. Evans. "Inhomogeneous model colloid-polymer mixtures: Adsorption at a hard wall." *Physical Review E* 63, 4: (2001) 041,405.

[19] Brodin, A., A. Nych, U. Ognysta, B. Lev, V. Nazarenko, M. Škarabot, and I. Muševič. "Melting of 2D liquid crystal colloidal structure." *Condensed Matter Physics* 13: (2010) 33,601.

[20] Brooks, A. M., M. Tasinkevych, S. Sabrina, D. Velegol, A. Sen, and K. J. Bishop. "Shape-directed rotation of homogeneous micromotors via catalytic self-electrophoresis." *Nature communications* 10, 1: (2019) 1–9.

[21] Brown, A., and W. Poon. "Ionic effects in self-propelled Pt-coated Janus swimmers." *Soft matter* 10, 22: (2014) 4016–4027.

[22] Brown, A. T., W. C. Poon, C. Holm, and J. de Graaf. "Ionic screening and dissociation are crucial for understanding chemical self-propulsion in polar solvents." *Soft Matter* 13, 6: (2017) 1200–1222.

[23] Brown, A. T., I. D. Vladescu, A. Dawson, T. Vissers, J. Schwarz-Linek, J. S. Lintuvuori, and W. C. K. Poon. "Swimming in a crystal." *Soft Matter* 12: (2016) 131–140.

[24] Buttinoni, I., . J. Bialke, . F. Kummel, . H. Lowen, . C. Bechinger, , and T. Speck. "Dynamical clustering and phase separation in suspensions of self-propelled colloidal particles." *Phys. Rev. Lett.* 110: (2013) 238,301.

[25] Cates, M. E., and J. Tailleur. "Motility-Induced Phase Separation." *Annual Review of Condensed Matter Physics* 6, 1: (2015) 219–244.

[26] Cheezum, M. K., W. F. Walker, and W. H. Guilford. "Quantitative comparison of algorithms for tracking single fluorescent particles." *Biophysical journal* 81, 4: (2001) 2378–2388.

[27] Chen, X., X. Yang, M. Yang, and H. Zhang. "Dynamic clustering in suspension of motile bacteria." *EPL (Europhysics Letters)* 111, 5: (2015) 54,002.

[28] Chenouard, N., I. Smal, F. De Chaumont, M. Maška, I. F. Sbalzarini, Y. Gong, J. Cardinale, C. Carthel, S. Coraluppi, M. Winter, et al. "Objective comparison of particle tracking methods." *Nature methods* 11, 3: (2014) 281.

[29] Cheung, C., Y. Hwang, X. Wu, and H. Choi. "Diffusion of particles in free-standing liquid films." *Physical review letters* 76, 14: (1996) 2531.

[30] Czirók, A., H. E. Stanley, and T. Vicsek. "Spontaneously ordered motion of self-propelled particles." *Journal of Physics A: Mathematical and General* 30, 5: (1997) 1375.

[31] Das, M., C. F. Schmidt, and M. Murrell. "Introduction to Active Matter." *Soft Matter* 16, 31: (2020) 7185–7190.

[32] Deaconu, M., and E. Tanré. "Smoluchowski's coagulation equation: probabilistic interpretation of solutions for constant, additive and multiplicative kernels." *Annali della Scuola Normale Superiore di Pisa-Classe di Scienze* 29, 3: (2000) 549–579.

[33] Dijkstra, M., and R. van Roij. "Entropic wetting and many-body induced layering in a model colloid-polymer mixture." *Physical review letters* 89, 20: (2002) 208,303.

[34] Dinsmore, A., P. Warren, W. Poon, and A. Yodh. "Fluid-solid transitions on walls in binary hard-sphere mixtures." *EPL (Europhysics Letters)* 40, 3: (1997) 337.

[35] Dinsmore, A., A. Yodh, and D. Pine. "Phase diagrams of nearly-hard-sphere binary colloids." *Physical review E* 52, 4: (1995) 4045.

[36] Doostmohammadi, A., J. Ignés-Mullol, J. M. Yeomans, and F. Sagués. "Active nematics." *Nature communications* 9, 1: (2018) 1–13.

[37] Drescher, K., J. Dunkel, L. H. Cisneros, S. Ganguly, and R. E. Goldstein. "Fluid dynamics and noise in bacterial cell–cell and cell–surface scattering." *Proceedings of the National Academy of Sciences* 108, 27: (2011) 10,940–10,945.

[38] Dunkel, J., V. B. Putz, I. M. Zaid, and J. M. Yeomans. "Swimmer-tracer scattering at low Reynolds number." *Soft Matter* 6, 17: (2010) 4268–4276.

[39] Elminyawi, I. M., S. Gangopadhyay, and C. Sorensen. "Numerical solutions to the Smoluchowski aggregation—fragmentation equation." *Journal of colloid and interface science* 144, 2: (1991) 315–323.

[40] Family, F., and D. P. Landau. *Kinetics of aggregation and gelation*. Elsevier, 2012.

[41] Family, F., P. Meakin, and J. M. Deutch. "Kinetics of coagulation with fragmentation: scaling behavior and fluctuations." *Physical review letters* 57, 6: (1986) 727.

[42] Feitosa, M. I. M., and O. N. Mesquita. "Wall-drag effect on diffusion of colloidal particles near surfaces: A photon correlation study." *Phys. Rev. A* 44: (1991) 6677–6685.

[43] Fily, Y., and M. C. Marchetti. "Athermal phase separation of self-propelled particles with no alignment." *Physical review letters* 108, 23: (2012) 235,702.

[44] Fry, D., T. Sintes, A. Chakrabarti, and C. Sorensen. "Enhanced kinetics and free-volume universality in dense aggregating systems." *Physical review letters* 89, 14: (2002) 148,301.

[45] Fu, X., L.-H. Tang, C. Liu, J.-D. Huang, T. Hwa, and P. Lenz. "Stripe formation in bacterial systems with density-suppressed motility." *Physical review letters* 108, 19: (2012) 198,102.

[46] Galajda, P., J. Keymer, P. Chaikin, and R. Austin. "A wall of funnels concentrates swimming bacteria." *Journal of bacteriology* 189, 23: (2007) 8704–8707.

[47] Ginot, F., I. Theurkauff, F. Detcheverry, C. Ybert, and C. Cottin-Bizonne. "Aggregation-fragmentation and individual dynamics of active clusters." *Nature communications* 9, 1: (2018) 1–9.

[48] Goldman, A. J., R. G. Cox, and H. Brenner. "Slow viscous motion of a sphere parallel to a plane wall—I Motion through a quiescent fluid." *Chemical engineering science* 22, 4: (1967) 637–651.

[49] Gompper, G., R. G. Winkler, T. Speck, A. Solon, C. Nardini, F. Peruani, H. Löwen, R. Golestanian, U. B. Kaupp, L. Alvarez, et al. "The 2020 motile active matter roadmap." *Journal of Physics: Condensed Matter* 32, 19: (2020) 193,001.

[50] González, A. E., F. Martínez-López, A. Moncho-Jordá, and R. Hidalgo-Álvarez. "Two-Dimensional Colloidal Aggregation: Concentration Effects." *Journal of Colloid and Interface Science* 246, 2: (2002) 227–234.

[51] Graessley, W. W. "Polymer chain dimensions and the dependence of viscoelastic properties on concentration, molecular weight and solvent power." *Polymer* 21, 3: (1980) 258–262.

[52] Grégoire, G., H. Chaté, and Y. Tu. "Active and passive particles: Modeling beads in a bacterial bath." *Physical Review E* 64, 1: (2001) 011,902.

[53] Harder, J., S. Mallory, C. Tung, C. Valeriani, and A. Cacciuto. "The role of particle shape in active depletion." *The Journal of chemical physics* 141, 19: (2014) 194,901.

[54] Helgesen, G., A. Skjeltorp, P. M. Mors, R. Botet, and R. Jullien. "Aggregation of magnetic microspheres: experiments and simulations." *Physical review letters* 61, 15: (1988) 1736.

[55] de Hoog, E. H., W. K. Kegel, A. van Blaaderen, and H. N. Lekkerkerker. "Direct observation of crystallization and aggregation in a phase-separating colloid-polymer suspension." *Physical Review E* 64, 2: (2001) 021,407.

[56] Huang, C., and R. C. Stewart. "CheZ mutants with enhanced ability to dephosphorylate CheY, the response regulator in bacterial chemotaxis." *Biochimica et Biophysica Acta (BBA)-Protein Structure and Molecular Enzymology* 1202, 2: (1993) 297–304.

[57] Huang, Z., P. Chen, G. Zhu, Y. Yang, Z. Xu, and L.-T. Yan. "Bacteria-Activated Janus Particles Driven by Chemotaxis." *ACS nano* 12, 7: (2018) 6725–6733.

[58] Jeanneret, R., D. O. Pushkin, V. Kantsler, and M. Polin. "Entrainment dominates the interaction of microalgae with micron-sized objects." *Nature communications* 7: (2016) 12,518.

[59] Jepson, A., V. A. Martinez, J. Schwarz-Linek, A. Morozov, and W. C. Poon. "Enhanced diffusion of nonswimmers in a three-dimensional bath of motile bacteria." *Physical Review E* 88, 4: (2013) 041,002.

[60] Jepson, A. K. "E coli motility and growth: a biophysical study." PhD thesis, University of Edinburgh, 2014.

[61] Jochen, A., M. V. A. Dawson, T. Pilizota, and W. Poon. "Dynamics-dependent density distribution in active suspensions." *Nature communications* 10, 1: (2019) 2321.

[62] Kaplan, P., J. Rouke, A. Yodh, and D. Pine. "Entropically driven surface phase separation in binary colloidal mixtures." *Physical Review Letters* 72, 4: (1994) 582.

[63] Kasyap, T., D. L. Koch, and M. Wu. "Hydrodynamic tracer diffusion in suspensions of swimming bacteria." *Physics of Fluids* 26, 8: (2014) 081,901.

[64] Kirkegaard, J. B., A. O. Marron, and R. E. Goldstein. "Motility of colonial choanoflagellates and the statistics of aggregate random walkers." *Physical review letters* 116, 3: (2016) 038,102.

[65] Kose, A., and S. Hachisu. "Ordered structure in weakly flocculated monodisperse latex." *Journal of Colloid and Interface Science* 55, 3: (1976) 487–498.

[66] Koumakis, N., A. Lepore, C. Maggi, and R. Di Leonardo. "Targeted delivery of colloids by swimming bacteria." *Nature communications* 4: (2013) 2588.

[67] Koumakis, N., A. T. Brown, J. Arlt, S. E. Griffiths, V. A. Martinez, and W. C. Poon. "Dynamic optical rectification and delivery of active particles." *Soft matter* 15, 35: (2019) 7026–7032.

[68] Kramers, H. A. "Brownian motion in a field of force and the diffusion model of chemical reactions." *Physica* 7, 4: (1940) 284–304.

[69] Kruger, S., H.-J. Mogel, M. Wahab, and P. Schiller. "Depletion force between anisometric colloidal particles." *Langmuir* 27, 2: (2011) 646–650.

[70] Kummel, F., P. Shabestari, C. Lozano, G. Volpe, and C. Bechinger. "Formation, compression and surface melting of colloidal clusters by active particles." *Soft Matter* 11: (2015) 6187–6191.

[71] Lekkerkerker, H. N., and R. Tuinier. *Depletion interaction*. Springer, 2011.

[72] Leptos, K. C., J. S. Guasto, J. P. Gollub, A. I. Pesci, and R. E. Goldstein. "Dynamics of Enhanced Tracer Diffusion in Suspensions of Swimming Eukaryotic Microorganisms." *Physical Review Letters* 103, 19.

[73] Li, T., and M. G. Raizen. "Brownian motion at short time scales." *Annalen der Physik* 525, 4: (2013) 281–295.

[74] Liebchen, B., and H. Löwen. "Which interactions dominate in active colloids?" *The Journal of chemical physics* 150, 6: (2019) 061,102.

[75] Liebchen, B., D. Marenduzzo, and M. E. Cates. "Phoretic interactions generically induce dynamic clusters and wave patterns in active colloids." *Physical review letters* 118, 26: (2017) 268,001.

[76] Lin, M., H. Lindsay, D. Weitz, R. Ball, R. Klein, and P. Meakin. "Universality in colloid aggregation." *Nature* 339, 6223: (1989) 360.

[77] Liu, B., T. R. Powers, and K. S. Breuer. "Force-free swimming of a model helical flagellum in viscoelastic fluids." *Proceedings of the National Academy of Sciences* 108, 49: (2011) 19,516–19,520.

[78] Lohse, D. J., and N. Hadjichristidis. "Microphase separation in block copolymers." *Current opinion in colloid & interface science* 2, 2: (1997) 171–176.

[79] Martinez, V. A., R. Besseling, O. A. Croze, J. Tailleur, M. Reufer, J. Schwarz-Linek, L. G. Wilson, M. A. Bees, and W. C. Poon. "Differential Dynamic Microscopy: A High-Throughput Method for Characterizing the Motility of Microorganisms." *Biophysical Journal* 103, 8: (2012) 1637 – 1647.

[80] Martinez, V. A., E. Clément, J. Arlt, C. Douarche, A. Dawson, J. Schwarz-Linek, A. K. Creppy, V. Škultéty, A. N. Morozov, H. Auradou, et al. "A combined rheometry and imaging study of viscosity reduction in bacterial suspensions." *Proceedings of the National Academy of Sciences* 117, 5: (2020) 2326–2331.

[81] Martinez, V. A., J. Schwarz-Linek, M. Reufer, L. G. Wilson, A. N. Morozov, and W. C. K. Poon. "Flagellated bacterial motility in polymer solutions." *Proceedings of the National Academy of Sciences* 111, 50: (2014) 17,771–17,776.

[82] Mathijssen, A. J., R. Jeanneret, and M. Polin. "Universal entrainment mechanism controls contact times with motile cells." *Physical Review Fluids* 3, 3: (2018) 033,103.

[83] Meakin, P., T. Vicsek, and F. Family. "Dynamic cluster-size distribution in cluster-cluster aggregation: Effects of cluster diffusivity." *Physical Review B* 31, 1: (1985) 564.

[84] van der Meer, B., L. Filion, and M. Dijkstra. "Fabricating large two-dimensional single colloidal crystals by doping with active particles." *Soft Matter* 12, 14: (2016) 3406–3411.

[85] van der Meer, B., M. Dijkstra, and L. Filion. "Removing grain boundaries from three-dimensional colloidal crystals using active dopants." *Soft matter* 12, 25: (2016) 5630–5635.

[86] Menzel, A. M., and H. Löwen. "Traveling and resting crystals in active systems." *Physical review letters* 110, 5: (2013) 055,702.

[87] Mino, G., T. E. Mallouk, T. Darnige, M. Hoyos, J. Dauchet, J. Dunstan, R. Soto, Y. Wang, A. Rousselet, and E. Clement. "Enhanced diffusion due to active swimmers at a solid surface." *Physical review letters* 106, 4: (2011) 048,102.

[88] Miño, G., J. Dunstan, A. Rousselet, E. Clément, and R. Soto. "Induced diffusion of tracers in a bacterial suspension: theory and experiments." *Journal of Fluid Mechanics* 729: (2013) 423–444.

[89] Mognetti, B. M., A. S˘aric, S. Angioletti-Uberti, A. Cacciuto, C. Valeriani, and D. Frenkel. "Living clusters and crystals from low density suspensions of active colloids." *Phys. Rev. Lett.* 111: (2013) 245,702.

[90] Morozov, A., and D. Marenduzzo. "Enhanced diffusion of tracer particles in dilute bacterial suspensions." *Soft Matter* 10, 16: (2014) 2748–2758.

[91] Naredi-Rainer, N., J. Prescher, A. Hartschuh, and D. Lamb. "Confocal Microscopy." In *Fluorescence Microscopy: From Principles to Biological Applications*, Wiley-VCH, 2013, 175–213.

[92] Navarro, R. M., and S. M. Fielding. "Clustering and phase behaviour of attractive active particles with hydrodynamics." *Soft Matter* 11, 38: (2015) 7525–7546.

[93] Nomura, T., Y. Morimoto, M. Ishikawa, H. Tokumoto, and Y. Konishi. "Synthesis of hollow silica microparticles from bacterial templates." *Advanced Powder Technology* 21, 1: (2010) 8–12.

[94] Noro, M. G., and D. Frenkel. "Extended corresponding-states behavior for particles with variable range attractions." *J. Chem. Phys.* 113: (2000) 2941–2944.

[95] Nossal, R., S.-H. Chen, and C.-C. Lai. "Use of laser scattering for quantitative determinations of bacterial motility." *Optics communications* 4, 1: (1971) 35–39.

[96] Olivier, B., and C. Sorensen. "Variable aggregation rates in colloidal gold: kernel homogeneity dependence on aggregant concentration." *Physical Review A* 41, 4: (1990) 2093.

[97] Omar, A. K., Y. Wu, Z.-G. Wang, and J. F. Brady. "Swimming to stability: structural and dynamical control via active doping." *ACS nano* 13, 1: (2018) 560–572.

[98] Palacci, J., C. Cottin-Bizonne, C. Ybert, and L. Bocquet. "Sedimentation and effective temperature of active colloidal suspensions." *Physical Review Letters* 105, 8: (2010) 088,304.

[99] Patteson, A. E., A. Gopinath, P. K. Purohit, and P. E. Arratia. "Particle diffusion in active fluids is non-monotonic in size." *Soft matter* 12, 8: (2016) 2365–2372.

[100] Petroff, A. P., X.-L. Wu, and A. Libchaber. "Fast-moving bacteria self-organize into active two-dimensional crystals of rotating cells." *Physical review letters* 114, 15: (2015) 158,102.

[101] Pierce, F., C. Sorensen, and A. Chakrabarti. "Aggregation- Fragmentation in a Model of DNA-Mediated Colloidal Assembly." *Langmuir* 21, 20: (2005) 8992–8999.

[102] Poon, W. "From Clarkia to Escherichia and Janus: The physics of natural and synthetic active colloids." *Proc. Intl Sch. Phys. Enrico Fermi* 184: (2013) 317–386.

[103] Poon, W., and P. Warren. "Phase behaviour of hard-sphere mixtures." *EPL (Europhysics Letters)* 28, 7: (1994) 513.

[104] Poon, W. C. *Colloidal suspensions*. Oxford Handbooks, 2012.

[105] Porter, M. K., A. P. Steinberg, and R. F. Ismagilov. "Interplay of motility and polymer-driven depletion forces in the initial stages of bacterial aggregation." *Soft matter* 15, 35: (2019) 7071–7079.

[106] Pusey, P., A. Pirie, and W. Poon. "Dynamics of colloid-polymer mixtures." *Physica A: Statistical Mechanics and its Applications* 201, 1-3: (1993) 322–331.

[107] Pusey, P., and W. Van Megen. "Detection of small polydispersities by photon correlation spectroscopy." *The Journal of chemical physics* 80, 8: (1984) 3513–3520.

[108] Pushkin, D. O., and J. M. Yeomans. "Fluid mixing by curved trajectories of microswimmers." *Physical review letters* 111, 18: (2013) 188,101.

[109] Pushkin, D. O., H. Shum, and J. M. Yeomans. "Fluid transport by individual microswimmers." *Journal of Fluid Mechanics* 726: (2013) 5–25.

[110] Pushkin, D. O., and J. M. Yeomans. "Stirring by swimmers in confined microenvironments." *Journal of Statistical Mechanics: Theory and Experiment* 2014, 4: (2014) P04,030.

[111] Ramananarivo, S., E. Ducrot, and J. Palacci. "Activity-controlled annealing of colloidal monolayers." *Nature communications* 10, 1: (2019) 3380.

[112] Redner, G. S., A. Baskaran, M. F. Hagan, M. F. S. of Physics, B. University, Waltham, MA, and USA. "Reentrant Phase Behavior in Active Colloids with Attraction." *Phys. Rev. E.* 88: (2013) 012,305.

[113] Rodriguez, D. R., F. Alarcon, R. Martinez, J. Ramírez, and C. Valeriani. "Phase behaviour and dynamical features of a two-dimensional binary mixture of active/passive spherical particles." *Soft matter* 16, 5: (2020) 1162–1169.

[114] Royall, C. P., W. C. K. Poon, and E. R. Weeks. "In search of colloidal hard spheres." *Soft Matter* 9: (2013) 17–27.

[115] Royall, C. P. "Hunting mermaids in real space: Known knowns, known unknowns and unknown unknowns." *Soft Matter* 14, 20: (2018) 4020–4028.

[116] Royall, C. P., J. Eggers, A. Furukawa, and H. Tanaka. "Probing Colloidal Gels at Multiple Length Scales: The Role of Hydrodynamics." *Phys. Rev. Lett.* 114: (2015) 258,302.

[117] Royall, C. P., S. R. Williams, and H. Tanaka. "Vitrification and gelation in sticky spheres." *The Journal of chemical physics* 148, 4: (2018) 044,501.

[118] Rubinstein, M. *Polymer physics*. Oxford ; New York: Oxford University Press, 2003.

[119] Sanchez, R., and P. Bartlett. "Equilibrium cluster formation and gelation." *Journal of Physics: Condensed Matter* 17, 45: (2005) S3551.

[120] Savin, T., and P. S. Doyle. "Static and Dynamic Errors in Particle Tracking Microrheology." *Biophysical Journal* 88, 1: (2005) 623–638.

[121] Schwarz-Linek, J., G. Dorken, A. Winkler, L. G. Wilson, N. T. Pham, C. E. French, T. Schilling, and W. C. K. Poon. "Polymer-induced phase separation in suspensions of bacteria." *EPL (Europhysics Letters)* 89, 6: (2010) 68,003.

[122] Schwarz-Linek, J., C. Valeriani, A. Cacciuto, M. E. Cates, D. Marenduzzo, A. N. Morozov, and W. C. K. Poon. "Phase separation and rotor self-assembly in active particle suspensions." *Proceedings of the National Academy of Sciences* 109, 11: (2012) 4052–4057.

[123] Schwarz-Linek, J., J. Arlt, A. Jepson, A. Dawson, T. Vissers, D. Miroli, T. Pilizota, V. A. Martinez, and W. C. Poon. "Escherichia coli as a model active colloid: A practical introduction." *Colloids and Surfaces B: Biointerfaces* 137: (2016) 2 – 16. Biocolloids and Colloids in Biology.

[124] Schwarz-Linek, J., A. Winkler, L. G. Wilson, N. T. Pham, T. Schilling, and W. C. K. Poon. "Polymer-induced phase separation in Escherichia coli suspensions." *Soft Matter* 6: (2010) 4540–4549.

[125] Semeraro, E. F., J. M. Devos, and T. Narayanan. "Effective interactions and dynamics of small passive particles in an active bacterial medium." *The Journal of chemical physics* 148, 20: (2018) 204,905.

[126] Smallenburg, F., and H. Löwen. "Swim pressure on walls with curves and corners." *Physical Review E* 92, 3: (2015) 032,304.

[127] Smith, P., G. Petekidis, S. Egelhaaf, and W. Poon. "Yielding and crystallization of colloidal gels under oscillatory shear." *Physical Review E* 76, 4: (2007) 041,402.

[128] Soper, A. "Empirical potential Monte Carlo simulation of fluid structure." *Chemical Physics* 202, 2-3: (1996) 295–306.

[129] Sorensen, C., H. Zhang, and T. Taylor. "Cluster-size evolution in a coagulation-fragmentation system." *Physical review letters* 59, 3: (1987) 363.

[130] Sowa, Y., and R. M. Berry. "Bacterial flagellar motor." *Quarterly reviews of biophysics* 41, 2: (2008) 103–132.

[131] Spöring, I., V. A. Martinez, C. Hotz, J. Schwarz-Linek, K. L. Grady, J. M. Nava-Sedeño, T. Vissers, H. M. Singer, M. Rohde, C. Bourquin, H. Hatzikirou, W. C. K. Poon, Y. S. Dufour, and M. Erhardt. "Hook length of the bacterial flagellum is optimized for maximal stability of the flagellar bundle." *PLOS Biology* 16, 9: (2018) 1–19.

[132] Steinhardt, P. J., D. R. Nelson, and M. Ronchetti. "Bond-orientational order in liquids and glasses." *Physical Review B* 28, 2: (1983) 784.

[133] Stenhammar, J., D. Marenduzzo, R. J. Allen, and M. E. Cates. "Phase behaviour of active Brownian particles: the role of dimensionality." *Soft Matter* 10, 10: (2014) 1489–1499.

[134] Stenhammar, J., R. Wittkowski, D. Marenduzzo, and M. E. Cates. "Activity-induced phase separation and self-assembly in mixtures of active and passive particles." *Physical review letters* 114, 1: (2015) 018,301.

[135] Stradner, A., H. Sedgwick, F. Cardinaux, W. C. Poon, S. U. Egelhaaf, and P. Schurtenberger. "Equilibrium cluster formation in concentrated protein solutions and colloids." *Nature* 432, 7016: (2004) 492.

[136] Szakasits, M. E., W. Zhang, and M. J. Solomon. "Dynamics of fractal cluster gels with embedded active colloids." *Physical review letters* 119, 5: (2017) 058,001.

[137] Tailleur, J., and M. E. Cates. "Statistical Mechanics of Interacting Run-and-Tumble Bacteria." *Phys. Rev. Lett.* 100: (2008) 218,103.

[138] Takatori, S. C., W. Yan, and J. F. Brady. "Swim pressure: stress generation in active matter." *Physical review letters* 113, 2: (2014) 028,103.

[139] Taylor, G. I. `http://web.mit.edu/hml/ncfmf.html`, 1967. See 'low Reynolds number flow'.

[140] Theurkauff, I., C. Cottin-Bizonne, J. Palacci, C. Ybert, and L. Bocquet. "Dynamic clustering in active colloidal suspensions with chemical signaling." *Phys. Rev. Lett.* 108: (2012) 268,303.

[141] Truskett, T. M., S. Torquato, S. Sastry, P. G. Debenedetti, and F. H. Stillinger. "Structural precursor to freezing in the hard-disk and hard-sphere systems." *Physical review E* 58, 3: (1998) 3083.

[142] Tuinier, R., J. Rieger, and C. De Kruif. "Depletion-induced phase separation in colloid–polymer mixtures." *Advances in colloid and interface science* 103, 1: (2003) 1–31.

[143] Tung, C., J. Harder, C. Valeriani, and A. Cacciuto. "Micro-phase separation in two dimensional suspensions of self-propelled spheres and dumbbells." *Soft Matter* 12, 2: (2016) 555–561.

[144] Turner, L., W. S. Ryu, and H. C. Berg. "Real-time imaging of fluorescent flagellar filaments." *Journal of bacteriology* 182, 10: (2000) 2793–2801.

[145] Uhlenbeck, G. E., and L. S. Ornstein. "On the theory of the Brownian motion." *Physical review* 36, 5: (1930) 823.

[146] Valeriani, C., M. Li, J. Novosel, J. Arlt, and D. Marenduzzo. "Colloids in a bacterial bath: simulations and experiments." *Soft Matter* 7, 11: (2011) 5228–5238.

[147] Van Blaaderen, A., A. Imhof, W. Hage, and A. Vrij. "Three-dimensional imaging of submicrometer colloidal particles in concentrated suspensions using confocal scanning laser microscopy." *Langmuir* 8, 6: (1992) 1514–1517.

[148] Van Dongen, P., and M. Ernst. "Dynamic scaling in the kinetics of clustering." *Physical review letters* 54, 13: (1985) 1396.

[149] Van Megen, W., P. Pusey, and P. Bartlett. "Phase behavior of dispersions of hard spherical particles." *Phase Transitions: A Multinational Journal* 21, 2-4: (1990) 207–227.

[150] Vicsek, T., A. Czirók, E. Ben-Jacob, I. Cohen, and O. Shochet. "Novel type of phase transition in a system of self-driven particles." *Physical review letters* 75, 6: (1995) 1226.

[151] Vicsek, T., and F. Family. "Dynamic scaling for aggregation of clusters." *Physical Review Letters* 52, 19: (1984) 1669.

[152] Vicsek, T., and A. Zafeiris. "Collective motion." *Physics reports* 517, 3-4: (2012) 71–140.

[153] Vigil, R. D., and R. M. Ziff. "Comment on" Cluster-size evolution in a coagulation-fragmentation system"." *Physical review letters* 61, 12: (1988) 1431.

[154] ———. "On the stability of coagulation–fragmentation population balances." *Journal of colloid and interface science* .

[155] Visser, J. "Particle adhesion and removal: A review." *Particulate science and technology* 13, 3-4: (1995) 169–196.

[156] Vissers, T., A. T. Brown, N. Koumakis, A. Dawson, M. Hermes, J. Schwarz-Linek, A. B. Schofield, J. M. French, V. Koutsos, J. Arlt, et al. "Bacteria as living patchy colloids: Phenotypic heterogeneity in surface adhesion." *Science advances* 4, 4: (2018) eaao1170.

[157] Vladescu, I., E. Marsden, J. Schwarz-Linek, V. Martinez, J. Arlt, A. Morozov, D. Marenduzzo, M. Cates, and W. Poon. "Filling an emulsion drop with motile bacteria." *Physical review letters* 113, 26: (2014) 268,101.

[158] Vrij, A. "Polymers at interfaces and the interactions in colloidal dispersions." *Pure and Applied Chemistry* 48, 4: (1976) 471–483.

[159] Walz, J. Y. "Effect of polydispersity on the depletion interaction between colloidal particles." *Journal of colloid and interface science* 178, 2: (1996) 505–513.

[160] Wang, L., and H. Yu. "Chain conformation of linear polyelectrolyte in salt solutions: sodium poly (styrenesulfonate) in potassium chloride and sodium chloride." *Macromolecules* 21, 12: (1988) 3498–3501.

[161] Wayne, R. O. *Light and video microscopy.* Academic Press, 2019.

[162] Wilson, L. G., V. A. Martinez, J. Schwarz-Linek, J. Tailleur, G. Bryant, P. Pusey, and W. C. Poon. "Differential dynamic microscopy of bacterial motility." *Physical review letters* 106, 1: (2011) 018,101.

[163] Wittkowski, R., J. Stenhammar, and M. E. Cates. "Nonequilibrium dynamics of mixtures of active and passive colloidal particles." *New Journal of Physics* 19, 10: (2017) 105,003.

[164] Wu, X.-L., and A. Libchaber. "Particle Diffusion in a Quasi-Two-Dimensional Bacterial Bath." *Physical Review Letters* 84, 13: (2000) 3017–3020.

[165] Wysocki, A., R. G. Winkler, and G. Gompper. "Propagating interfaces in mixtures of active and passive Brownian particles." *New Journal of Physics* 18, 12: (2016) 123,030.

[166] Zhi Lin, J.-L. T., and S. Childress. "Stirring by squirmers." *Journal of Fluid Mechanics* 669: (2011) 167–177.

[167] Zhou, X. "Onset of gravitational collapse of colloidal gels : an optical microscopy study.", 2018.

[168] Zöttl, A., and H. Stark. "Hydrodynamics determines collective motion and phase behavior of active colloids in quasi-two-dimensional confinement." *Physical review letters* 112, 11: (2014) 118,101.